AN EXPERIMENTAL STUDY OF TRUE TRIAXIAL STRESS-INDUCED

DEFORMATION AND PERMEABILITY ANISOTROPY

IN SANDSTONES

by

Bekdar Baizhanov

A thesis submitted to the Faculty and the Board of Trustees of the Colorado School of Mines in partial fulfillment of the requirements for the degree of Master of Science (Petroleum Engineering).

Golden, Colorado

Date ____________________

Signed: ____________________________

Bekdar Baizhanov

Signed: ____________________________

Dr. Azra N. Tutuncu

Thesis Advisor

Golden, Colorado

Date ____________________

Signed: ____________________________

Dr. Erdal Ozkan

Professor and Department Head

Department of Petroleum Engineering

ABSTRACT

Determination of stress-induced anisotropy of reservoir mechanical properties is essential for a number of areas that can be collectively termed as drilling risk reduction and optimization of well and reservoir productivity. Borehole stability, well completions, hydraulic fracturing, and production operations require correct analysis of deformational behavior under a general stress state ($\sigma_1 \geq \sigma_2 \geq \sigma_3$). Current attempts to capture the effect of stress state on rock deformational characteristics typically consist of conventional triaxial testing of core samples. However, there still remains an absence of experimental results on stress-induced anisotropy of deformational properties performed under true triaxial stress state. Such stress conditions allow for independent manipulation of three principal stresses and consequently, studying of the stress-induced anisotropy of static deformation, acoustic wave velocities, permeability, resistivity, and other anisotropic properties under a variety of stress states and magnitudes.

A novel true triaxial testing apparatus was designed and built by Dr. Ali I Mese of Geomechanics Engineering and Research, PLLC, and has been loaned to UNGI to conduct measurements under realistic in-situ reservoir conditions using cylindrical core samples. This study was performed to capture the true triaxial stress effects on the deformational and flow behavior of reservoir rocks. The apparatus has been calibrated and used to study the influence of realistic stress anisotropy on static deformation, acoustic wave velocity, and permeability in sandstone core samples. Through shear stress cycling at various *b* parameter values and octahedral normal stresses, it was determined that stress-induced anisotropy is a function of closing and opening of microfractures oriented normally to increasing stresses. Changes in the nondimensional stress parameter *b*, signifying the relative magnitude of intermediate principal stress to maximum and minimum stresses, influence the mechanical behavior of rock in both dry and water-saturated conditions. Permeability measurements in the axial direction also display a dependence on magnitude and state of stress.

TABLE OF CONTENTS

LIST OF FIGURES

ACKNOWLEDGEMENTS

I would like to express heartfelt gratitude to my advisor, Dr. Azra N. Tutuncu, for this opportunity to perform hands-on geomechanical research and understand the principles of true triaxial testing for petroleum engineering applications. With her continuing support, professional advice, and care for this project, I was able to successfully complete this challenging endeavor within the time constraints of my Master's study. I want to express my thanks to Dr. Hazim Abass for being on my thesis committee and his continuous support during my study. My thanks go to Dr. Ali Mese for his technical ingenuity in creating the true triaxial testing apparatus and lending it to UNGI.

I am extremely grateful to Dr. Daisuke Katsuki for his guidance and complete involvement with this project. Dr. Katsuki's enthusiasm and technical insight have helped me tremendously throughout my work in the Geomechanics laboratory, and have made me a better engineer and researcher. I sincerely thank him for mentoring me and showing me the value of real experimental work.

I also thank all of my friends, fellow Master's and PhD students for the spirit of unity in a time of challenge. My thanks go to Olawale Adekunle, Dina Hegazy, and Jessica Iriarte, for sharing with me many days and nights spent working in the laboratory.

I also thank Maxat, Chingis, and Dlwar – my dear friends that accompanied me throughout my journey.

Lastly and most importantly, I would like to thank my family for their never-ending support of my interests and aspirations. I would not be the person that I am if not for my parents, my little brother, my elder brother, and his family. They are my continuous source of inspiration, a shining light during challenging times, and firm believers in my success, for which I am deeply thankful.

For my family

CHAPTER 1

INTRODUCTION

1.1 Motivation

With development of more complex oil and gas projects in the recent years, laboratory reservoir rock testing has been gaining importance in petroleum engineering research. As projects involving higher formation stresses, performed in increasingly unconventional fields, are becoming the norm, core-scale geomechanical analysis remains an important source of insight for such ventures. Drilling through highly anisotropic formation rocks and regions with overpressure or high overburden, borehole stability, and hydraulic fracture stimulation require knowledge of in-situ stress state and rock deformation characteristics. Unconventional petroleum resources are one such area in which large-scale simulation is extremely difficult, making laboratory core-scale data crucial to our understanding of fluid flow and deformation processes.

The Unconventional Natural Gas and Oil Institute at the Colorado School of Mines performs coupled geomechanics research involving core-scale experiments with uniaxial and conventional triaxial conditions. Investigatory work on permeability and deformation using ultrasonic wave propagation at elevated pore pressures has been performed. The Institute has also recently obtained a novel prototype true triaxial testing apparatus on a temporary loan. However, the potential of the true triaxial testing apparatus had not been fully explored. While the prototype is on a temporary loan to UNGI, its practical application has to be established as correlating to the theoretical capabilities included in its design. This includes the controlled generation of three independent principal stresses in a cylindrical core sample, pore pressure, and measurements of wave velocity, static deformation, permeability, and resistivity in a rock specimen.

The combination of the availability of a true triaxial apparatus and the potential for novel laboratory geomechanical research, accompanied with the accessible resources at UNGI, rendered this opportunity into a viable Master's thesis project.

1.2 Purpose of the Study

This study aims to investigate the influence of true triaxial stress anisotropy on deformation and permeability of sandstones, determine the relationship between laboratory derived static and dynamic moduli, and demonstrate the capabilities of the UNGI true triaxial apparatus as comparable to those of conventional triaxial testing devices most commonly used in petroleum engineering research.

The experimental work is concentrated on true triaxial testing of cylindrical Buff Berea sandstone samples. The reasons that caused this sedimentary rock to be selected for testing are threefold. Firstly, Buff Berea sandstone exhibits a relatively low degree of intrinsic anisotropy, being a transversely isotropic material, and is therefore a more appropriate choice to study stress-induced anisotropy without the added effects of fractures and large laminations, such as would be the case with most shales. Secondly, millidarcy-scale permeability of Berea allows for short periods of saturation and pore pressure equilibration in the sample, effectively simplifying the testing procedure and allowing time for calibration of the apparatus and associated measurements. Lastly, the lack of high clay content in the quarried sandstone samples allows for application of pore pressure effects with minimum fluid-rock interactions that could influence the deformation of rock under anisotropic stress conditions.

Most of the compressional testing of reservoir rock samples has been limited to conventional triaxial apparatuses, in which two of the principal stresses are equal ($\sigma_1 > \sigma_2 = \sigma_3$ or $\sigma_1 = \sigma_2 > \sigma_3$). Moreover, the bulk of previously published works on true triaxial testing of reservoir rocks involves failure testing with devices limited by some of the common issues, such as loading eccentricity, blank loading corners, and restrictions in sample deformation.

Owing to the novel design and laboratory calibration work, the true triaxial apparatus that serves as the basis of this study incorporates no such issues. The results of this study can improve the understanding of stress-induced anisotropy of deformation under unrestricted, general stress conditions ($\sigma_1 \geq \sigma_2 \geq \sigma_3$), and allow for comparisons to be drawn with more limited conventional triaxial testing. The effect of intermediate principal stress, σ_2, on permeability anisotropy, wave propagation, as well as static and dynamic elastic moduli, will be explored to gain insight on the importance of laboratory true triaxial testing in petroleum engineering applications.

1.3 Rock Properties of Buff Berea Sandstone

Buff Berea is a fine-to-medium grained Lower Mississippian sandstone. It should be noted for clarity that different Berea sandstones may show different properties, owing to the widespread deposition area of the Bedford-Berea sedimentary sequence that stretches from Pennsylvania to Kentucky, and the associated changes in lithology of the formation. The samples used in this study are quarried from Kipton, Lorain county, mid-north Ohio. They are well-sorted and light-brown with presence of darker-brown quartz minerals. While variations in lithology may exist for different Berea sandstones, the samples of Buff Berea exhibit a porosity of 23%, water permeability in the 80-120 mD range, which is common among other Berea sandstones. Grain density of Buff Berea samples used in this study is 2.64 g/cm^3.

According to Lo et al., the mineral composition of Berea sandstone is mainly quartz and minor amounts of feldspars, kaolinite, and carbonate materials (1986). Lene and Owen (1969) performed a quartz-grain orientation study on Berea sandstone and suggested that most quartz grains are oriented with long axes parallel to the plane of bedding. Berea sandstone is defined as a transversely isotropic material, for which the main cause of anisotropy is the weakly preferred orientation of cracks and flat pores. In many rocks, transverse isotropy and other types of elastic anisotropy are observed through acoustic velocity changes under stress (Lo et al. 1986; Takahashi and Koide 1989; Thosuwan et al. 2009).

CHAPTER 2

LITERATURE REVIEW

2.1 Rock Deformation Principles

Before investigating the effects of stress state on deformation anisotropy, it is necessary to consider a specific definition of deformation. For homogeneous and isotropic rocks, there are four types of constitutive laws governing rock deformation: elastic, poroelastic, elasto-plastic, and viscoelastic laws (Zoback 2007). For linearly elastic materials, stress and strain are proportional to one another and deformation is reversible. For elastic media, the deformation associated with loading is fully recovered during unloading (Amadei 1983). However, rocks rarely show perfect linear-elastic behavior because of complex processes of rock deformation owing to heterogeneity and anisotropy. The existence of microcracks, pore space, and irregularities in rock microfabric often causes non-linear elasticity up to a yield point, after which plastic deformation is dominant. Typically, rocks first deform non-linearly in response to applied stress, which is signified by microfracture closures. Afterwards, the behavior becomes more linear elastic until failure stress is reached. A suitable example of realistic rock deformation was illustrated by Jaeger et al. (2007) in a complete stress-strain diagram for rock under uniaxial stress (Figure 2.1). The closure of microfractures in the rock is seen in region OA with a positive curvature, followed by a nearly linear elastic deformation in region AB. The region BC is where irreversible strain occurs in the rock, leading to a gradual decrease in the slope of the curve and a final failure of the rock at point C. Upon reaching point P on the BC curve, the stress is unloaded to zero, but some strain remains in the rock, shown as ε_O. In addition, a hysteretic behavior is demonstrated when deformation during loading and unloading follows different stress-strain curves. Further loading would result in joining to the original stress-strain curve at point R, corresponding to a higher stress and strain than point P. Differences between loading and unloading stress-strain curves are associated to energy loss in the form of friction along grain boundaries and microfracture faces (Jaeger et al. 2007). While post-failure deformation in the rock is possible within a larger rock mass, it cannot be measured in core-scale laboratory testing due to loss of any cohesion in core specimens.

Another factor in deformation is poroelasticity, which takes place in the compression of pore space of rock saturated with fluid. The pore fluid pressure counteracts the stress created in a rock. Nevertheless, the poroelastic behavior is largely influenced by the rate of applied stress, and the difference of stiffness in undrained and drained rocks is an example of such behavior. If the rate of applied stress is greater than the rate of fluid being exerted out of pore space, the fluid tends to stiffen the rock by carrying part of the total stress. Similar to poroelasticity, viscoelasticity of a rock describes the deformation with respect to stress as rate-dependent. Overall, the coupled physics of such relationships between stress, strain, fluid flow, and viscosity, are used to describe the deformational behavior of rocks.

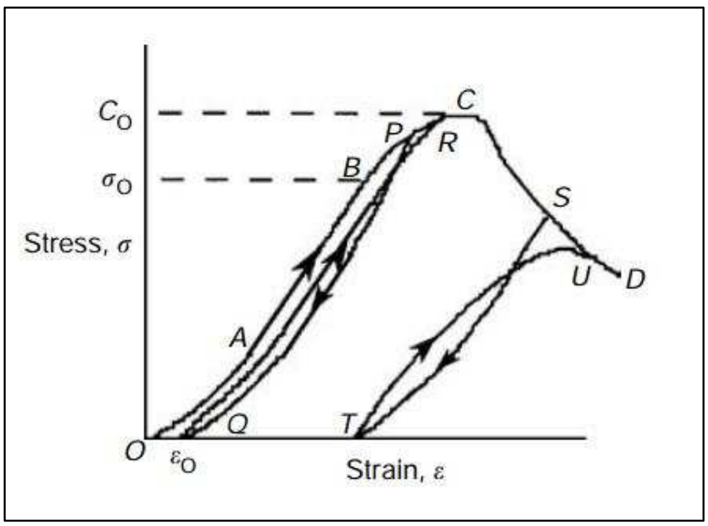

Figure 2.1: Stress-strain diagram of a rock under uniaxial stress (Jaeger et al. 2007).

In studying deformation, elastic moduli are used to describe the deformation caused by applied stress. An overview of the three types of strain and their relation to elastic moduli is shown in Figure 2.2. These elastic moduli describe the deformation of rock when subjected to three types of stress: uniaxial stress, shear stress, and hydrostatic stress. However, they are commonly used in describing deformation under conventional triaxial stress state.

An important characteristic of the linear-elasticity model for homogeneous and isotropic rock is that it requires only two elastic moduli to describe its deformational behavior. However, for most rocks, there exists a degree of elasticity anisotropy, meaning that rock stiffness depends on the direction in which the stress is applied.

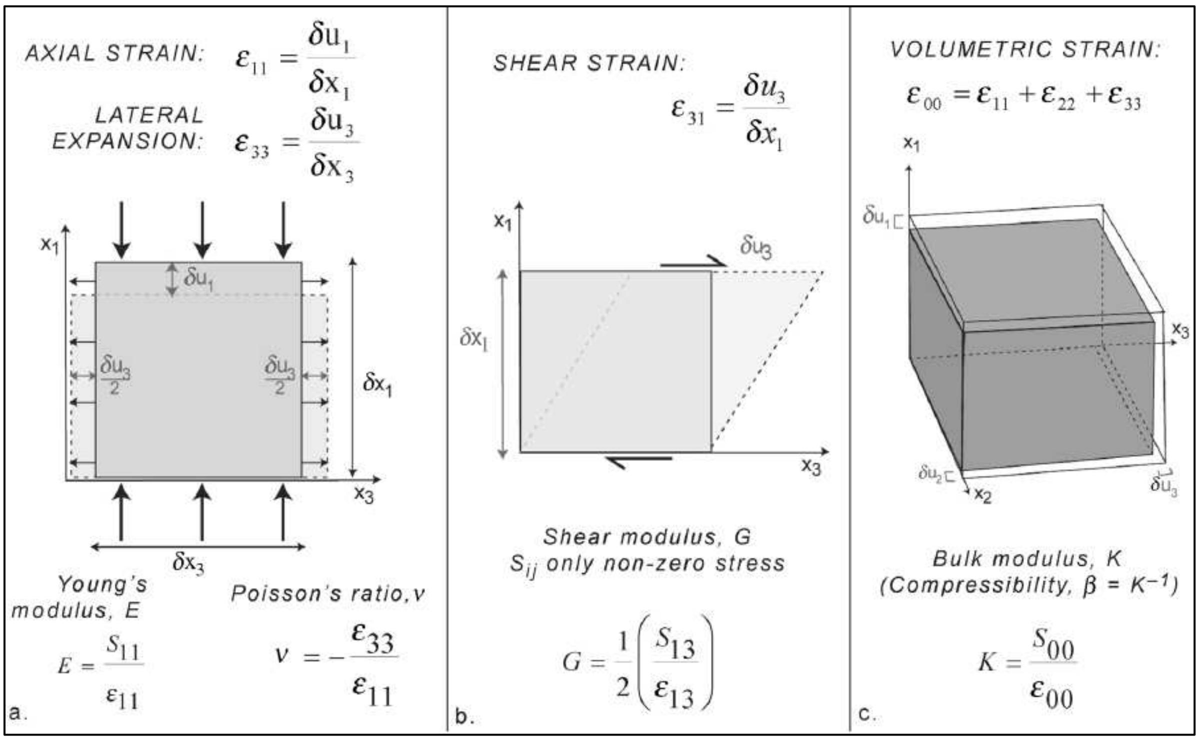

Figure 2.2: Illustration of Strain, Stress, and Elastic Moduli in Idealized Deformation Measurements (Zoback 2007).

Elasticity anisotropy can be described with the stress-strain formulation known as the generalized Hooke's law in Equation 2.1.,

$$S_{ij} = c_{ijkl} * \varepsilon_{kl} \tag{2.1}$$

where c_{ijkl} is a fourth-rank tensor with 81 constants, which can be reduced to 21 constants based on symmetry and other assumptions.

For most rocks, the characterization of anisotropy only requires five constants due to a higher degree of symmetry. Such rocks are known as transversely isotropic, meaning that vector measurements in one direction, usually vertical, in these rocks are different from measurements obtained in any other direction (Anderson et al. 1994). Calculations involving this concept are usually performed using directional wave velocities measured to investigate wave propagation anisotropy.

2.2 Stress-Induced Anisotropy

Anisotropy in rock properties is known to be a result of depositional environment, mineral microstructure, fracture alignment, and other complex physical and chemical processes of transportation, compaction, and cementation (Al-Tahini and Abousleiman 2010). However, anisotropy can also occur under large stress variations in different periods of reservoir exploitation, such as after drilling, hydraulic fracturing, production related formation subsidence, and pore-pressure depletion. It is usually known as stress-induced anisotropy.

In this section, the relationship between a stress environment in a rock and its anisotropic properties is discussed, with an emphasis on anisotropy of rock deformation, permeability, and elasticity.

2.2.1 Wave Propagation in Anisotropic Rocks

Elastic wave propagation has long been viewed as a significant source of information to determine properties of petroleum reservoirs in the form of borehole acoustic measurements and laboratory measurements of core plugs. Elastic waves are known as mechanical disturbances generated by particle movement that causes energy to propagate through a material without displacement of the material itself (Eitzenberger 2012). They take the form of compressional (longitudinal, or P-) and shear (transverse, or S-) waves. The direction of particle movement is parallel to the direction of wave propagation in P-waves and perpendicular in S-waves, respectively. Since particle vibration in S-waves takes place on a plane normal to the propagation direction, the direction of vibration on that plane can vary and is known as polarization. S-waves are usually divided into vertically (SV) and horizontally (SH) polarized components.

Wave propagation through intact rock depends on both the intrinsic properties of the rock and the external factors, such as stress state and magnitude, as well as fluid type and saturation. However, due to a differing nature of propagation, P- and S- waves react differently to these factors. Wave velocity is influenced by factors like rock texture, density, porosity, and intrinsic anisotropy. Consolidated rocks with densely packed grains generally result in higher P- and S- wave velocities than unconsolidated soils. Similarly, rocks with lower porosity lead to higher wave velocity due to an increase in grain density. The effects of mineral composition had also been previously explored (Ramana and Venkatanarayana 1972), where wave velocity trends had been noted with increasing content of certain minerals, but no conclusive statements were made.

Anisotropic properties of rocks, such as bedding, presence of microfractures, or preferential grain orientation, influence wave propagation. Since most rocks are anisotropic in nature due to aligned microfractures, minerals, large-scale fractures and faults, as well as an anisotropic stress field, wave propagation is often used to study elasticity anisotropy and progressive damage of the rock. For instance, it was previously established that elastic wave velocities decrease with formation and evolution of microfractures (Sayers and Kachanov 1995).

2.2.2 Elasticity Anisotropy

The most general definition of anisotropy of a property is “the directional variation in the value of vector measurement of a property” (Anderson et al. 1994). It is important to note that this definition is scale dependent. It depends upon the relative size of the smallest structural feature of the problem of interest with respect to the largest feature of the medium (Amadei 1983). Additionally, an exception in the use of the term exists where anisotropy is used to describe a state of stress, which results in anisotropy of intrinsic physical properties.

It was observed that such anisotropy in rock can be induced under non-hydrostatic stress state, even if the rock exhibited no anisotropy originally (Wu and Hudson 1991; Rudnicki 1977). Generally, changes in the anisotropic behavior due to stress are attributed to closure and/or opening of microfractures (Ita et al. 1993). Yin and Nur (1992) performed measurements of wave velocities under polyaxial stress and concluded that induced velocity anisotropy is a result of cracks closed in the direction of applied stress. In a study involving six different rock types, including Berea sandstone, they observed that stress affected intrinsic anisotropy, which was predominantly due to preferential grain orientation, direction of microcracks, and interbedded fine clay layers. In another study of anisotropic poroelastic response in sandstones by Lockner and Beeler (2003), it was also stated that bedding, alignment of microfractures, and mineral fabric are common causes of intrinsic anisotropy. However, they reasoned that deviatoric stress effects, even small ones, also create substantial anisotropy. In conventional triaxial compression of brine-saturated shales, both velocities and peak strength are affected by different maximum principal stress orientations with respect to bedding (Piane et al. 2010). It was determined that dilatancy of microfractures and ensuing anisotropy are increased under bedding parallel loading, whereas bedding normal loading reduces anisotropy. This particular behavior is dependent on pre-existing anisotropy as well as the stress effects. As an example, a study of faulting in an anisotropic, schistose rock under general triaxial conditions determined that weak bedding planes may control the geometry of rock deformation and faulting under stress (Kwasniewski and Mogi 2000). A similar conclusion is achieved by Piane et al., who describe the generation of microfractures as influenced by both lamination within rock, as well as magnitude and orientation of stresses (2010). As discussed by Dewhurst and Siggins (2006) and Popp and Salzer (2006), deviatoric stress causes changes in the physical properties of shale, increasing or decreasing elastic anisotropy. Particularly, these changes occur due to alterations in magnitude of mean effective stress, orientation and degree of anisotropy of the stress field. It can be generalized that, while intrinsic anisotropy plays an important role in the sensitivity of rock mechanical properties to applied stress, magnitude and orientation of mean and deviatoric stresses can also induce anisotropy in deformation and rock strength.

Measurements of different kinds were done under various stress conditions on Berea sandstone. Ita et al. (1993) investigated the effects of stress-induced anisotropy on its static and dynamic properties by performing uniaxial, biaxial, and hydrostatic loading on both saturated and unsaturated samples. Among their findings was the understanding that compressibility exhibits stress-induced anisotropy and is not only a function of mean stress. The explanation provided for such behavior was that pore compressibility and effective elastic moduli depend on stress state due to non-linear grain contact stiffness in Berea sandstone. The influence of fluid saturation is shown as viscous stiffening in addition to elastic stiffening of grain contacts. Dependence of drained pore compressibility on the states of stress applied to the samples is shown in Figure 2.3. Dynamic compressibility is maximized under biaxial state, while the static one is largest under hydrostatic conditions. This behavior is attributed to dilation of grain contacts in the direction of minimum stress, which offsets compressibility in maximum stress direction.

In measurements of elastic and poroelastic properties of Berea under axisymmetric loading, Lockner and Beeler (2003) reported that, while Berea contains intrinsic anisotropy, it only plays a role at low confining pressure, whereas the stress-induced anisotropy is seen to grow concurrently with applied differential stress. It should be noted that the experimental differential stress was constrained to about 50% of failure stress to minimize introducing any permanent microcracks to the sample.

As mentioned previously, stress-induced anisotropy was observed when applied stresses were within the elastic limit of the rock. This allowed stress-induced anisotropy to be reversible and the sample was returned to almost its original state after unloading. Another finding made in Lockner and Beeler (2003) was the determination of anisotropic poroelastic coefficients for the simplest level of anisotropy (transverse isotropy). It was determined that eight independent constants are needed to describe a poroelastic transverse isotropic system.

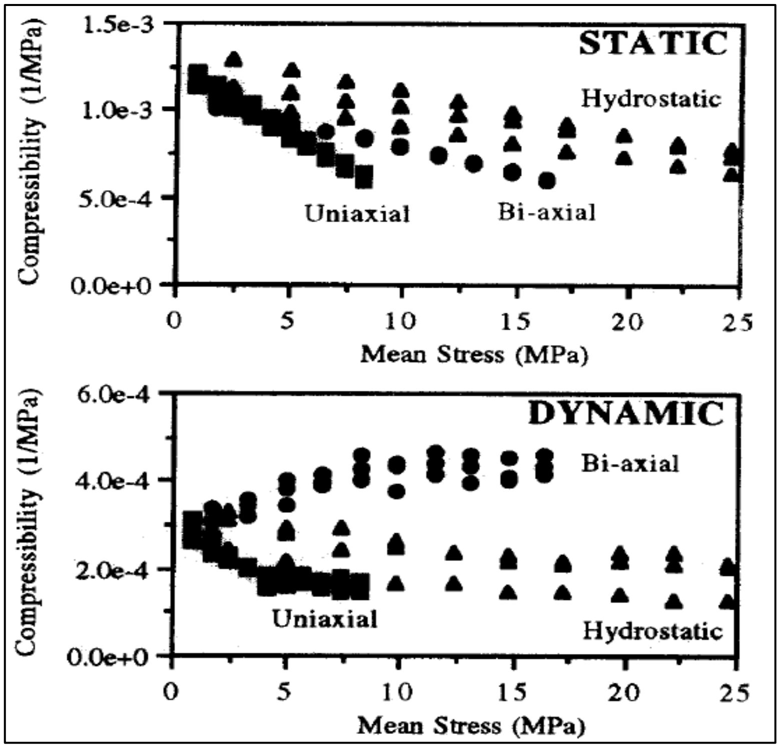

Figure 2.3: Static and dynamic drained pore compressibility for Berea sandstone under three states of stress (Ita et al. 1993).

Much of the experimental work included considerations of pore pressure and effective stress in “drained” and “undrained” tests, as well as the effect of deviatoric and differential stresses on intrinsic anisotropy. Both the intrinsic properties of rock, such as microfractures, alignment of mineral grains, and stress state were found to play an important role in creating anisotropy of static and dynamic elastic moduli.

It was determined that even homogeneous, isotropic rocks are subject to stress-induced anisotropy at both high and low levels of deviatoric or anisotropic stress, and that weak intrinsic anisotropy can be minimized under increasing stress conditions.

2.2.3 Permeability Anisotropy

Permeability anisotropy is known as the directional variability of permeability in a formation, commonly associated with intrinsic formation anisotropy, such as bedding and laminations. It is usually expressed as the ratio of horizontal to vertical permeability; k_h/k_v, or vice versa. Moreover, permeability is also stress-dependent and can be influenced by both the magnitude and state of stress in a formation.

Bruno (1993) studied experimental stress-induced permeability alteration in sandstones combined with a discreet element model that incorporates grain-boundary and intragranular microcracking, intergranular deformation, and pore network fluid flow.

During development of theoretical background for the model, Bruno defined intergranular bonds as the cementation connections bridging any two individual grains, which are subject to deformation and fracture (Figure 2.4). Pore space conduits can be seen as crossing over some of the intergranular bonds in this 2D representation of the simulation microstructure model. However, based on a simplifying assumption about flow tortuosity, pore space flow is localized at the centroids of intergranular bonds, and in 3D space the channels wrap around individual bonds. Bond deformation under stress is assumed to control the flow through pore space conduits.

Simulation of both such deformation and the formation of intragranular microfractures was performed in models such as one shown in Figure 2.5. For this particular model, the grain size range was 0.4-0.6 mm with cementation of 0.10-0.15 mm surrounding the grains, resulting in area grain density of 64%. Simulation was performed in biaxial compression with axial to lateral load ratio of 4:1 and flow direction occurring parallel to the axial loading direction. Figure 2.6 shows the resulting axial strain, microfracture formation frequency, and permeability response during loading and unloading.

Permeability decreases steadily until the onset of microfracture formation, which also corresponds to the beginning of non-linear strain behavior. As microfracture frequency rises, permeability reduction rate is decreased. This response suggests there exists a preferential orientation in microfracture formation, which is parallel to the maximum stress direction. Right before peak load is achieved and directly afterwards, permeability increases in an abrupt fashion.

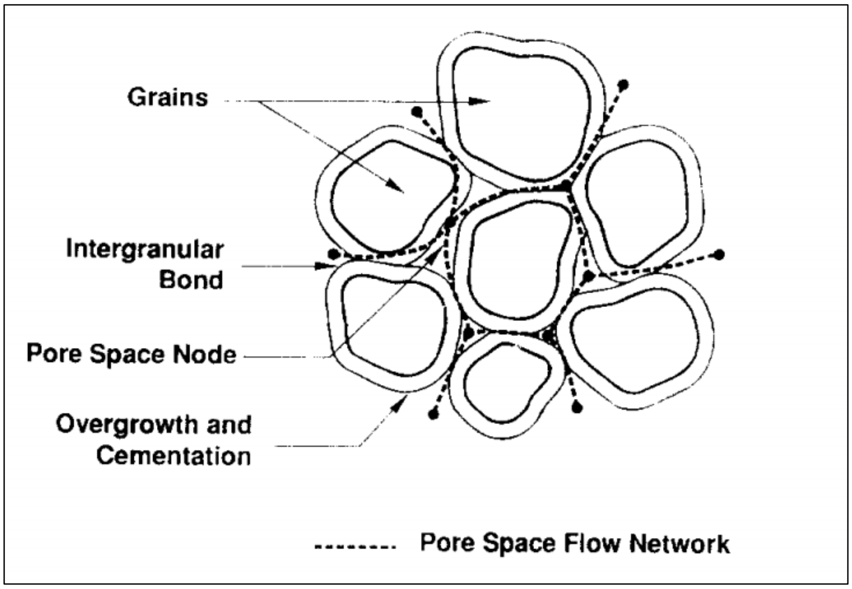

Figure 2.4: Simulation discreet element microstructure (Bruno 1993).

This behavior is attributed to the coalescence of microfractures oriented parallel to maximum stress direction into a shear band. The model was also used in simulations of uniaxial loading parallel and perpendicular to flow direction, which illustrated that permeability reduction is markedly higher when high stress is applied in direction perpendicular to flow than when it is in direction parallel to flow. This result is correlated with experimental testing performed on specimens of three different lithologies: Salt Wash sandstone, Castlegate sandstone, and Kern River sand. Each specimen was tested in conventional triaxial compression with stress magnitudes reaching 15 MPa. Figure 2.7 demonstrates the difference in permeability alteration in the two directions during loading and unloading for the Castlegate sandstone specimen. Flow-perpendicular loading clearly shows permanent permeability reduction, which can be associated with irreversible deformation and compaction.

The results of the study demonstrated a clear stress-dependency of permeability values – both the conventional triaxial testing experiments and the simulation exhibiting comparable outcomes. It was observed that under an increasing hydrostatic stress states permeability is reduced due to compaction of pore throats and channels.

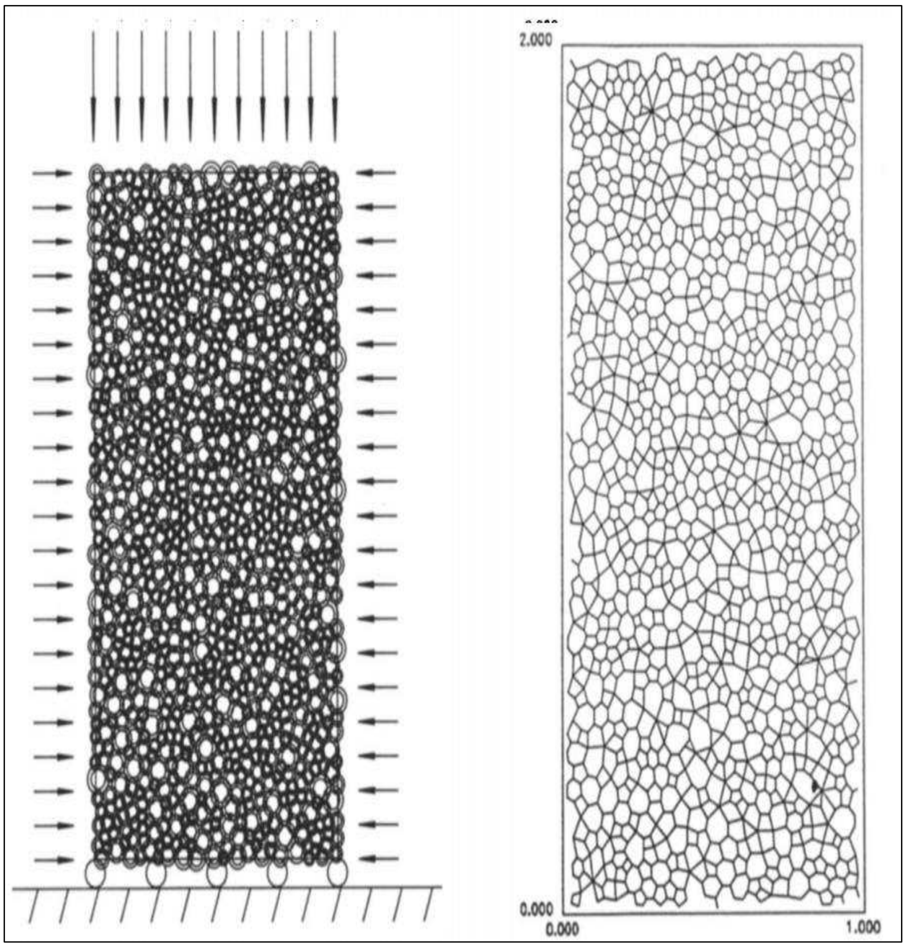

Figure 2.5: Grain model and associated pore network (Bruno 1993).

It was noted that deviatoric stress effects counteracted this reduction in permeability by enlarging of additional flow channels during tensile and shear damage to intergranular cementation, and microfracture formation within grains. Another observation was made in terms of microfracture alignment – it was preferentially oriented parallel to the maximum principal stress direction. Lastly, different stress sensitivity of permeability was attributed to the differing amount of cementation in the samples tested.

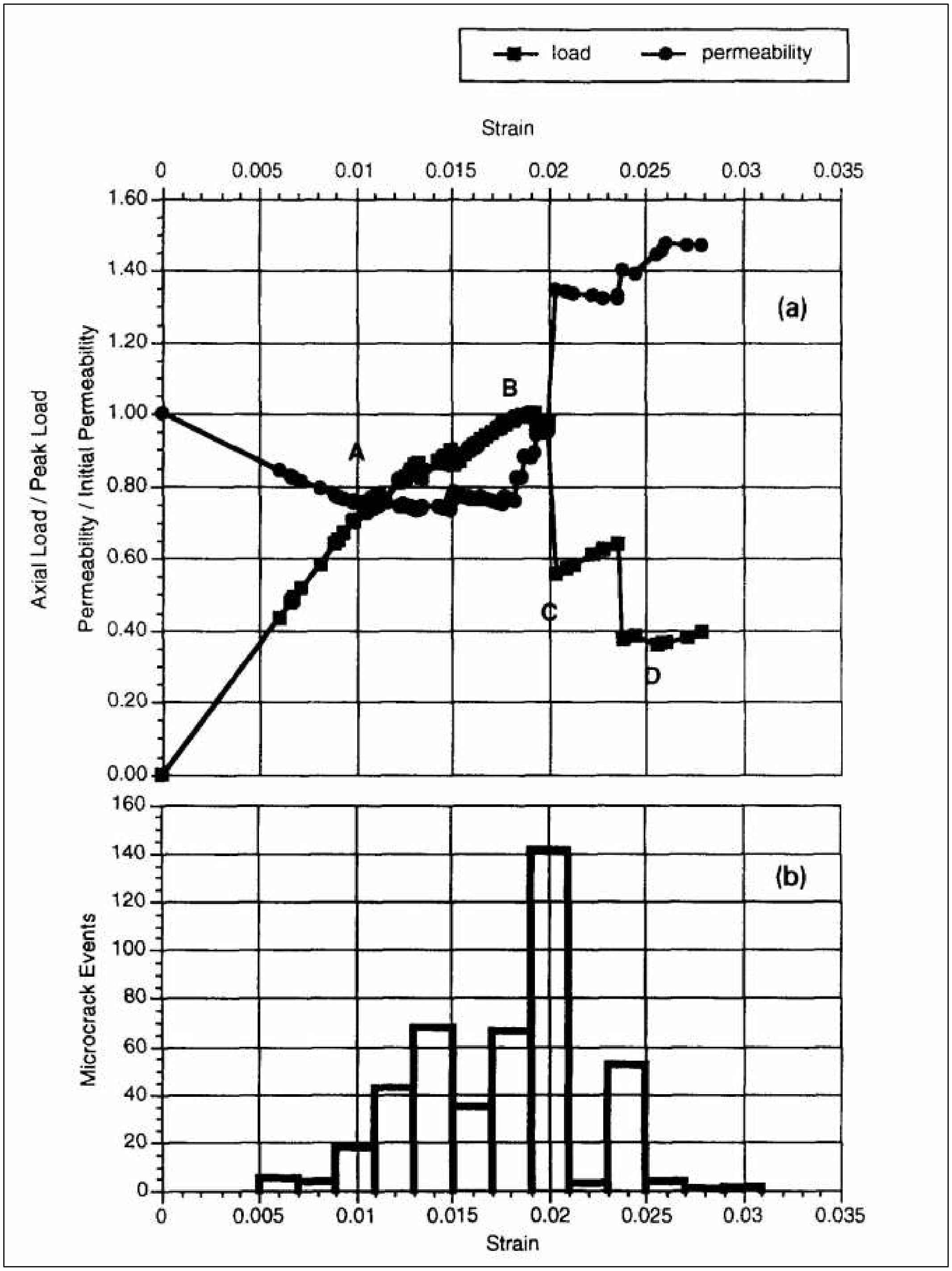

Figure 2.6: Simulation results: axial strain, permeability, and microfracture frequency with axial loading (Bruno 1993).

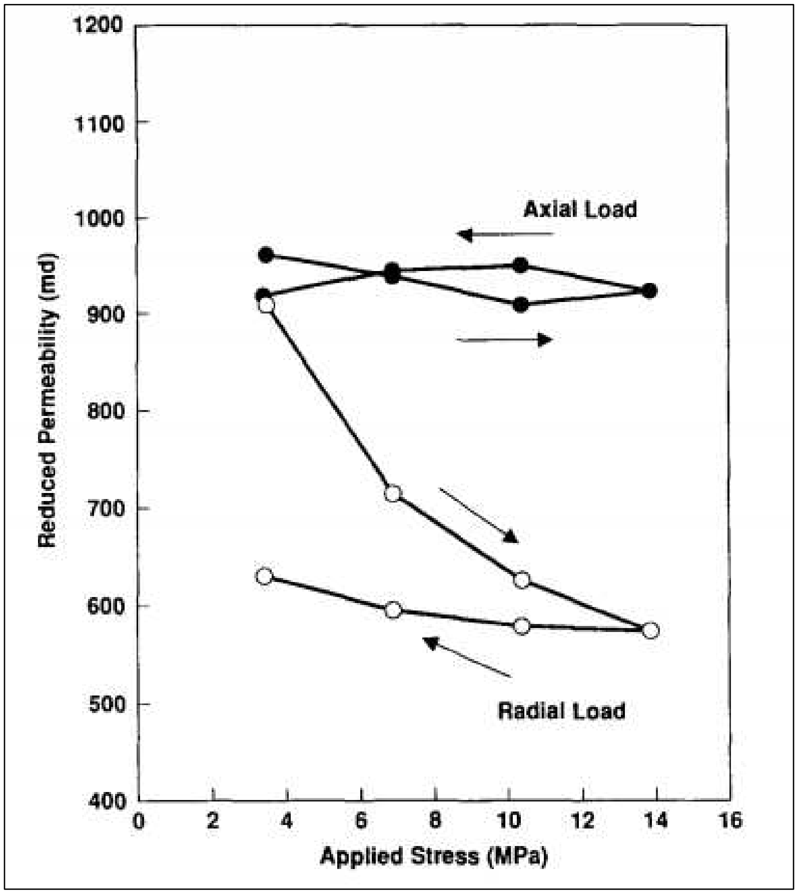

Figure 2.7: Permeability alteration for loading and unloading in axial and radial direction for Castlegate sandstone (Bruno 1993).

2.3 Common True Triaxial Cell Designs

True triaxial testing of rocks in the laboratory allows for generation of an anisotropic stress environment existing in petroleum reservoirs, and can be used to improve the understanding of their geomechanical properties. Most commonly used rock mechanical and geomechanical testing of core samples in the petroleum industry has been limited to conventional triaxial testing due its simplicity. In a conventional triaxial test, where a cylindrical core plug is loaded axially while under radial fluid confinement, the intermediate principal stress effect is not incorporated in rock deformational behavior since loading is limited to two of the three principal stresses being equal in magnitude, rendering σ_2 equal to either σ_3 or σ_1. Such behavior is well-illustrated in the Mohr-type failure criteria. In order to capture the full extent and accuracy of rock deformation under anisotropic in-situ stress conditions, one would require a true triaxial testing apparatus to create three independent orthogonal principal stresses in a rock specimen.

In this section, true triaxial testing devices are reviewed in terms of loading patterns, design advantages and limitations, and overall applicability to petroleum engineering research.

2.3.1 Historical True Triaxial Testing of Rocks

Li et al. (2011) have performed a study of historical development of true triaxial testing, listing all major true triaxial apparatus designs and their characteristics. The history of true triaxial testing of rocks begins with the discovery that rock strength is a function of intermediate principal stress, σ_2, under constant minimum principal stress, σ_3. While conventional triaxial testing had been the norm in the field of rock mechanics before true triaxial testing, it was first observed by Karman in 1911 that compressive strengths of a rock specimen measured under triaxial compression $(\sigma_1 > \sigma_2 = \sigma_3)$ and extension $(\sigma_1 = \sigma_2 > \sigma_3)$ yielded different results. This rock failure behavior was later confirmed by further testing with different rock types (Li et al. 2011, and Handin et al. 1967), and in consequence, the intermediate principal stress was found to have influence over rock strength, which led to attempts in creating a true triaxial apparatus enabling control of all three principal stress magnitudes independently. Initial approaches involved compressional and torsional testing of thin hollow cylindrical cores, whereby a true triaxial stress state was created and the ensuing test results were used to improve understanding of shear strength, fracture angle, and brittle-ductile transition (Li et al. 2011, Handin et al. 1967). However, scattering of results and inability to test brittle rocks limited the applicability of such testing.

Over time, numerous other testing devices were made that generated direct true triaxial stress within rock specimens, unlike the indirect stress created during torsional testing. Tests involved cubic, prismatic, and cylindrical rock samples, with loading actuated by rigid plates or fluid pressure through a flexible medium.

2.3.2 Classification of True Triaxial Apparatuses

A classification was created by Li et al. (2011) that categorizes existing true triaxial testing apparatuses into three types based on loading pattern. They are known as Type I: the rigid platen type, Type II: the flexible medium type, and Type III: the mixed type.

Type I apparatuses incorporate three pairs of pistons loading cubic or prismatic samples through rigid platens. While such machines are characterized by a high loading capacity and an ability to test larger specimens, a number of disadvantages have limited their applicability for rock mechanical testing, especially in petroleum engineering research. Figure 2.8 is a schematic of an apparatus by King et al. (1995), wherein three pairs of hydraulic rams are used to apply loading onto a cubic rock sample in three orthogonal directions, with pressure in any set of opposing rams being equal on opposite sides. While in this particular example loading eccentricity is minimized, other devices with fixed supports on opposite sides of hydraulic pistons cause deviation between the center of the sample and the center of loading. In order to prevent any contact between moving platens, the sample size is usually made larger than the size of individual platens, which leads to partial loading of the sample. Such blank loading corners create non-uniform stress distribution, which is detrimental to proper stress generation and affects rock deformation. Another disadvantage with Type I apparatuses is the existence of a rigid loading boundary between a specimen and the apparatus, which restricts specimen deformation and fracture surface formation. Additionally, the use of rigid platens on all faces of a sample renders permeability and acoustic testing very difficult to perform. Finally, the limitation of specimen shape to prisms and cubes creates further complexities in sample preparation.

Type II apparatuses are those in which at least two orthogonal directions of loading are equipped with fluid pressure, with the remaining direction loaded by a rigid platen, or a piston. Fluid pressure is transmitted by a flexible material that does not restrict sample deformation and eliminates blank corner loading.

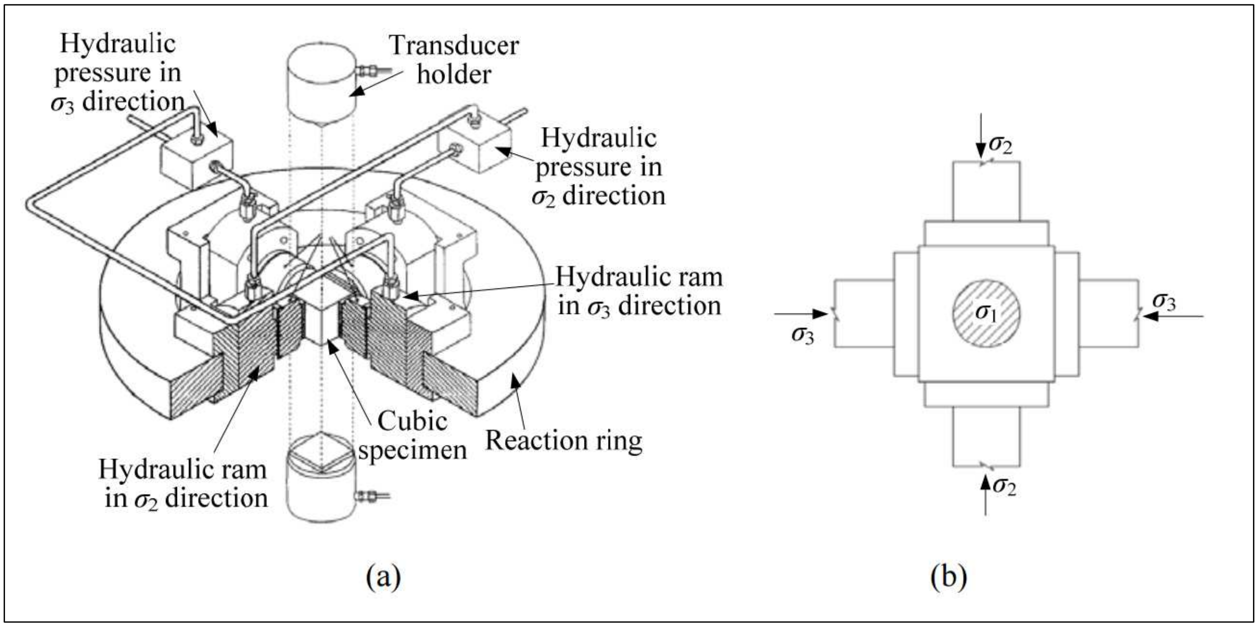

Figure 2.8: Schematic of Type I true triaxial apparatus (King et al. 1995). (a) Diagram of the machine; (b) Stress diagram of the rock sample.

A notable example of a Type II apparatus is one constructed by Smart (1995). Its design was made to minimize limitations of Type I apparatuses. Smart et al. described one of those limitations being the complex geometry of cubic specimens as problematic for weak sandstones and shales. The loading consists of rigid axial platens used to apply maximum principal stress, and radial confinement by 24 tubes surrounding the rubber jacket in a way similar to a conventional triaxial testing approach, as can be seen in Figure 2.9. The trapped tubes are held within recesses milled into the cell in order to contact the flat side of the tube with the rubber jacket surrounding the sample. Constructed from PVC, the shape of the tubes is changed to have a flat face so that the sum of all tubes develops radial stresses on the core sample when subject to independent servo-controlled fluid pressures. The 24 trapped tubes are divided into three banks of tubes (numbers 1, 2, and 3 in Figure 2.10), selective pressurization of which allows for differential radial stresses to be generated. Use of such design allowed successful testing of cylindrical specimens under true triaxial stress state and measurements of permeability in a fluid saturated rock specimen. A clear advantage of this type is the ability to compare test results to those performed in conventional triaxial testing. A limitation of this particular apparatus is its relatively low loading capacity, limiting its use in hard rocks.

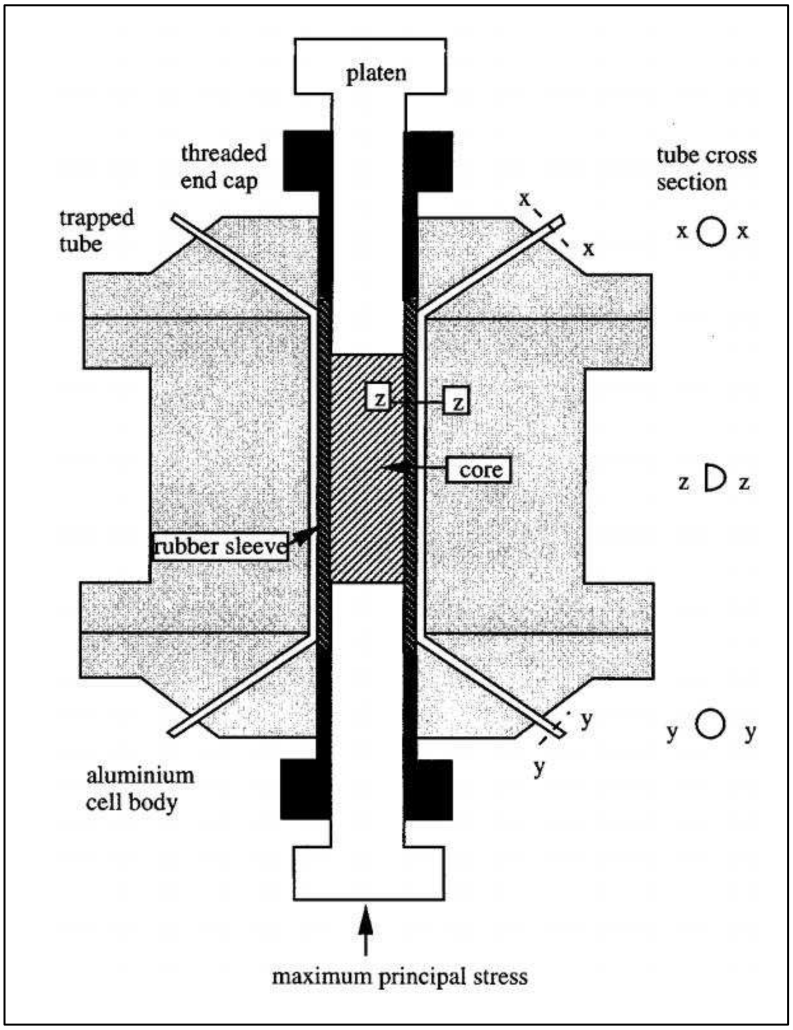

Figure 2.9: Schematic of Type II true triaxial apparatus by Smart et al. (1999).

A Type III true triaxial apparatus is one where two principal stress directions are loaded with rigid platens and the remaining one is loaded with a flexible medium. This type is also known as the Mogi-type apparatus, based on the very first design created by Mogi (1970). A schematic of a Type III apparatus is shown in Figure 2.11 - maximum and intermediate principal stresses are applied using rigid platens in a way that minimizes loading eccentricity, while minimum principal stress is created by fluid pressure applied to the remaining faces of the specimen not in contact with the platens.

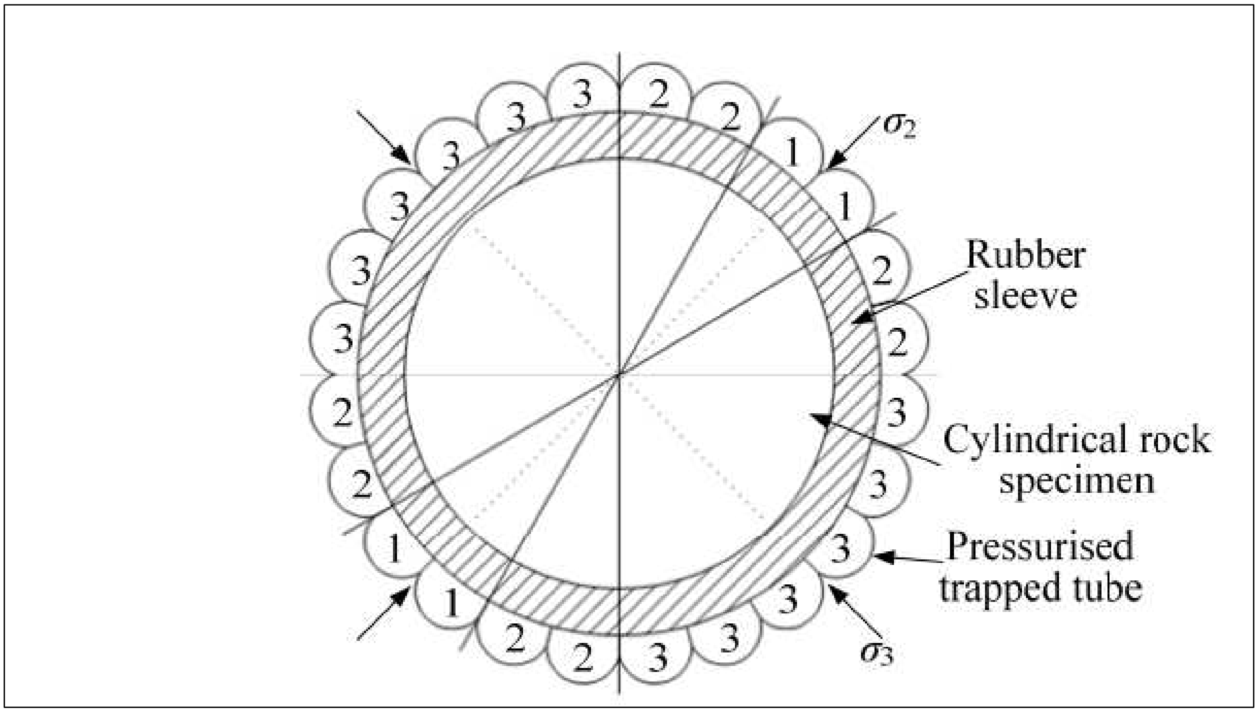

Figure 2.10: Schematic of Radial Loading. Numbers 1, 2, and 3 represent independent servo-controlled hydraulic circuits (Smart 1995).

Nevertheless, end friction and blank corner effects, however reduced, are still present. Type III device advantages over Type II apparatuses are the ability to directly measure strains along two faces of a specimen and a higher loading capacity. However, the Type III apparatus is built around rectangular shaped rock samples, which remains a disadvantage for testing of cylindrical samples and comparative analysis with conventional triaxial tests.

2.3.3 Characteristics of UNGI True Triaxial Testing Assembly

The true triaxial testing assembly used in this research study has been designed and built by Dr. Mese and loaned to UNGI by Geomechanics Engineering and Research, PLLC in 2014. A patent is pending on the apparatus at the time of writing. The true triaxial cell, which will be referred to as UNGI True Triaxial cell in this thesis study can be categorized as a Type II, or flexible medium type, apparatus capable of testing cylindrical rock specimens.

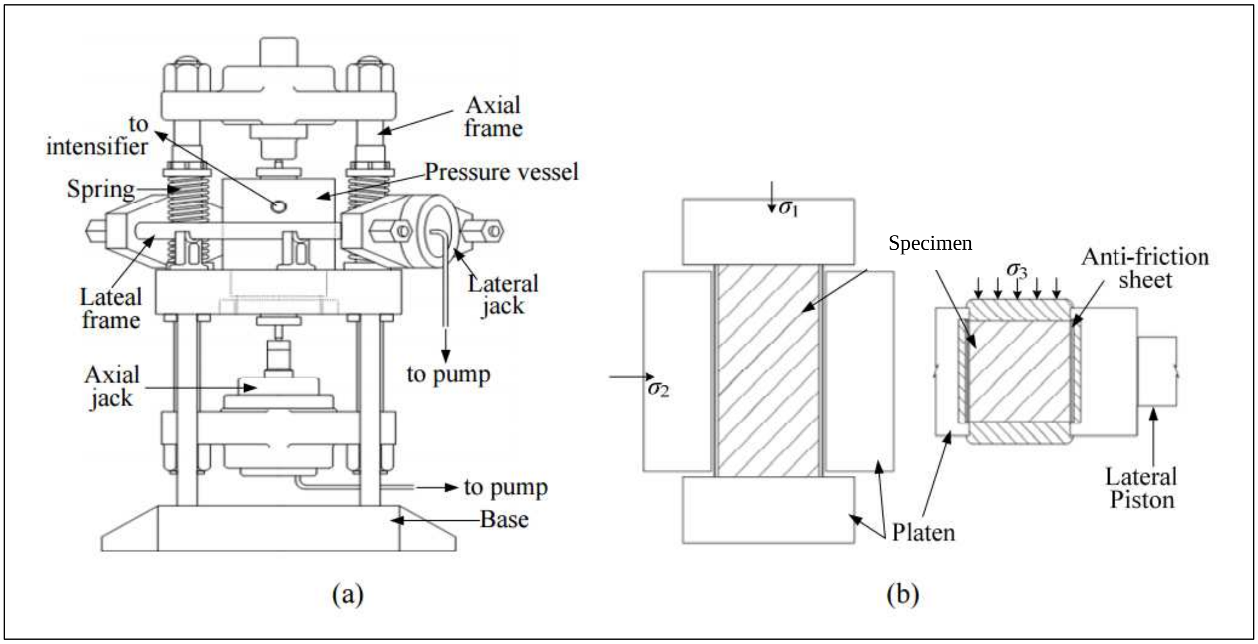

Figure 2.11: Schematic of Type III true triaxial apparatus (Mogi 1970). (a) Front view; (b) Diagram of platens and rock sample.

The assembly consists of a true triaxial cell resembling a conventional triaxial apparatus, as shown in Figure 2.12. The schematic of the apparatus is illustrated in Figure 2.13. A cylindrical sample is loaded axially by a rigid piston on one side, while placed against a fixed support on the opposite side. The axial loading creates maximum principal stress, or σ_1. On the radial plane, the specimen is loaded in σ_3 direction with confining fluid pressure applied directly to a rubber jacket. Intermediate principal stress is created with a set of two flexible rubber membranes transmitting fluid pressure on the remaining opposite sides of the specimen. The confining fluid generating σ_3 is separated from the fluid inside the membranes, which is confined within two rigid radial pistons. The radial pistons are clamped against both the axial rigid piston and the axial fixed support in order to limit generation of intermediate principal stress to the fluid inside the flexible membranes. The apparatus creates no blank loading corners, provides unrestricted rock deformation due to uniform boundary loading through flexible membranes and no end friction, and eliminates loading eccentricity. The design of the apparatus allows for relatively high loading capacity that is controlled by the pressure capacity of utilized hydraulic pumps.

The capabilities of the assembly consist of strain and wave propagation measurements in all three orthogonal directions, as well as permeability and resistivity measurements under drained and undrained conditions. However, the laboratory work performed within the time constraints of this project limited comprehensive calibration to only axial strain and wave propagation measurements, as well as permeability testing. Future studies would include full coupling of geomechanical and wave velocity anisotropy under true triaxial stress state.

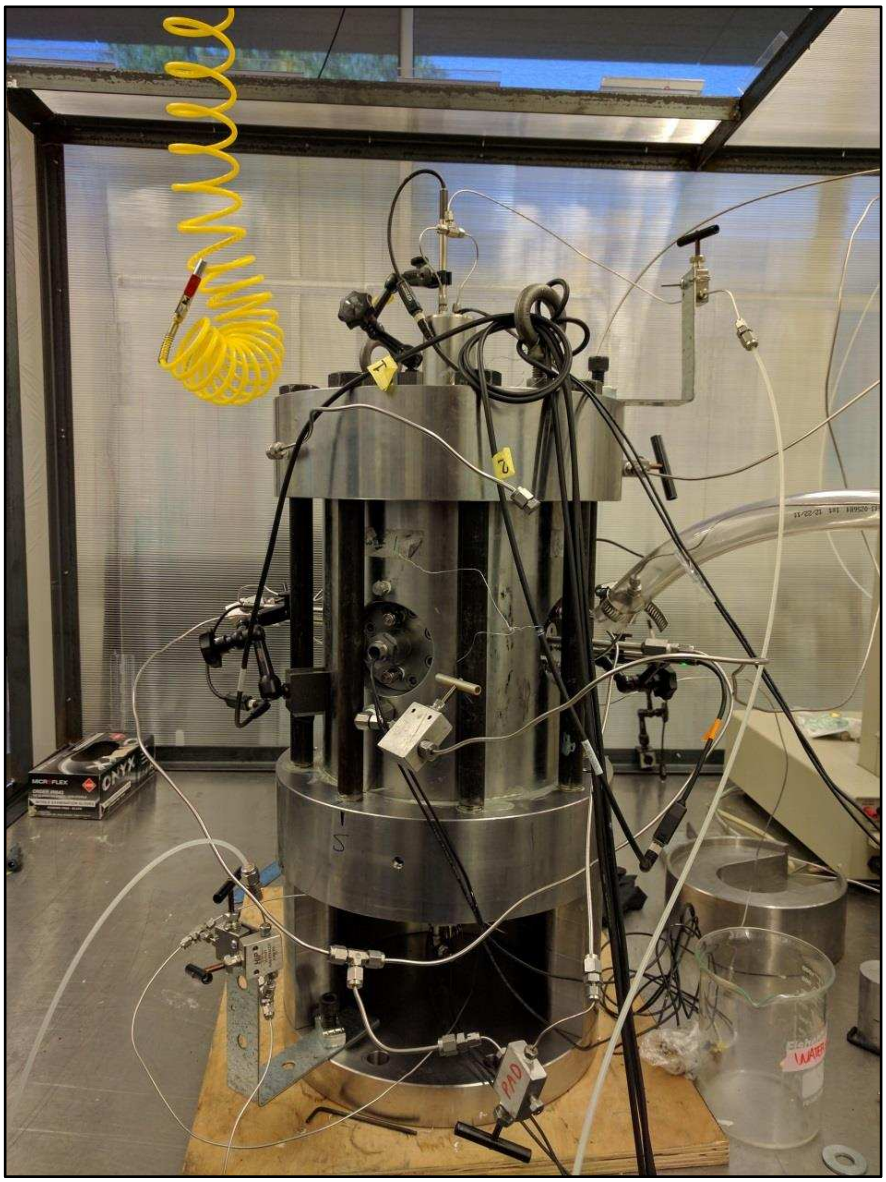

Figure 2.12: Complete assembly of the UNGI true triaxial testing apparatus.

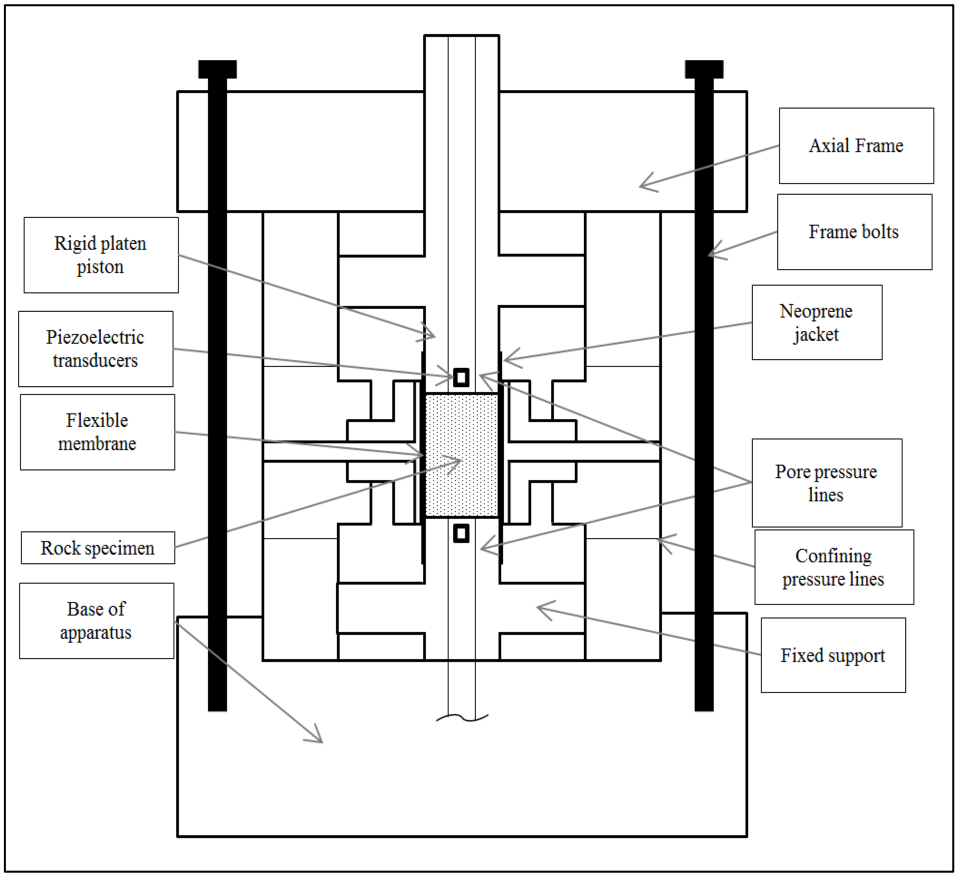

Figure 2.13: Schematic of UNGI true triaxial testing apparatus.

2.4 Laboratory Variation in Dynamic and Static Measurements

Stress-strain relations of rocks derived through laboratory testing often portray different elastic moduli than those calculated with elastic wave velocities, contrary to the linear elasticity theory. The former and the latter are known as static and dynamic moduli, respectively. The difference in the two types of moduli has been explored by studying poroelastic and viscoelastic properties of rocks, and has been largely attributed to the effects of strain magnitude and rate (Tutuncu et al. 1998, Fjaer 2009).

An important factor in the relation of laboratory measurements of wave velocity to static measurements of deformation is rate-dependency of rock stiffness. The difference in magnitude of observed stiffnesses between the two methods stems from a difference in the amount of strain created in the rock.

The phenomenon is amply described by the mechanism of squirt flow, or localized flow. Squirt flow is known as the localized oscillatory motion of fluid in thin pores or microcracks compressed under wave excitation, which minimizes energy dissipation, causing an apparent increase in rock stiffness (Mavko and Nur 1979).

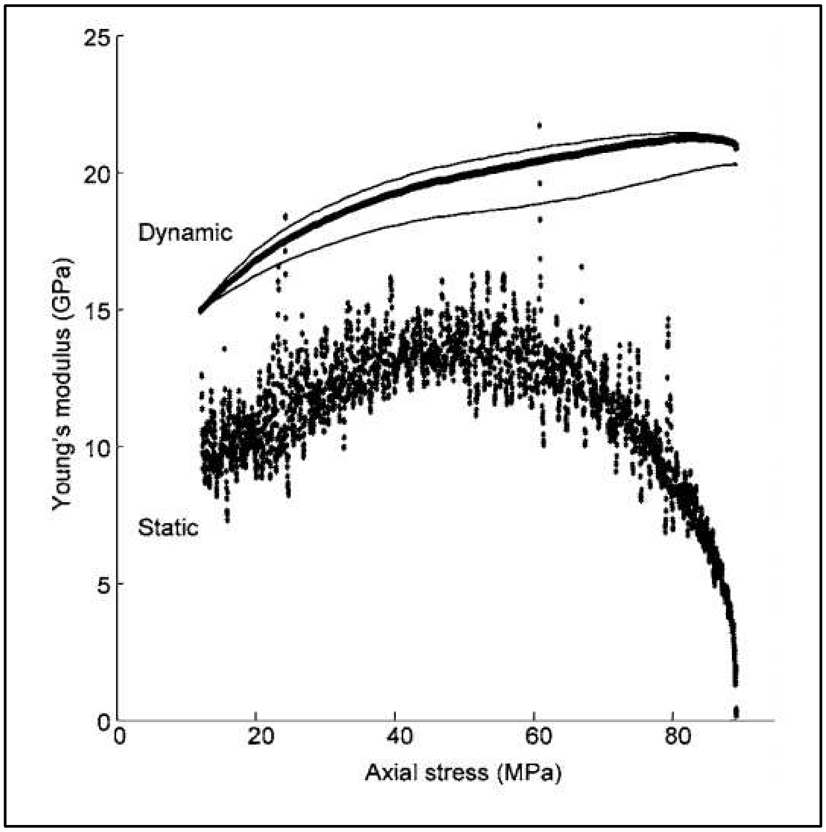

Figure 2.14: Static and dynamic Young's modulus response to axial stress in a triaxial test (Fjaer 2009).

It has been experimentally proven by Tutuncu et al. (1998a, b) that elastic moduli of dry and fluid-saturated sandstones exhibit larger magnitudes with higher frequency wave measurements, i.e. $E_{ultrasonic} > E_{log} > E_{lowfreq} > E_{static}$. Additionally, it was reported through uniaxial stress cycling tests that strain amplitude differences are the primary cause of variation between static and dynamic moduli, assuming viscoelastic frequency-dependent effects have been corrected for, with higher strain amplitudes resulting in smaller moduli. What had been concluded is that, even without the viscoelastic effects of squirt flow in dry rocks, strain amplitude effects exist in both high-strain static measurements and low-strain dynamic measurements of elastic moduli, and are the cause of, along with frequency, the differences between static and dynamic data.

Fjaer (2009) reported results of testing dry Castlegate sandstone specimens in uniaxial and triaxial compression, as well as the analysis of differences between static and dynamic moduli. The dynamic Young's modulus was found to be larger than the static modulus for all stresses in all triaxial tests. It was observed that the differences in strain amplitudes of static and dynamic measurements were most likely the cause of divergence in moduli, especially at higher stresses (Figure 2.14). During initial loading, both types of moduli increased with increasing stress. However, at higher stress magnitudes static moduli were decreasing, while dynamic moduli exhibited little sensitivity to stress change. Large strain amplitudes of static loading were linked to higher frictional sliding along microfractures, causing a decrease in static Young's modulus. Conversely, dynamic strain amplitudes were much lower than the static ones, leading to proportionally smaller dynamic moduli.

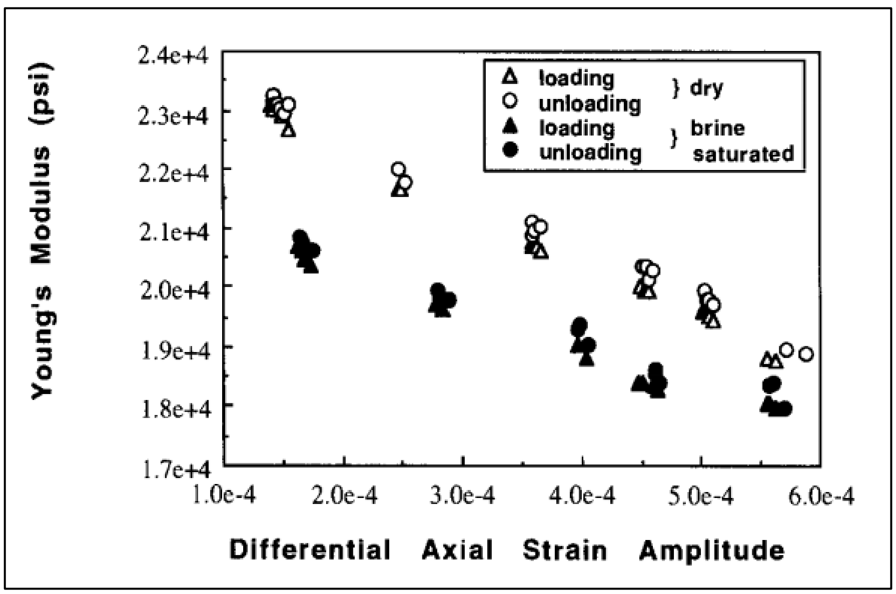

Figure 2.15: Young's moduli hysteresis during loading and unloading of dry and brine-saturated samples (Tutuncu et al. 1998b).

It was experimentally observed that fluid type also affects the strain amplitude dependence of elastic moduli (Tutuncu et al. 1998b). Using uniaxial stress cycling tests of Berea sandstone specimens in dry, brine-, and hexodecane-saturated states, the hysteretic strain behavior and the effects of fluid type on strain amplitude dependence were studied. Two additional samples were saturated with a solution containing CTAB, a cationic surfactant rendering grain surfaces hydrophobic, to explore the effects of stick-slip sliding and adhesion hysteresis on attenuation. The Berea samples tested had about 20% porosity and 600 md permeability. The resulting hysteretic behavior is visible in Figures 2.15 and 2.16, where loading and unloading of dry and brine-saturated samples results in slightly different Young's moduli.

Non-linear hysteretic behavior is seen in all specimens and saturations, with similar stress-strain relationships in dry and hexadecane-saturated states but different from those of the brine-saturated state. The CTAB-saturated states indicate higher axial strains and lower radial strains that any other states. The hysteretic behavior is explained by mechanical instabilities caused by cyclic movement of asperities between grain contacts, and frictional grain sliding. The theory of the process discusses that larger deformation during unloading is due to a different amount of forces that need to be overcome for a mechanical equilibrium to be maintained between grain boundaries. Presence of chain-like molecules such as CTAB causes an even higher hysteresis due to additional pull-off forces needed to break molecular entanglement, leading to a different stress-strain response.

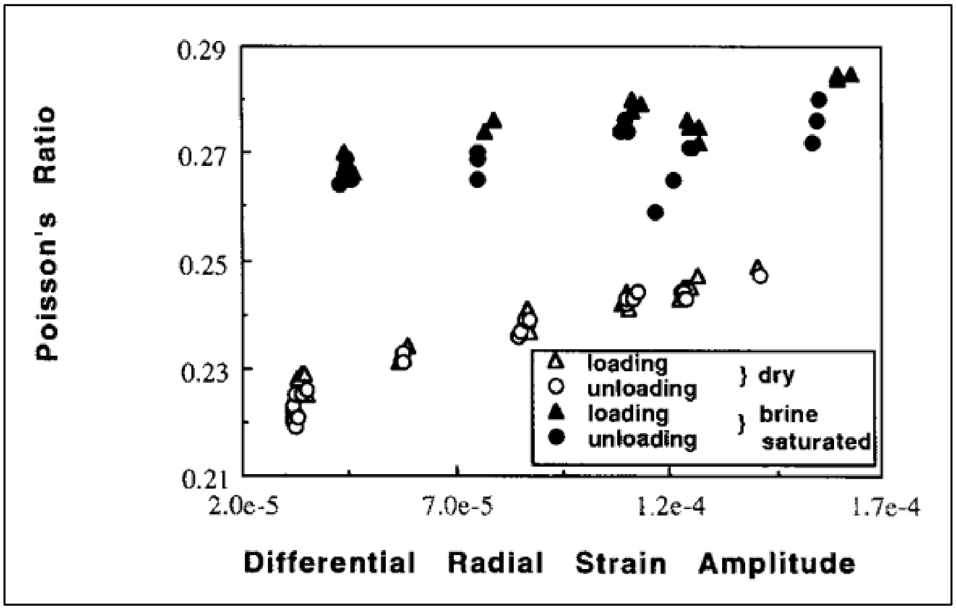

Figure 2.16: Poisson's ratios hysteresis during loading and unloading of dry and brine-saturated samples (Tutuncu et al. 1998b).

CHAPTER 3

METHODOLOGY AND MATERIALS

This project consisted of experimental true triaxial testing of Buff Berea sandstone samples in dry and water-saturated states with simultaneous measurements of compressional and shear wave velocities, axial deformation, and water permeability in axial direction.

The testing was performed with the UNGI true triaxial testing apparatus, which was first calibrated to ensure that no loading eccentricity, blank corner loading, or radial sample deformation restrictions were present. The experimental phase of the research performed, calibration of the apparatus and the measurement system, pore pressure installation for permeability testing, preparation of samples, loading method, setting up and testing procedures are discussed in this section.

3.1 Calibration of the True Triaxial Testing Apparatus

The calibration brought revisions of the original design as shown in Figure 2.13. The original version incorporated two sets of radial pad pistons, one with flexible membranes, and one with rigid metal platens. Together, the two sets form radial enclosure of a cylindrical sample where two radial directions are loaded with a rigid platen on one side and a flexible membrane on the other. This configuration can allow wave propagation measurements in two orthogonal radial directions. Initial experimental trials have indicated possible existence of loading eccentricity, friction along the axial faces of the sample, and difficulty of eliminating confining fluid invasion into the enclosed sample space. Another significant challenge was present in the calibration of radial wave propagation. Further calibration work and testing is expected to allow implementation of the original design, which would incorporate simultaneous measurements of wave propagation in three orthogonal directions.

In the adjusted configuration used in this study, the two radial rigid pistons were left inactive and the pistons containing flexible rubber membranes were implemented for loading in σ_2 direction, placed against each other. The sample faces in the σ_3 direction were consequently open to confining fluid pressure following this change of configuration. As shown in Figure 2.13, the only direction of loading using rigid platens is the axial direction, in which maximum principal stress, σ_1, is applied. As the radial pistons are pressurized, the metal frames surrounding the membranes are placed against the axial plates, effectively preventing the pressure of the radial pistons from being transferred onto the faces of the rock specimen. This allows fluid pressure within the membranes to create stress in the sample.

The center of the sample does not deviate from the center of loading in the axial direction because the sample is held by the fixed-support platen on the bottom and only the axial rigid platen is moved during the loading-unloading process, similar to the conventional triaxial systems. In order to prevent any loading eccentricity from the radial flexible membranes, equal pressurization of both membranes was ensured by connecting both pressure lines to a single ISCO syringe pump with 0.001 psi high accuracy. Radial pistons were also pressurized using one source, in order to equalize loading on both sides of the specimen.

The corner effect is not present in testing involving the UNGI true triaxial apparatus, because half of the cylindrical sample is appropriately encased by two opposite-facing flexible membranes along one of the two horizontal directions, while the other half is loaded with confining fluid pressure. Stress concentration effects from radial pistons are negligible since metal frames of the pistons are deterred from applying any stress to the sample by the axial rigid platens, limiting radial loading to confining fluid and flexible membranes.

The use of fluid pressure allows for unrestricted sample deformation in the radial plane since there is no frictional force between the sample and the surrounding fluid in the cell or membranes, warranting uniform boundary loading. Nevertheless, in order to ensure fluid pressure transmission throughout the sample faces in contact with membranes, water was injected into the membranes prior to testing. To confirm that an adequate volume of fluid necessary to contact areas of the sample closest to the metal frames was injected, a visual observation of the saturated membranes was made before setting up the apparatus, noting the expansion of the membranes. Later on, the fluid volume within membranes was adjusted according to the observation of piston LVDT displacement and pressure communication between membranes and the surrounding pistons.

The adjusted configuration of the radial pistons necessitated isolating flexible membranes from confining fluid to prevent fluid communication between the cell and the membranes. This was accomplished by sealing within and around the contact area between the neoprene jacket and the radial pistons with “3M Marine Fast Cure Adhesive Sealant”. Sealing was performed directly before apparatus assembly in order to bring the radial pistons to full contact with the jacket before tack-free curing of the sealant occurs. The neoprene jacket was previously degreased and lightly sanded to provide adequate adhesion. The described approach worked sufficiently during preliminary testing and was therefore applied for the samples used for the thesis study. The sealant was also used to isolate the rock sample from confining fluid, along with “Devcon H2 Hold Flexible Epoxy”. Both products were applied separately over top and bottom ends of the neoprene jacket in conjunction with sealing the radial pistons. The resulting sealing allowed for the anticipated testing to be performed without fluid communication to the sample being tested and any leakage in the system.

3.2 Sample Preparation

Cylindrical Buff Berea sandstone core plugs of 2” diameter were used in the experimental study. The samples to be measured were cut down to lengths nearing 3.5” with a core cutting saw in the Core Preparation Laboratory at the Colorado School of Mines Petroleum Engineering Department, without water lubrication during cutting to prevent any rock-fluid interactions that may alter the sample characteristics. Subsequently, the core lengths were brought down precisely to 3.5”, with accuracy of 0.001”, using a lathe in the College of Engineering and Computational Sciences Machine Shop at Mines. The end surfaces of the cores were uniformly smoothed to minimize stress concentration effects when in contact with the axial rigid platens.

The length and diameter were repeatedly measured, and then averaged to take into account the uncertainty of manual measurements. Each sample was weighed on a scale with resolution of 0.001 g.

3.3 Preparation and Calibration of Wave Measurements

The equipment used in measurements of acoustic wave propagation is listed as follows:

1. Two ultrasonic piezoelectric dual-mode transducers with natural resonance frequency of 1 MHz, custom-designed to fit inside the axial rigid piston and the fixed-support platen.
2. “Olympus Model 5058 PR” pulser/receiver.
3. “Tektronix TDS 2024C” four channel digital storage oscilloscope.
4. “Olympus” P- and S-wave transducer cables.
5. “LabView” computer software package to record waveforms and other geomechanical measurement data in real time.

The wave propagation was used in through-transmission mode wherein an electric signal travels from source to receiver transducer. The signal is sent from the transducer located below the core specimen, in the fixed-support platen, and received by the transducer in the axial rigid piston (Figure 2.13).

Travel time loss through the rigid platens was calculated by measuring through-transmission mode wave propagation face-to-face for calibration. The time delay was incorporated in the analysis of wave data by subtracting the face-to-face time from arrival time in the sample measurements shown in Chapter 4.

An acoustic couplant was used to assure full coupling of the transducers to the housing they sit in. The couplant used in the dry test was soluble in water, therefore, when the water-saturated measurements were conducted, it was replaced with “3M Marine Fast Cure Adhesive Sealant”. The latter, being resistant to water, proved appropriate as an acoustic couplant with waveform clarity comparable to the dry sample measurements.

The S-wave polarization remarkably impacted the shear wave data. Therefore, the experiments were performed with transmitter and receiver transducers oriented for 0 degree polarization for both tests.

3.4 Installation and Use of LVDT Transducers

Static measurements of axial deformation of the sample, as well as radial piston displacement, were made with three Linear Variable Displacement Transformer (LVDT) units. The transducers used were "Keyence GT2-P12K" stylus type high-precision sensor heads, with measurement range of 12 mm (0.47") and resolution of 1μm. All three sensors were mounted on the apparatus in the assembly orthogonal to the surfaces of pistons. The sensors were connected to the computer via a "Keyence GT2-100N" large display amplifier showing real-time displacement and used in conjunction with pump control units during testing for observation and recording of axial deformation response of the core samples to changing stress states. LVDT units were also mounted on the radial pistons and used to record piston movement in response to change in confining fluid pressure, radial piston pressure, and flexible membrane pressure, in order to adjust membrane volume accordingly.

3.5 Stress Loading Method

In exploration of the effect of true triaxial stress state ($\sigma_1 \geq \sigma_2 \geq \sigma_3$) on deformation and permeability anisotropy, this study aims at describing the influence of both magnitude and state of stress (e.g. hydrostatic or anisotropic). While it may be easier to analyze stress effects in conventional triaxial testing by considering only axial and radial stresses ($\sigma_2 = \sigma_3$ in conventional triaxial compression), the inclusion of intermediate principal stress σ_2 complicates the analysis of deformation, especially when many stress states are considered. In this study, a total of 91 different stress states are applied to both dry and water-saturated Buff Berea samples. Without a comprehensive method that separates the effects of stress state from the effects of stress magnitude, an approach that includes the effects of σ_2 would prove difficult in achieving the objective of this project.

The stress loading method used in this study consisted of simultaneous variation of three principal stresses to create and maintain constant octahedral normal stress σ_{oct}, while changing octahedral shear stress, τ_{oct}. The equations for octahedral stresses are shown below:

$$\sigma_{oct} = \frac{\sigma_1 + \sigma_2 + \sigma_3}{3} \tag{3.1}$$

$$\tau_{oct} = \frac{1}{3}\sqrt{(\sigma_1 - \sigma_2)^2 + (\sigma_2 - \sigma_3)^2 + (\sigma_3 - \sigma_1)^2} \tag{3.2}$$

Testing was performed on several different octahedral stress planes with cyclical variation of τ_{oct} within each plane. Eight different effective octahedral normal stresses have been implemented. They are: 100, 200, 300, 400, 500, 1000, 2000, and 3000 psi. Within each stress magnitude equal to or larger than 500 psi, the effective octahedral shear stress was varied from zero to a relatively maximum value, limited by either the octahedral normal stress or pump pressure capacity. This loading method allowed separation of stress magnitude from stress state, exemplified by σ_{oct} and τ_{oct}, and also the inclusion of σ_2 effects. The latter was accomplished with a nondimensional stress parameter b, which expresses the relative magnitude of σ_2 in relation to σ_1 and σ_3:

$$b = \frac{(\sigma_2 - \sigma_3)}{\sigma_1 - \sigma_3} \tag{3.3}$$

where $b = 0$ or $b = 1$ respectively illustrate triaxial compression ($\sigma_2 = \sigma_3$) and triaxial extension ($\sigma_2 = \sigma_1$) conditions. Movement towards the upper limit, where $b = 1$, corresponds to increasing intermediate principal stress. All three principal stresses were manipulated simultaneously for each loading cycle (the complete procedure of testing, including pump control, is described in section 3.6 below). The resulting combination of stresses designed for this study was illustrated in Figure 3.1 (a, b, and c), showing variation of stresses in three-dimensions. Initial hydrostatic stress conditions of 100, 200, 300, and 400 psi were not incorporated into octahedral shear stress cycling. Figure 3.1a illustrates the four octahedral stress planes, in which stress state was varied from hydrostatic to highly anisotropic. Octahedral shear stress, as seen in

Figure 3.1b, was varied significantly, with maximum magnitude of up to 1400 psi. For each octahedral stress plane considered, the octahedral shear cycling was repeated 5 times.

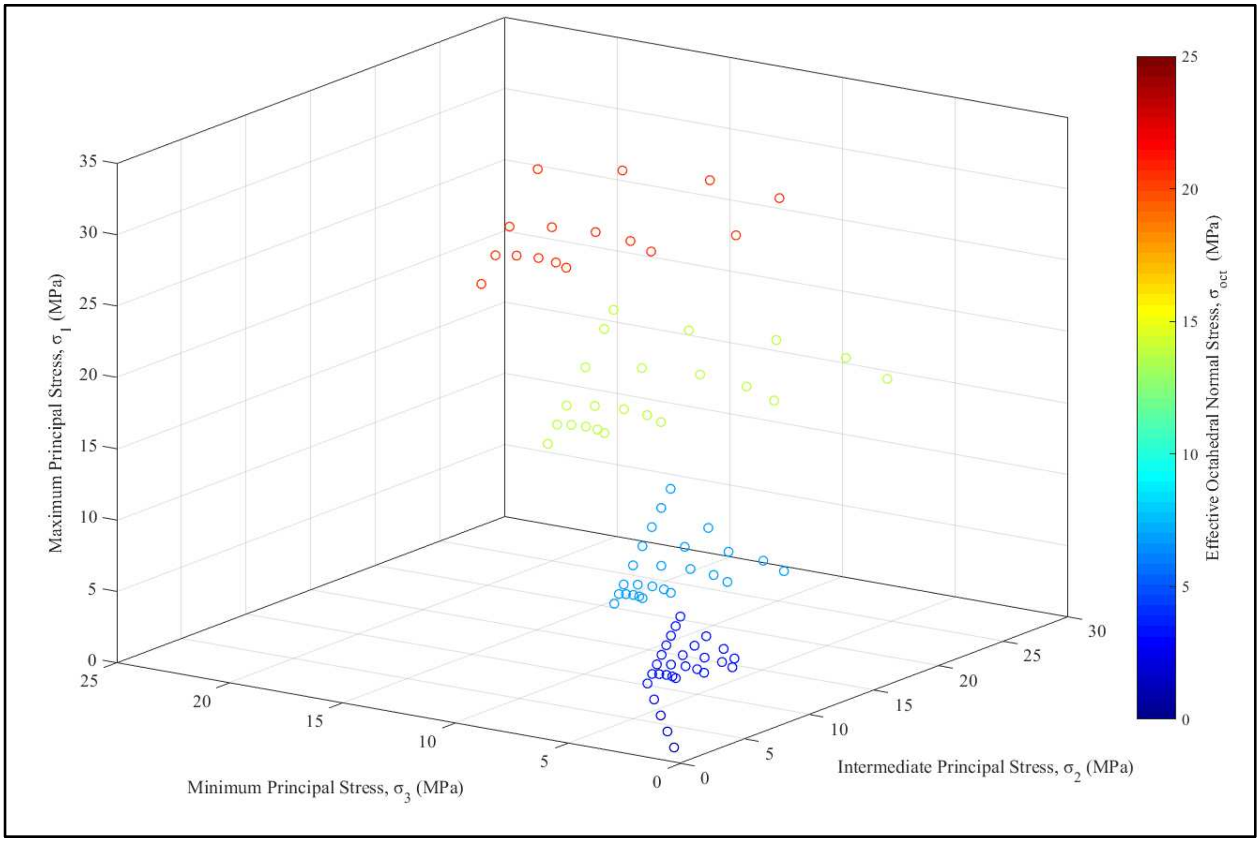

Figure 3.1a: Loading variation for dry and saturated Berea sandstone samples in 3D space. Shear stress cycling conducted in four octahedral stress planes: 500, 1000, 2000, and 3000 psi. The octahedral normal stress σ_{oct} magnitude is shown in the color bar (psi).

Cyclic loading was conducted to allow changes in stress parameter b. The parameter magnitudes incorporated into testing were 0, 0.25, 0.5, 0.75, and 1, signifying stress conditions with complete variation of σ_2: triaxial compression, general triaxial conditions, and triaxial extension (Figure 3.1c).

3.6 Setup & Testing Procedure

The true triaxial apparatus was assembled in a manner that suited the testing procedure, as described in previous sections of this chapter. High-vacuum grease was applied at the o-rings, or packings surrounding pistons, to prevent any fluid flow across the rings.

The vertical position of the fixed-support platen was adjusted to guarantee clamping of the platens by radial piston frames. The length of the neoprene jacket was also measured and prepared to cover the core specimen and axial platens, and to provide a seal with the platens. Sealant and epoxy were applied as described in section 3.1.

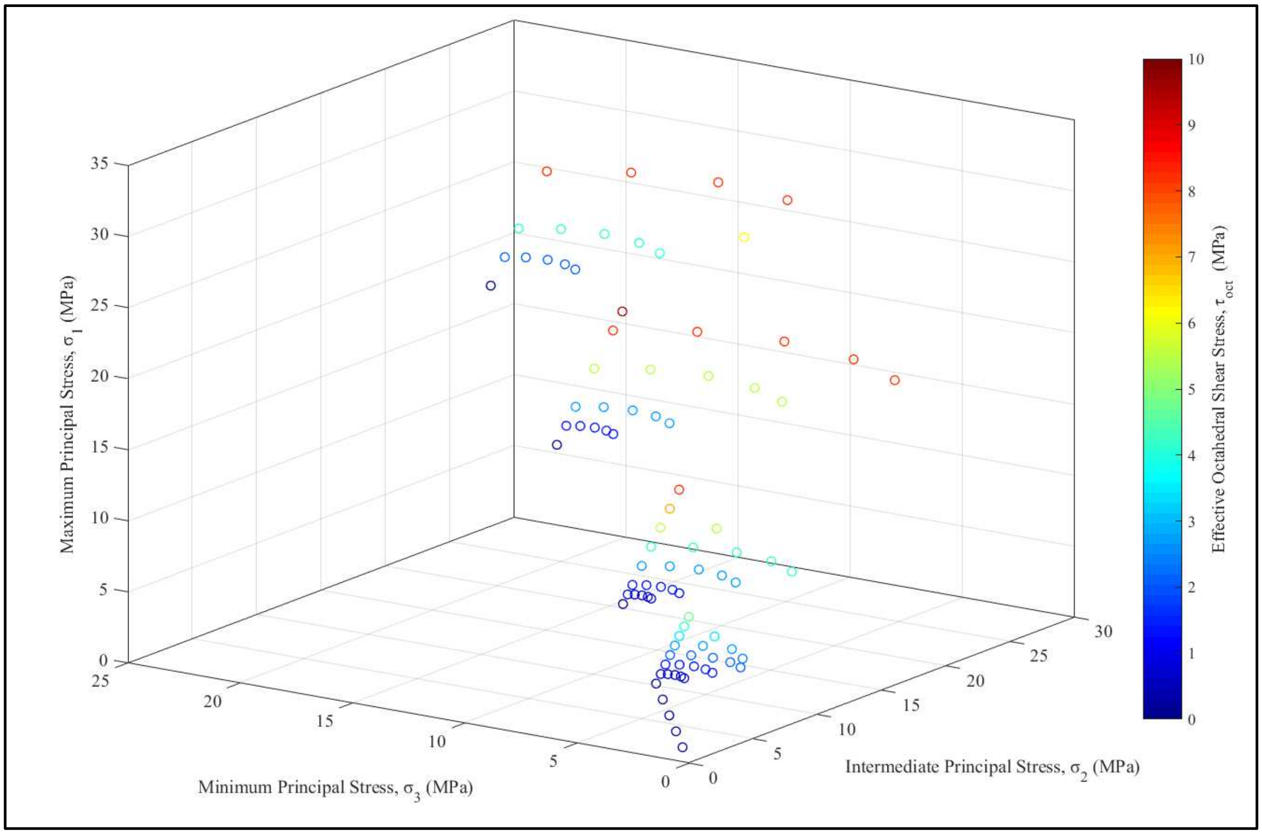

Figure 3.1b: Loading variation for dry and saturated Buff Berea sandstone samples in 3D space. The color bar shows octahedral shear stress variation (τ_{oct}) in psi.

Piezoelectric transducer alignment was made prior to securing transducers within axial platens for constant S-wave polarization. Upon assembly of the apparatus components, all LVDT sensors were manually mounted and then calibrated for positioning orthogonal to metal surfaces. After recording of displacement was initiated, a small degree of axial stress was applied to the sample and the pore space of the sample was vacuumed to ensure a tight seal of the neoprene jacket by the applied sealant and epoxy. Before tack-free curing occurred, radial pistons were pressurized to provide full contact between flexible membranes, sealant, and neoprene jacket. The pressure in the flexible membranes was increased in order to ensure proper pressure communication with the radial pistons and to adjust water volume in the membranes. Wave signal transmission was also checked to ensure clear wave propagation through the specimen. The apparatus was then left untouched for 3 days to ensure curing of sealant before testing.

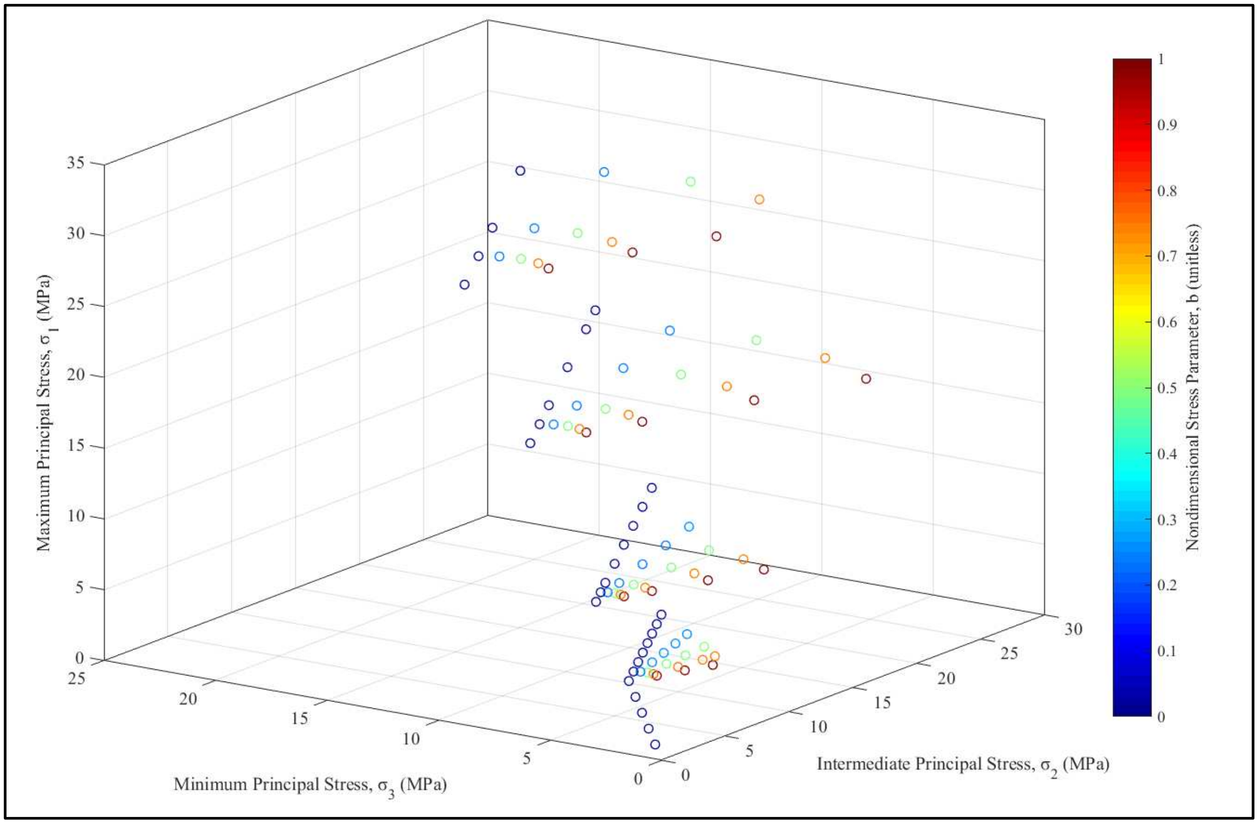

Figure 3.1c: Loading variation for dry and saturated Buff Berea sandstone samples in 3D space. The color-coding shows variation of nondimensional stress parameter b (unitless).

Testing commenced after injection of cell fluid into the apparatus. Injection was performed without prior vacuuming of cell volume, as air was allowed to exit the cell with continuous water injection. Injection was completed when a continuous stream of water was observed leaving the cell.

A total of 5 pumps were connected to the true triaxial apparatus, one for each of the functions listed below: axial rigid piston pressure (σ_1), confining cell pressure (σ_3), flexible membrane pressure (σ_2), radial piston pressure, and pore pressure. All the pumps used were part of "Teledyne Isco D Series" single-pump systems, each consisting of a controller and a pump module. Accurate pressure and flowrate control was necessary in the pore pressure system in order to run permeability tests, and in the flexible membrane-radial piston arrangement to control fluid volume in the membranes, therefore, pumps with high-precision flowrate and pressure were used.

Pump pressures and flowrates were controlled using a programmed pressure gradient function. This function allowed steady pressurization of different systems in the apparatus with constant flowrate. It was used to adjust pressures in the axial piston and the confining fluid in order to create the various stress magnitudes in the sample. The structure of the apparatus required keeping pressure changes in the axial piston and confining fluid corresponding to a certain relationship between the two pressures, because of confining fluid pressure acting on the flange of the axial piston. The approach of such pressure control is same in conventional triaxial testing, owing to similarities in design. Flexible membrane pressure was manipulated manually with either flexible membrane pump or radial piston pump, and was kept higher than confining pressure during all anisotropic stress states, since it was used to create intermediate principal stress in the core specimen.

Between any two cycles on an octahedral stress plane, the stress conditions were brought to the hydrostatic stress state ($\tau_{oct} = 0$) in order to return the strains in the sample to those before loading. Moreover, cyclic testing at different octahedral stress planes was performed over a course of several days, in both dry and saturated cases, with at least a 12 hour delay between changing the magnitude of σ_{oct}. During the delay, all stresses in the sample were brought down to about 300 psi σ_1 and 200 psi radial stress. It was conducted this way to minimize the influence of stress history on sample deformational behavior.

3.7 Permeability Testing

A system of pressure lines, valves, and vacuum lines connecting the apparatus, pore pressure pump, and a differential pressure transducer, was constructed in order to run several permeability tests throughout testing of the sample. Firstly, the sample was saturated with degassed deionized (or DI) water upon completion of apparatus assembly, checking the deformation response and the wave signal in the oscilloscope, as well as full curing of the sealant and the epoxy. A separate chamber containing deionized water was continuously vacuumed by the "Inficon QS5" two-stage, rotary vane vacuum pump over a period of several days in order to minimize the volume of air trapped within the water. The pressure difference between the ambient atmospheric pressure and vacuum pressure was 24-25 in Hg (11-12 psi) – the maximum vacuum pressure, as shown by the pressure gauge connected to the pump.

Subsequently to its degassing, the water reservoir was used to saturate the sample via gravity flow. The reservoir was placed at a higher position than the sample, which facilitated the flow of water to the sample owing to the pressure difference. Prior to saturation, the sample was vacuumed using the vacuum pump. In the saturation process, the flow of excess water leaving the pore space was observed in the transparent plastic line above the sample, indicating sample saturation. While intermittent air bubbles were also observed in the line, the ratio of air to water was seen decreasing during the process. Fluid flow was stopped when the water volume injected into the sample pore space was estimated to be larger than the pore volume by several orders of magnitude (i.e. 3 to 4). The resulting saturation level was deemed sufficient, assuming the permeability of the sample. Further saturation, if any, is assumed to have been achieved during pore pressure build-up using the pore pressure pump. It is, however, logical to expect that minor air presence persisted throughout initial saturation, owing to air remaining in the water chamber after extensive degassing, and air molecules present in the pore network upon vacuuming the sample pore space. Nevertheless, the potential air saturation is assumed to have been minimal during permeability tests causing water flow through the pore space.

Permeability tests were performed under both hydrostatic, e.g. 500 psi of octahedral normal stress, and anisotropic stress states (maximum applied shear stresses). Water flow was maintained in the axial direction, upwards from the bottom of the sample. Water was injected through two inlet pore pressure lines located in the fixed-support platen. The pore pressure line openings were equally spaced from the center of the sample, as shown in Figure 2.13. The outlet pore pressure lines were spaced in the same manner, located within the rigid axial platen. Before commencing flow, the inlet and outlet lines were also connected to "Veris Industries PW Series" wet differential pressure transducer (from here on referred to as 'DPT') with resolution of 0.01 psi. The full system of connections is illustrated in Figure 3.2. Each permeability test was performed under stabilized deformation conditions, warranted by absence of displacement in all three LVDT sensors and a stable acoustic waveform. The complete procedure of testing is described below:

1. At the start of the procedure, valves #1, 2, 5, 7, 8, and 9 were kept closed. Valves #3 and 4 were kept open. The pressure pumps for the rigid piston, radial pistons, flexible membranes, and confining pressure were running and maintaining the achieved stress conditions in the sample. Pore pressure of 100 psi was maintained (the pressure reading was cross-referenced between the pore pressure pump and the inlet pressure reading of the DPT). The vacuum air pump was turned off. The lines between the water trap and valves #5 and 7 were under vacuum.
2. If the pore pressure pump was previously refilled (maximum volume of approximately 68 mL), this step was omitted. It was necessary to maintain at least 40 mL of water in the pump to allow flow of water for the test. If pump needed refilling (i.e. pump volume was less than 40 mL), valve #4 was closed to maintain pore pressure at 100 psi. Afterwards, the pressure in the pump was brought to 10 psi and then stopped. The vacuum air pump was turned on; valves #9 and 5 were opened, which caused pump pressure reading to be negative (-11 to -12). Then, after several minutes to ensure vacuum in the lines leading to the pump inlet line, valve #2 was opened. After vacuum pressure was balanced, valves #5 and 3 were closed and #1 was open to allow the flow of degassed DI water to the pump. Later, the pump was set to refill, which moved the pump piston down to maximum volume position. To ensure full refilling of the pump, valves #1 and 2 were closed after 10-15 minutes. Consequently, pump pressure was increased to 10 psi and valve #3 was opened to allow pressure communication with the DPT. Pressure in the pump was adjusted to result in 100 psi reading in the DPT, if necessary. Pump pressure was then increased to pore pressure conditions of 100 psi (DPT reading) and valve #4 was opened. Subsequently, valve #9 was closed and the

vacuum air pump was turned off. The pump was effectively refilled with degassed deionized water and was run at 100 psi pore pressure.

3. The maximum flowrate limit in the pore pressure pump was adjusted to 10 mL/min.
4. The vacuum air pump was turned off and the vacuum pressure was released to ambient atmospheric pressure by opening of valve #8. The pressure reading in the lines was checked by observing the vacuum pressure gauge, which showed the ambient atmospheric pressure.
5. Valve #6 was opened to allow pressure communication between the DPT and the outlet pore pressure line. Pressure in the outlet and inlet was then stabilized, as shown by the DPT.
6. The DPT software used in the testing was turned on for logging and recording of resistivity versus time data for both inlet and differential pressures. The resistivity data was later converted into pressure.
7. The maximum flowrate limit in the pore pressure pump was then adjusted to 30 mL/min (a higher flowrate was not possible due to pump constraints).
8. Valve #7 was then opened to a small degree, allowing water flow into the water trap. The change of differential pressure and pump flowrate was observed. Once the flowrate and differential pressure were constant, a real-time display of resistivity vs. time in the DPT software computer exhibited a relatively constant resistivity value. After accumulating several minutes of data measurements, valve #7 was opened to a larger degree, thereby increasing the differential pressure on the DPT and the pump flowrate. The time for data recording was kept same after ensuring constant flow and pressure. Valve #7 was then opened more, with aim to achieve differential pressure around 10-12 psi, for which the flowrate was still well below maximum value of 30 mL/min. This differential pressure was estimated through trials to be achievable with the limited pump volume available, assuming that pressure and flow equilibration time increases with differential pressure. The time period for data recording at this stage was kept same as in previous stages. For each stage, pressure and flow equilibrium was ensured so that permeability calculations can be made with maximum accuracy.

9. Upon the completion of data recording, the DPT software was turned off. Then, flowrate limit in the pump was decreased to around 15-20 mL (without limiting actual flow). Valve #7 was closed slowly to prevent any drastic pore pressure changes in the rock sample by observing differential pressure and inlet pressure constantly. When flow was stopped, flowrate limit was brought down to 3-5 mL/min. Then, Valve #6 was closed.
10. Since flowrate and pressure data were recorded and stored in two different computers (one connected to the DPT and the second – to the pump control unit), time difference between the clocks of the two computers was recorded for calibration in permeability calculations.

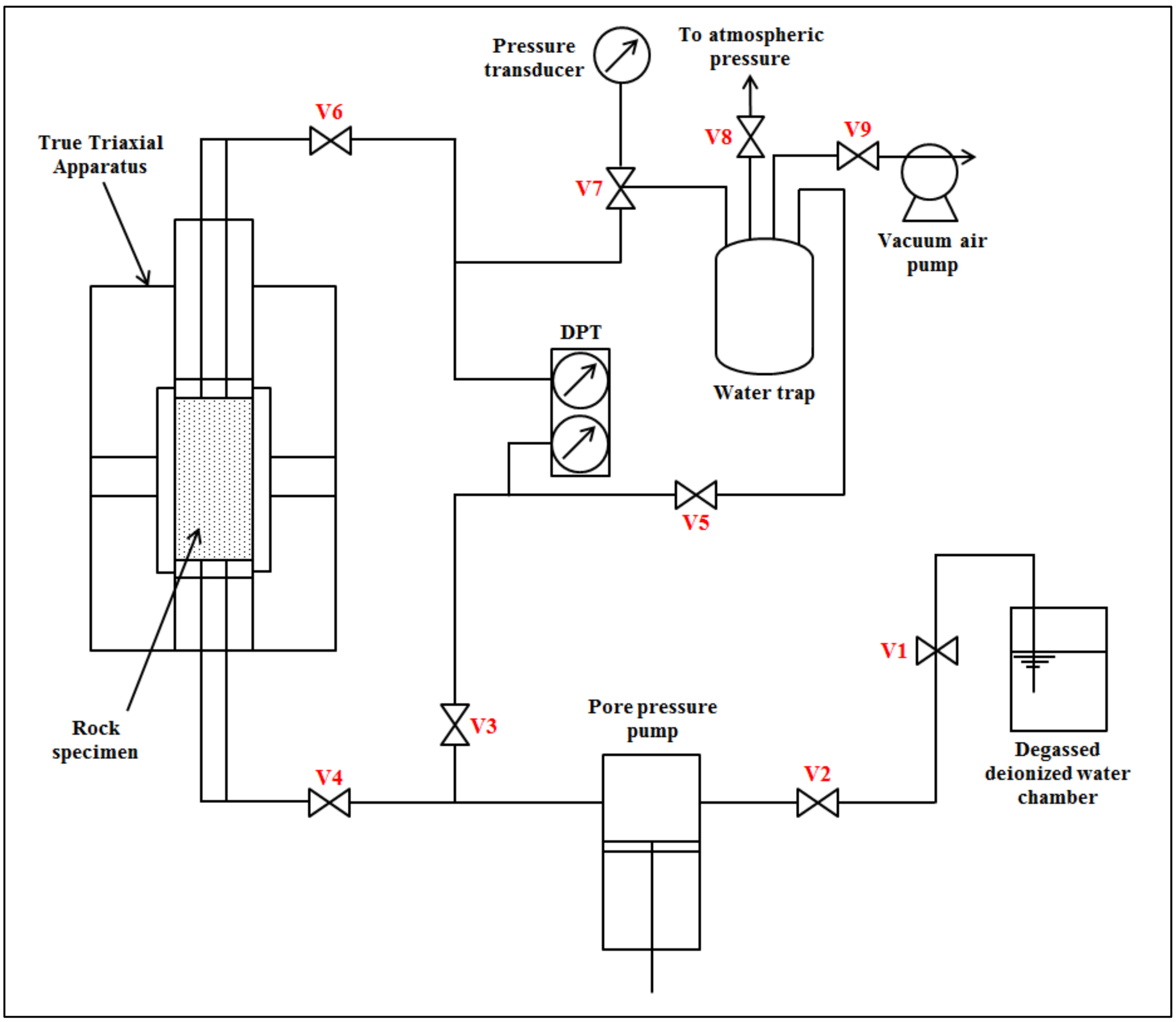

Figure 3.2: Diagram of permeability testing setup.

CHAPTER 4

RESULTS AND DISCUSSION

This chapter presents the results of the completed experimental work in the form of stress-strain curves, wave velocities, dynamic and static moduli, and permeability changes in the axial direction. X-ray CT scan images of the core samples used in this research study are provided in the Appendix. Analysis of the results is based on comparing and contrasting various data sources, i.e. wave propagation, strain, stress, and permeability. The discussion presented in this section concentrates on the following significant aspects: deformation differences in the core samples tested in dry and water-saturated conditions, differences between dynamic and static moduli, as well as effects of stress anisotropy and magnitude on permeability and sample deformation. A uniting deformational phenomenon derived from the results is also discussed.

4.1 Comprehensive Examination of Stress-Strain Curves

Both tests were performed in the same manner with only one difference in the form of pore pressure, implemented in the saturated case. The experiments were performed over similar timeframe (8 days for the dry sample and 6 days for the saturated sample), including all of the non-testing time, when the system was left overnight. During periods of no testing, the stresses were brought down to minimum (i.e. 0.69 to 1.38 MPa). Loading for the two tests was performed in the same manner, with stresses in the sample generated at constant pressure rate. The complete stress-strain curves incorporating effective octahedral shear stress (from here on, referred to as simply “shear stress”) and axial strain, are shown in Figures 4.1 and 4.2. The four clusters of loops represent the effective octahedral normal stresses (“normal stresses” from here on) of 3.4, 6.9, 13.8, and 20.7 MPa. It is worth mentioning that in order to maintain constant normal stresses for an array of shear stresses and values of *b*, at least two of the three principal stresses needed to be adjusted simultaneously.

For ease of comparison with works of other authors in the literature, units of stress are represented in megapascals instead of pounds per square inch (original data units), with unit notation for other variables also represented in respective SI units.

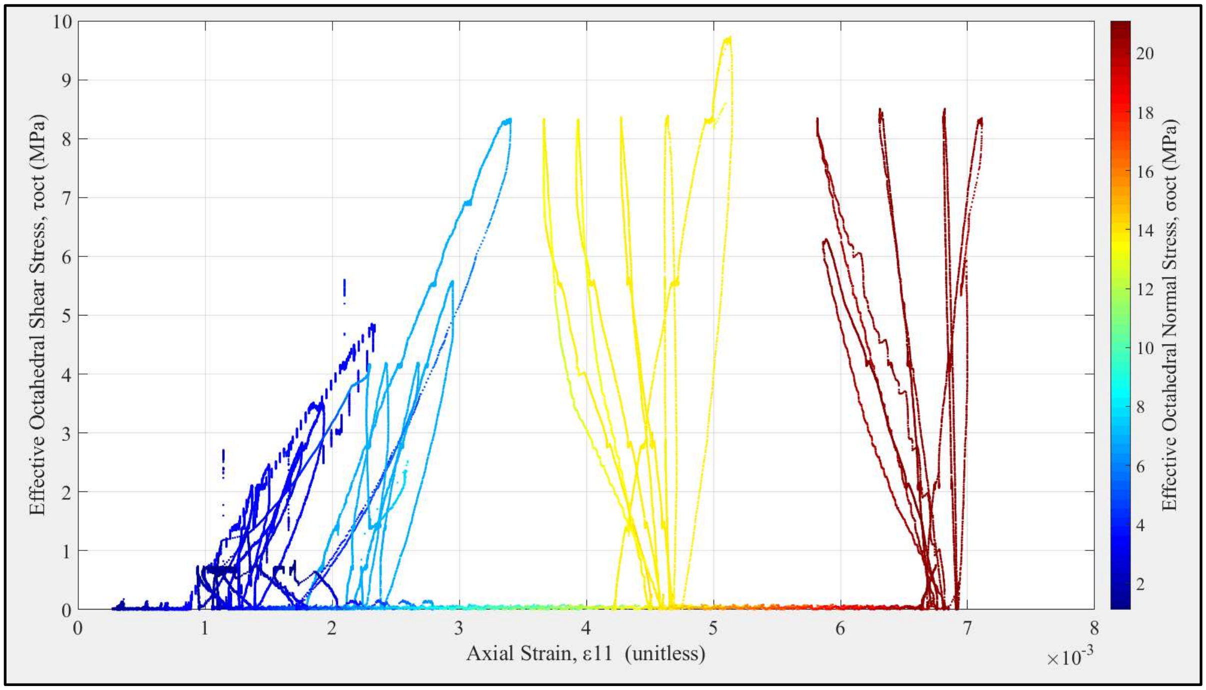

Figure 4.1: Complete stress-strain curve for the dry Buff Berea sample (color bar indicates variation in normal stress).

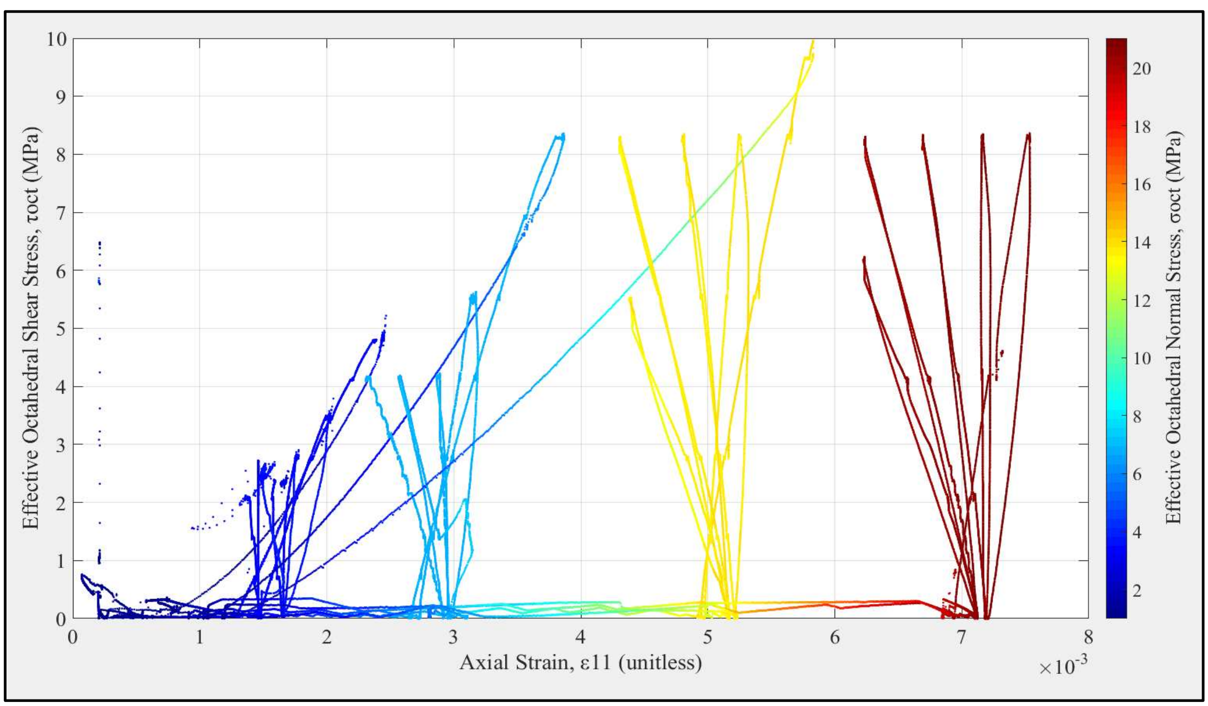

Figure 4.2: Complete stress-strain curve for the water-saturated Buff Berea sample (color bar indicates variation in normal stress).

As can be observed from the figures, hysteretic behavior was present in both tests, signified by loading and unloading stress-strain curves following different paths. A smaller degree of hysteresis is seen in the saturated case. The dry case exhibits somewhat distorted stress-strain curves in the first two clusters, whereas the saturated case indicates distortion in the first cluster. With higher normal stress applications, the strain response becomes clearer for both cases. A marked increase in strain can be noted in the saturated sample test from the strain measured for the dry sample when the sample is subjected to various hydrostatic stress states ($\tau_{oct} = 0$).

Each stress-strain loop in individual cluster corresponds to a specific constant b value for that loop, beginning with the smallest value of $b = 0$ in the right loop and progressing toward the left. The increase in b corresponds to lower axial strain. Furthermore, starting with $b = 0.5$, strain reversal begins proportional to the value of b for each following loop in most of the clusters reported in this study. At higher values of b, the largest magnitude of octahedral shear stress at a constant octahedral normal stress decreases, owing to the increase of intermediate principal stress σ_2. This illustrates why maximum shear stresses for the triaxial compression loops ($b = 0$) stand out from the maximum stresses in all subsequent hysteresis loops.

The stress-strain diagrams shown above were reproduced using only the stress and strain values corresponding to the wave measurements and more clearly illustrate the slopes of each individual curve (Figures 4.3 and 4.4). At $b = 1$, the condition where intermediate and maximum principal stresses are equal, the magnitude of the stress-strain curve slope is roughly the same or greater than the slope at $b = 0$ for normal stresses of $\sigma_{oct} = 13.8$ and 20.7 MPa in both tests. The strain reversal at high values of b is shown to counteract the strain generated by normal stress. At normal stress of 3.4 MPa in the dry sample scenario, however, no strain reversal occurred, i.e. the slopes of loading and unloading curves were positive. The next normal stress of 6.9 MPa a reversal of axial deformation took place only under $b = 1$.

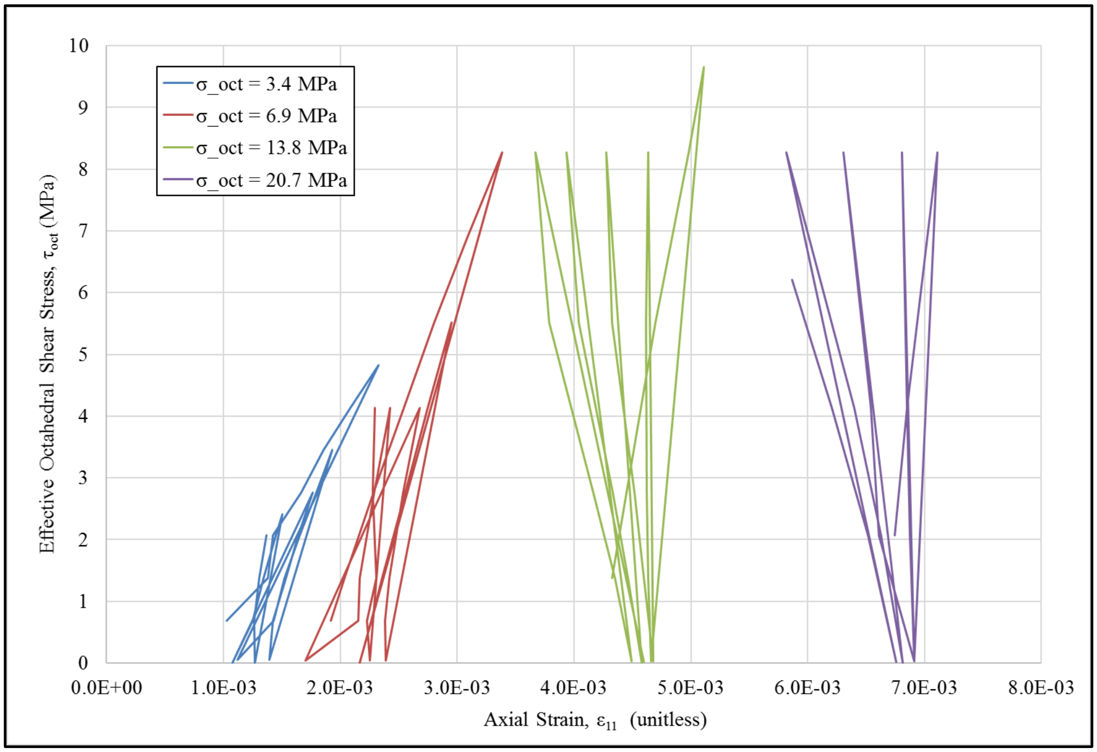

Figure 4.3: Simplified stress-strain curve for dry Buff Berea sample. Only the data points for step changes in stress magnitudes and states are used.

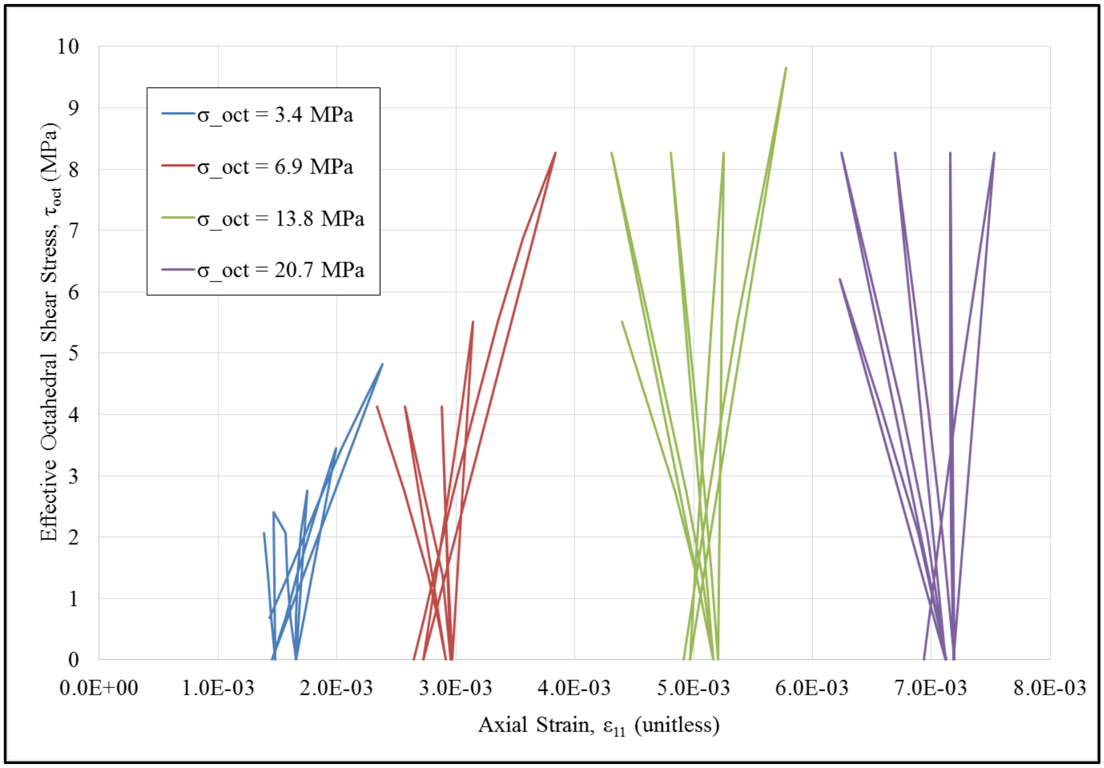

Figure 4.4: Simplified stress-strain curve for saturated Buff Berea sample. Only the data points for step changes in stress magnitudes and states are used.

Permanent strain generation can also be recognized in the stress-strain curves after unloading of the stress loops. The location of the initial strain at the beginning of a particular loop is different for different stress hysteresis loops within the same cluster. This behavior is present in both dry and saturated scenarios.

It should be noted that strain rate is highest under normal stresses of 3.4 MPa and gradually decreases with increasing normal stresses. This behavior is present in both tests and is most likely associated with initial closures of microfractures in the samples. As more closures occur, the sample becomes stiffer under larger normal and shear stresses. It is also observed in the dry sample test that strain is positive at $b > 0.5$, while the saturated sample displays a relatively small negative slope at $b = 1$.The logical deduction follows that early-stage microfracture closures under increasing σ_2 diminish its effects on axial strain. Owing to microfractures closures in the planes parallel to maximum and intermediate stresses, lateral straining from σ_2 does not communicate well with axial straining by σ_1 at low normal stress.

4.2. Wave Velocity Response

The propagation of acoustic waves through the samples is an integral part of the experimental results in this study and therefore, it was given careful attention in terms of wave velocity measurements. The arrival times for compressional and shear waves in through-transmission were estimated in groups with various waveforms plotted together for higher accuracy. Changes in waveform frequency and amplitude were incorporated in the velocity determination. The estimation approach for P-wave arrivals was kept same for the two tests. The S-waves were analyzed slightly differently than P-waves, but in the same manner for the two sets of data. It should be noted that there always exists a small degree of uncertainty stemming from differences in manual approach of picking arrival times. Such uncertainty in the data is acceptable assuming that error is consistent and the approach is comprehensive and constant throughout the analysis of waveforms. The velocity values were calculated by taking into account static strain of the samples at each consecutive stress condition.

The changes in calculated P-wave velocities under the stress state conditions applied for the two samples are shown in Figures 4.5-4.8 below. Figures 4.5 - 4.8 illustrate the effects of stress conditions on P-wave propagation in tests of dry and saturated samples. Velocities increase with higher normal and shear stresses. A noticeable and consistent difference in velocities across the tests is the higher velocity magnitude in the saturated case. Nevertheless, both datasets show a similarity in velocity trends corresponding to different *b* values under all normal stresses. The effect of *b*, while still present, diminishes for the saturated scenario, signifying a smaller sensitivity to the intermediate stress effect. Still, it can be concluded from the data that P-wave velocity is inversely proportional to the changes in the non-dimensional stress parameter. While there is minor overlapping of velocity profiles corresponding to specific *b* values, the general trend of decreasing velocity with increasing *b* is clearly visible.

At lower constant normal stresses of 3.4 and 6.9 MPa, there exists a larger variation in velocity response to shear stress, which becomes a more stable slope at higher stress levels of 13.8 and 20.7 MPa. Dry case velocities exhibit magnitudes in the range of 2.77 - 3.37 km/s, while the saturated velocity range is 3.18-3.57 km/s. The differences in average velocity show the same response to the applied normal stress (Figure 4.9). As pore pressure in the core rises, the pore fluid, in our case water, provides another medium for compressional wave propagation in addition to the rock matrix filling the pore space and making the bulk density higher compared to the dry case where pores are filled with air. Since water is relatively incompressible under the stress states implemented in the experiment, it improves transmission of the acoustic wave, and combined with increased density, results in a higher velocity. It should be highlighted that pore pressure was maintained in the "drained" condition throughout testing of the saturated sample, signifying that the volume of fluid in the sample was continuously adjusted to maintain constant pore pressure. The S-wave velocities are shown in Figures 4.10-4.13 in the same order as the compressional wave velocities. An opposite response to the saturation is observed - shear wave propagation is consistently slower in the saturated case than in the dry case. Another significant change from compressional velocities is the increased variation and inconsistency of the velocity response to *b* value between the two tests.

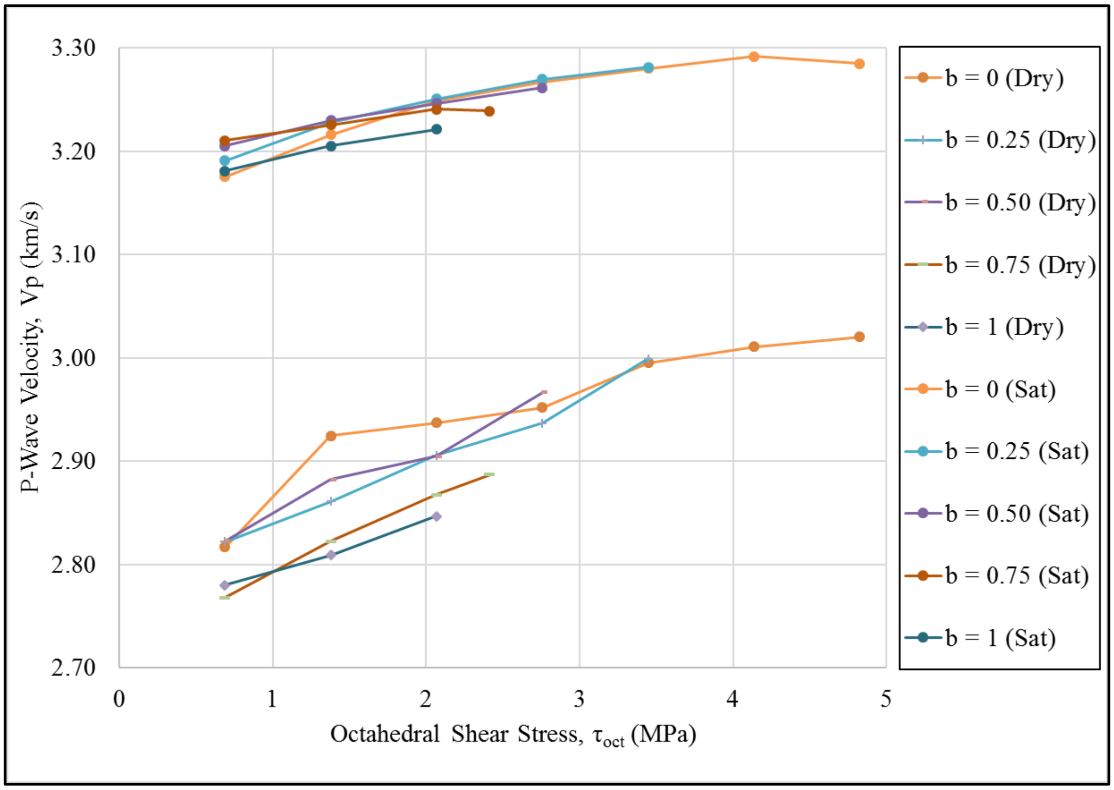

Figure 4.5: P-wave velocity variation with shear stress at constant normal stress of σ_{oct} = 3.4 MPa, with different values of b for dry sample (Dry) and saturated sample (Sat).

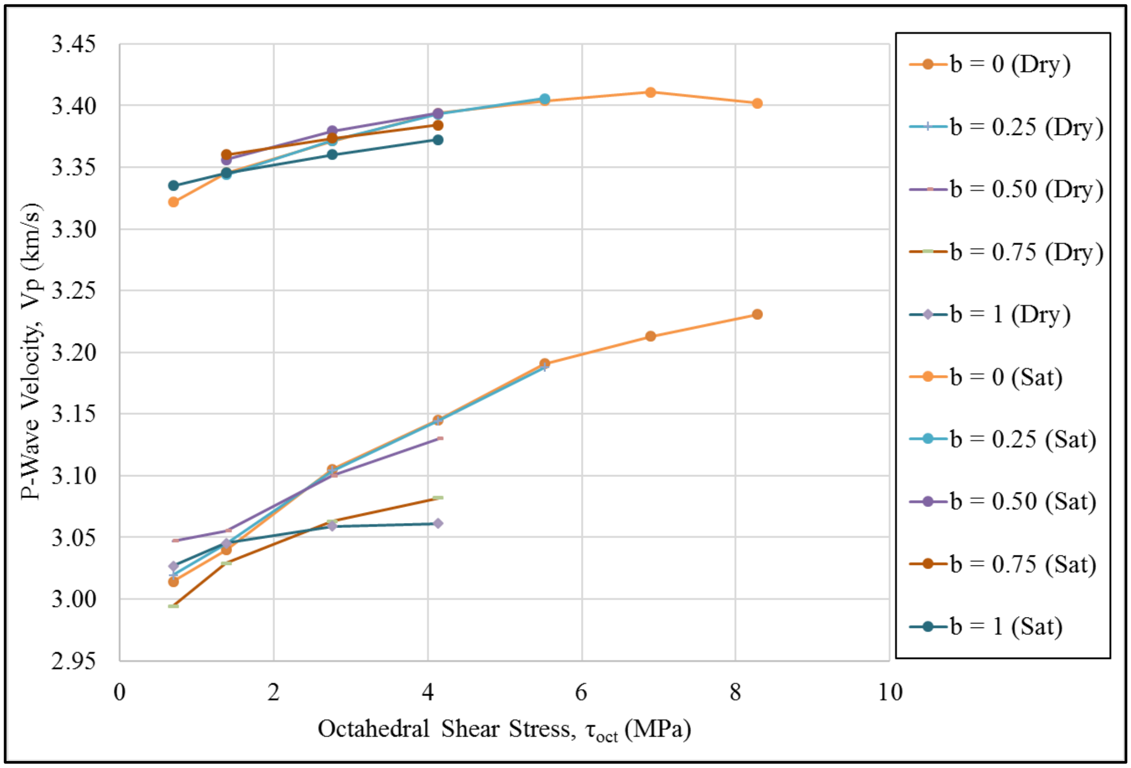

Figure 4.6: P-wave velocity variation with shear stress at constant normal stress of σ_{oct} = 6.9 MPa, with different values of b for dry sample (Dry) and saturated sample (Sat).

The difference in response originates from inconsistency in the dry sample velocities across different normal stresses. For instance, in Figure 4.10, the velocity profiles at $b = 0$ for the saturated and dry cases show opposite behavior, yet in Figure 4.11 the behavior is similar. Shear wave velocities for the saturated condition illustrate the same response to b at different normal stresses. It follows then, that shear wave velocity in the saturated case is directly proportional to b. Dry velocities, conversely, do not display a consistent relationship with the stress parameter, due to variation in velocity profiles corresponding to $b = 0$ and $b = 0.25$. Other velocity profiles for the dry sample express directly proportional response to stress parameter changes.

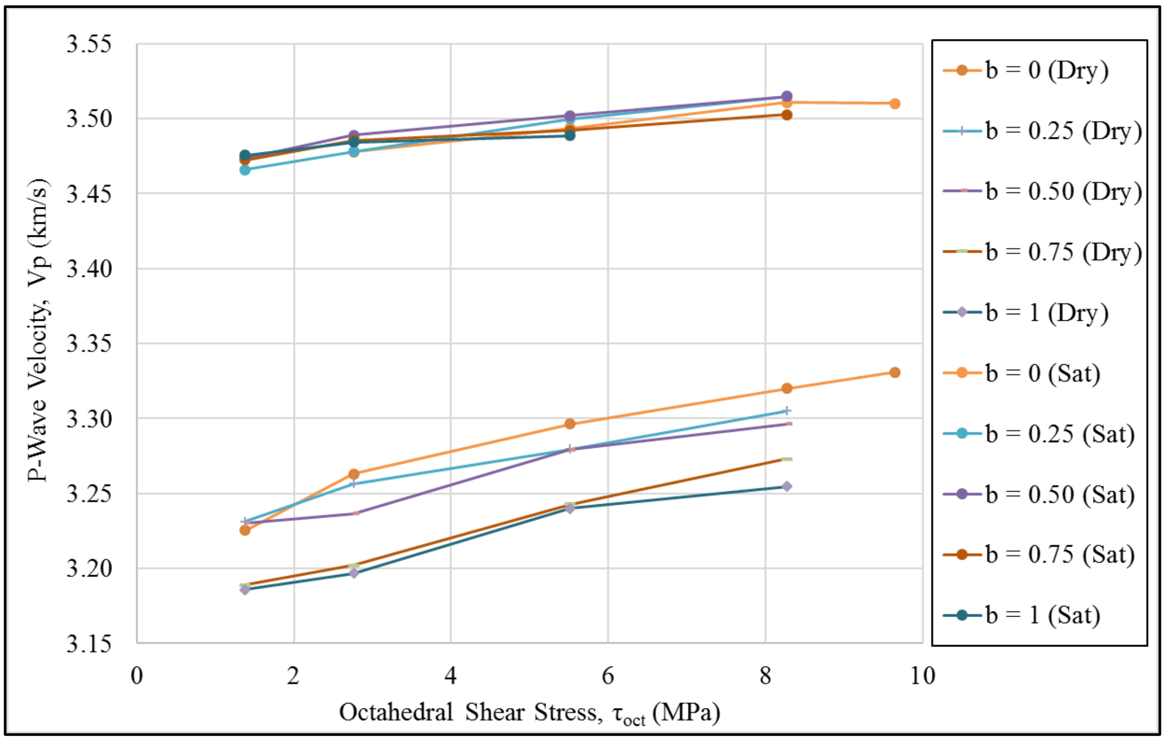

Figure 4.7: P-wave velocity variation with shear stress at constant normal stress of $\sigma_{oct} = 13.8$ MPa, with different values of b for dry sample (Dry) and saturated sample (Sat).

This interesting velocity response to stress state and magnitude is a result of stress-induced anisotropy of deformation. As mentioned in Chapter 2, deformation of sandstone involves closing and opening of microfractures, or small high aspect ratio cracks, under both hydrostatic and anisotropic stress conditions.

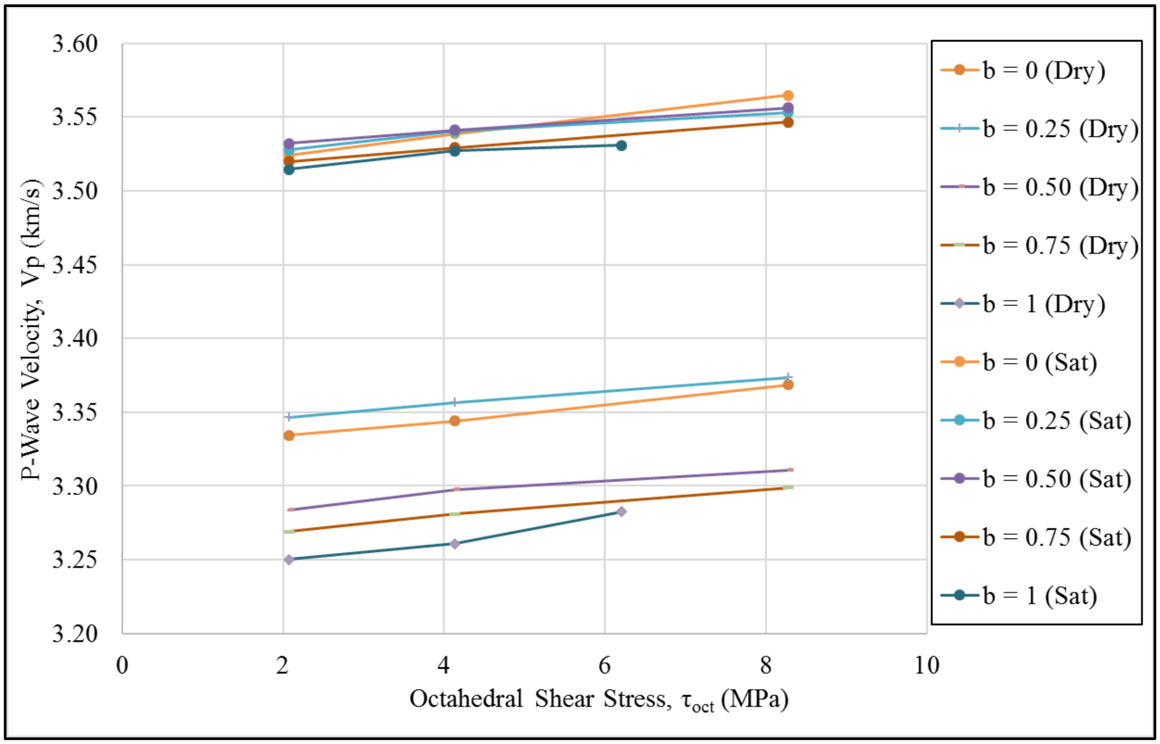

Figure 4.8: P-wave velocity variation with shear stress at constant normal stress of $\sigma_{oct} = 20.7$ MPa, with different values of *b* for dry sample (Dry) and saturated sample (Sat).

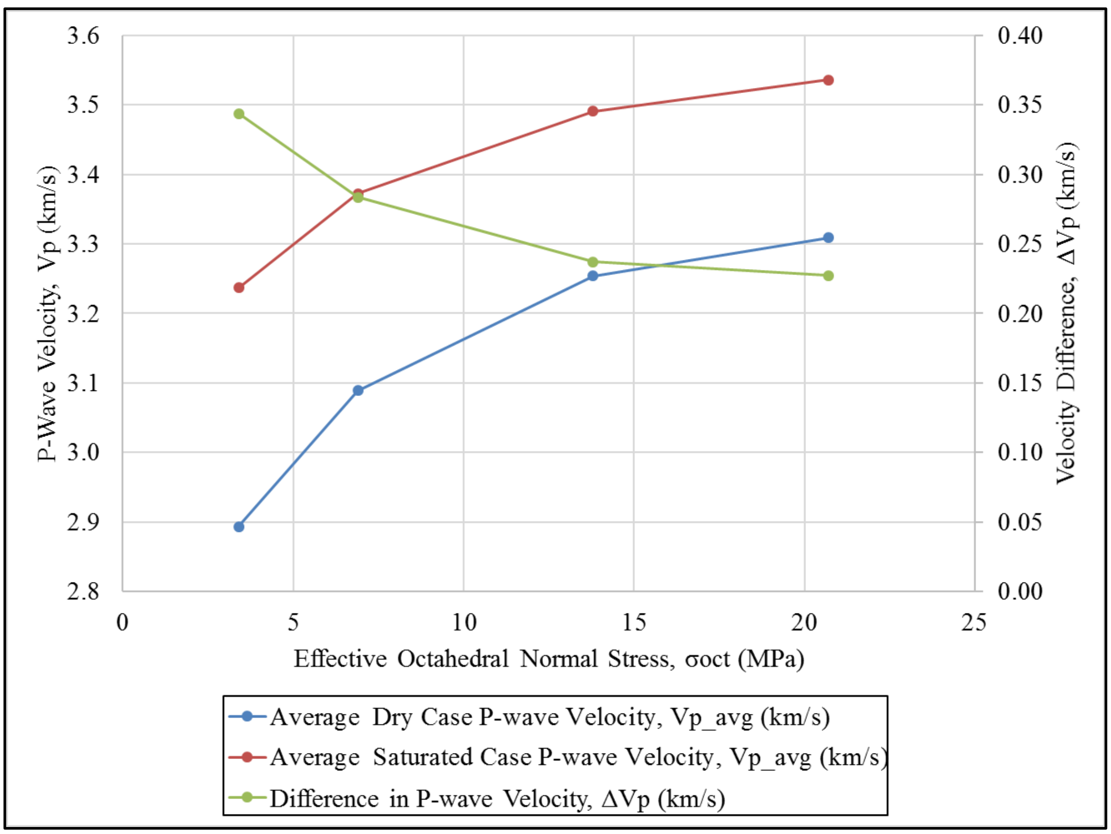

Figure 4.9: Difference between average P-wave velocities for dry and saturated samples.

In the former, all randomly oriented microcracks begin collapsing since stress is uniform in three directions. However, under anisotropic stress conditions, microfractures oriented normally to the maximum stress direction will close, while those oriented along the direction will be forced to open. Moreover, with increasing intermediate principal stress physical changes to microfractures become more complex. The increase in b parameter indicates an increase in the magnitude of intermediate principal stress relative to maximum and minimum stresses. As b rises it causes a higher degree of closure in microcracks oriented normal to the σ_2 direction. Because S-waves are polarized in the plane parallel to the direction of intermediate stress, as was mentioned in Chapter 2, the medium of wave propagation becomes denser as microcracks are closed. The dry sample scenario illustrates a varying response from S-wave velocity to increasing stress parameter. At normal stresses of 3.4 MPa, when $b = 0$, velocity experiences an initial rise, followed by a decrease in magnitude at higher shear stresses. Corresponding to these stress changes in the sample is a large increase in axial strain, as illustrated by Figure 4.3. An important feature in deformation profiles of both samples is that axial strain at $\sigma_2 = 3.4$ MPa is largest throughout both tests, as shown by the slope of the stress-strain curves. Within this first cluster of the stress-strain loops, the straining of the samples is largest at lowest b, which is also the case for other cycles at higher normal stresses. In each stress-strain cluster, as b increases, axial strain is diminished. Firstly, this behavior supports previous findings that σ_2 increase in a general stress state counteracts the strain generated by σ_1, even at decreasing σ_3 magnitudes. Secondly, as it applies to S-wave propagation during triaxial compression, the shear stress increase is warranted by a larger difference between maximum and minimum stresses. With decreasing confining pressures, naturally, the stress state becomes increasingly uniaxial, causing closure of microfractures oriented aligned to maximum stress direction and unrestricted lateral expansion. Consequently, as microfractures oriented parallel to S-wave polarization plane are enlarged, the medium of wave propagation becomes less dense, resulting in lower S-wave velocity. This velocity trend is observed at the smallest normal stress. Higher normal stresses result in smaller variation of velocity with shear stress. There, the increase in shear stress incorporates larger confining stresses at $b = 0$, causing a smaller degree of lateral expansion, and therefore a smaller change in S-wave velocity. As the stress parameter increases, lateral expansion becomes more limited in the σ_2 direction, followed by a later reversal into lateral strain, as signified by the stress-strain curves in Figures 4.1 and 4.2.

Again, the S-wave propagation medium becomes denser, explaining the directly proportional response to b. The nonconforming response is seen in dry velocities at normal stress of 6.9 MPa, where the b effect is more negligible. The response of average velocity to increase in normal stress (Figure 4.14) is relatively the same for both dry and saturated tests.

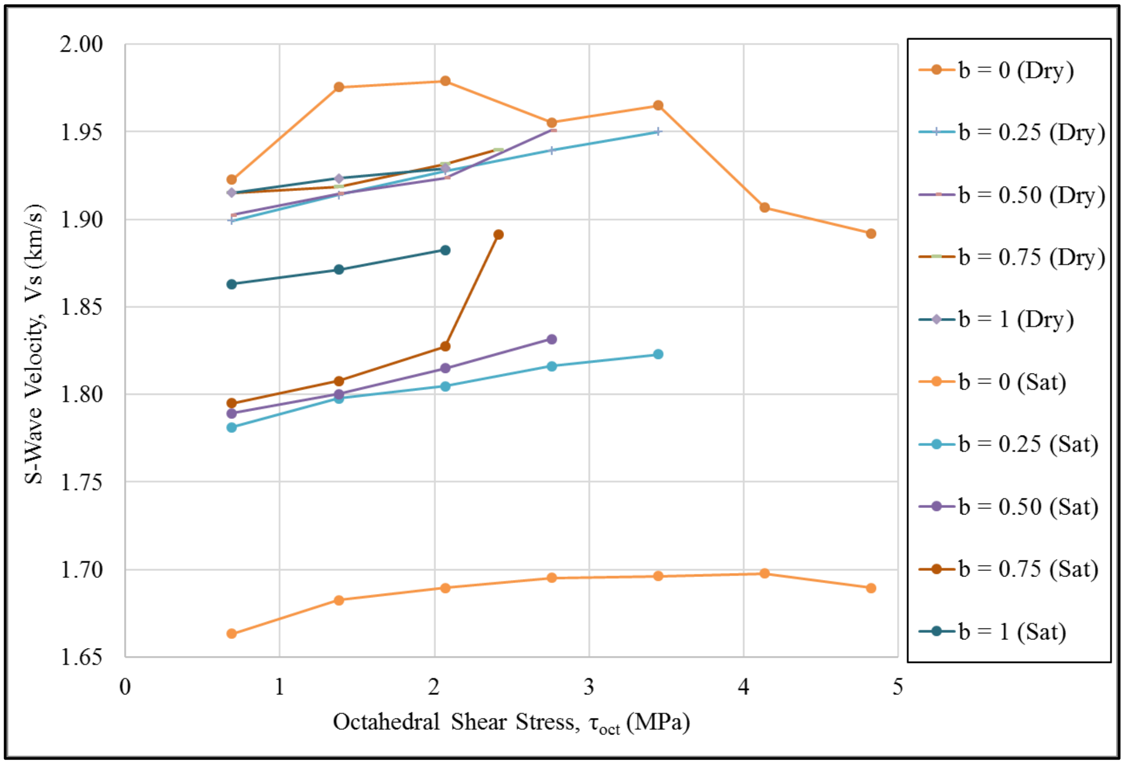

Figure 4.10: S-wave velocity variation with shear stress at constant normal stress of $\sigma_{oct} = 3.4$ MPa, with different values of b for dry sample (Dry) and saturated sample (Sat).

Discrepancy in S-wave velocities can be better observed by combining S- and P-wave velocities in terms of V_p/V_s ratios. The compressional to shear velocity ratio has been proven as an indicator of lithology in both laboratory experiments and sonic logs, as well as exhibiting relative independence from effective stresses or pore volume changes (Pickett 1963).

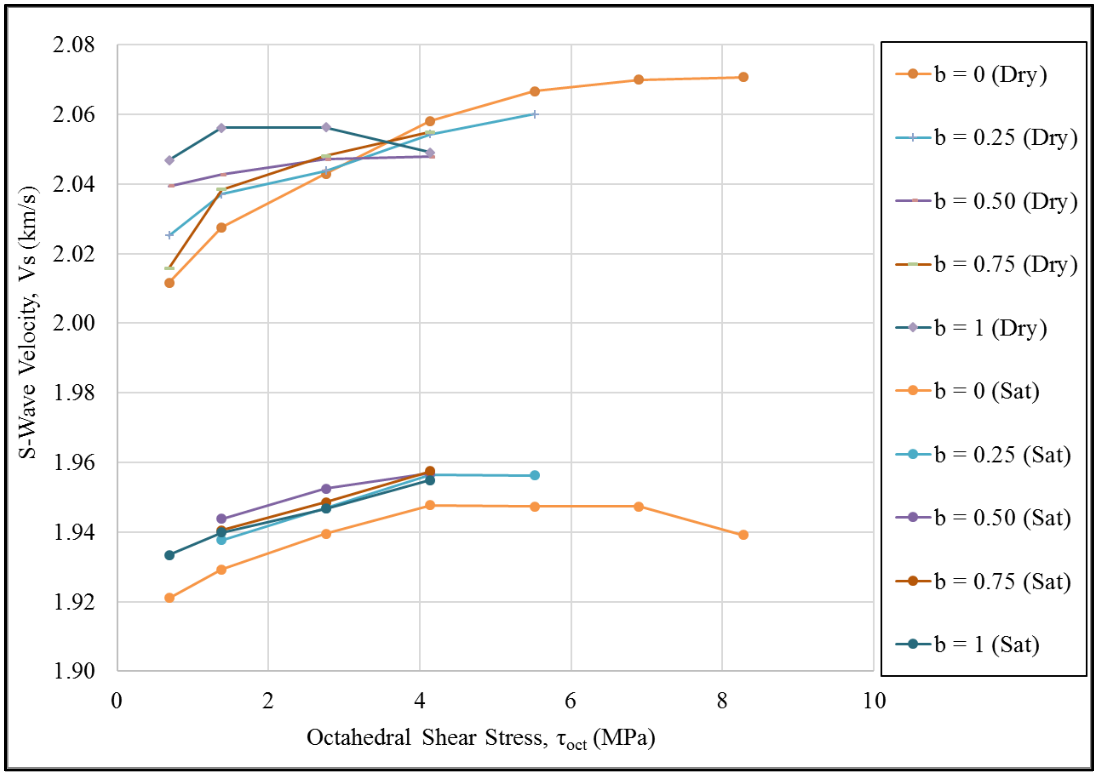

Figure 4.11: S-wave velocity variation with shear stress at constant normal stress of σ_{oct} = 6.9 MPa with different values of b for dry sample (Dry) and saturated sample (Sat).

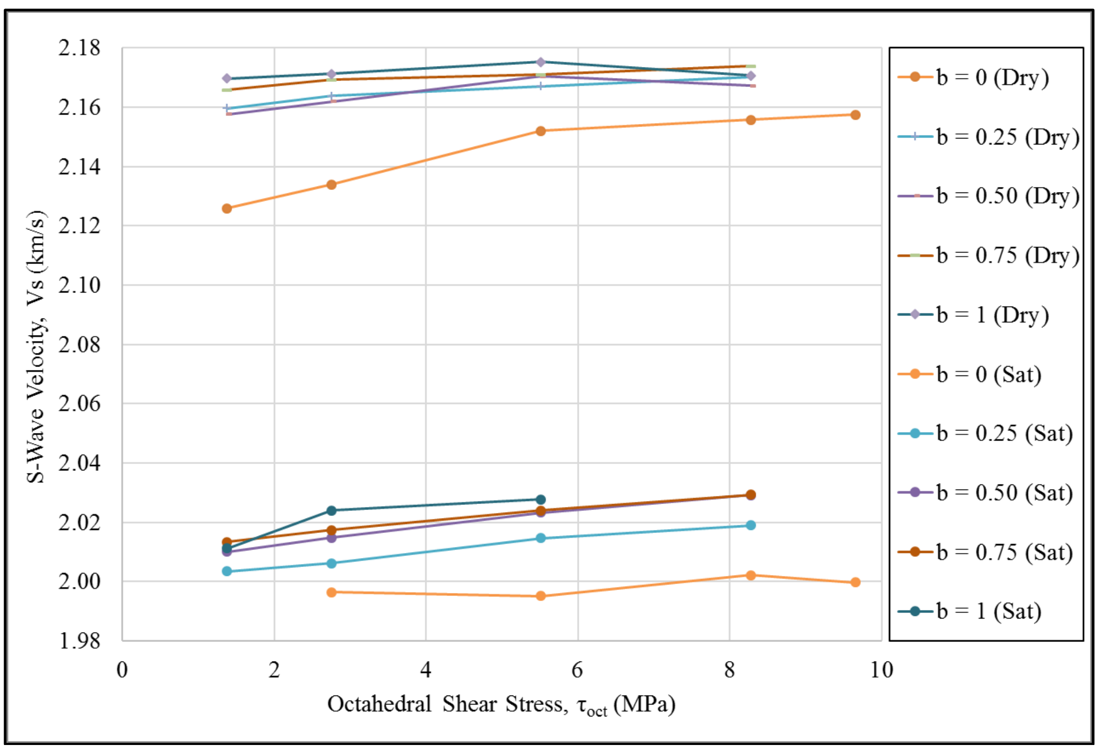

Figure 4.12: S-wave velocity variation with shear stress at constant normal stress of σ_{oct} = 13.8 MPa with different values of b for dry sample (Dry) and saturated sample (Sat).

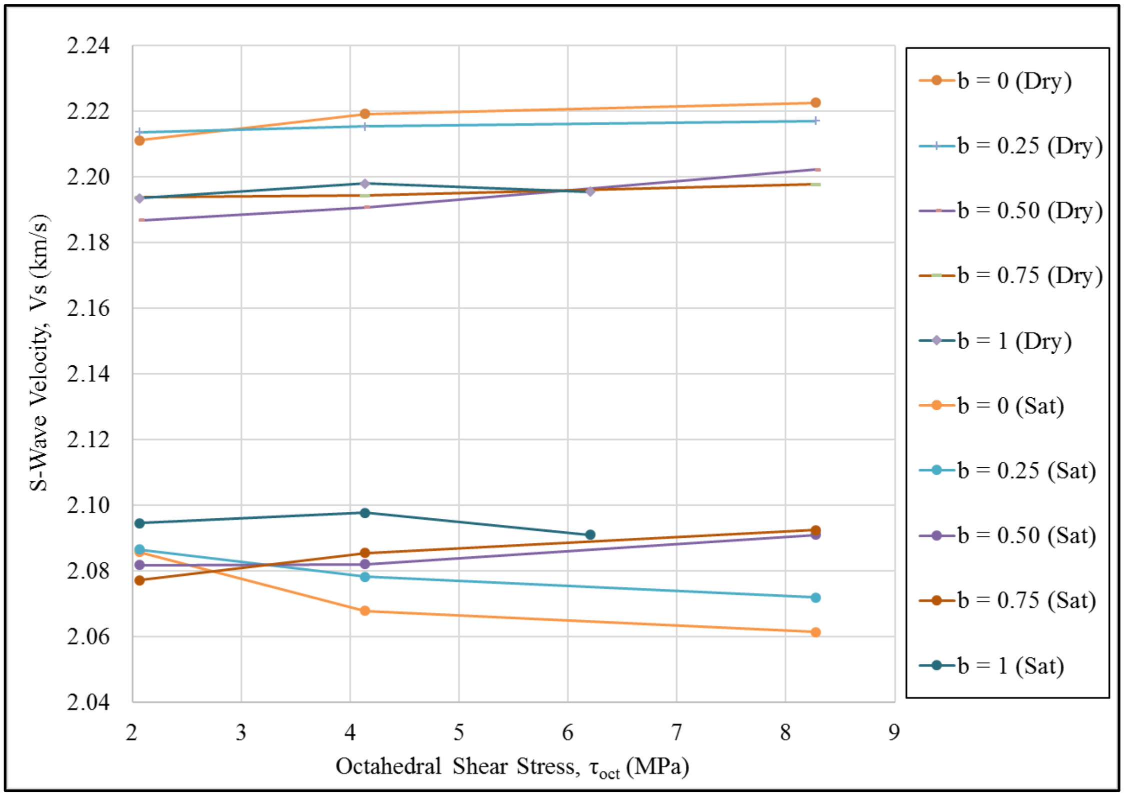

Figure 4.13: S-wave velocity variation with shear stress at constant normal stress of σ_{oct} = 20.7 MPa with different values of b for dry sample (Dry) and saturated sample (Sat).

However, it was also estimated that shear velocities show a higher degree of change associated with a respective porosity change than compressional velocities. The velocity ratio has been used increasingly often alongside compressional and shear velocities in identification of porosity and fluid type (Castagna et al. 1985). If the calculated shear wave velocity trends translate into the velocity ratios, the large difference between velocities at $b = 0$ and those at $b > 0$ can be attributed to a decrease in porosity, in addition supporting the notion of microfracture closures. The V_p/V_s ratios are illustrated in Figures 4.15 – 4.18. The velocity ratios in the saturated condition clearly exhibit a dependence on b, especially under 3.4 MPa normal stress, as seen in Figure 4.15. The trend in the saturated sample ratios is consistent and exhibits a reversely proportional relationship with the stress parameter, similar to P-wave velocity. This response is expected, owing to larger magnitudes of compressional wave velocity as compared to shear wave velocity. For higher normal stresses, the saturated S-wave velocity sensitivity to change in b is relatively constant, with smallest variation taking place under σ_{oct} = 6.9 MPa.

Dry case S-wave velocities showed a smaller dependence on the stress parameter, with data under 3.4 MPa normal stress showing little to no *b* effect. The remaining velocity ratios show a larger degree of consistency.

Through a comprehensive study of an array of different laboratory measurements and experimental data from the literature, Castagna et al. (1985) determined that clastic silicate sedimentary rocks exhibit an almost linear relationship between P- and S-wave velocities. The velocities were measured on samples under a variety of testing conditions, representing a general relationship between *Vp* and *Vs*.

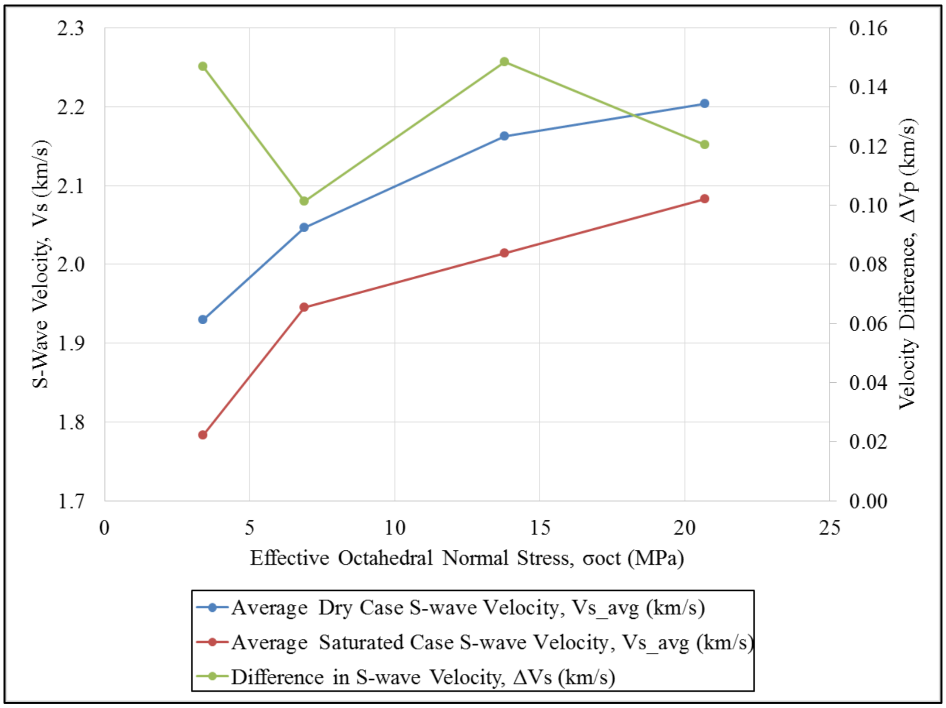

Figure 4.14: Difference between average S-wave velocities for dry and saturated samples.

Among other findings, Castagna et al. (1985) reported nearly constant velocity ratios for dry sandstones and decreased ratios at lower compressional velocity in saturated measurements. The laboratory wave velocity relationships for various sandstones are illustrated in Figure 4.19.

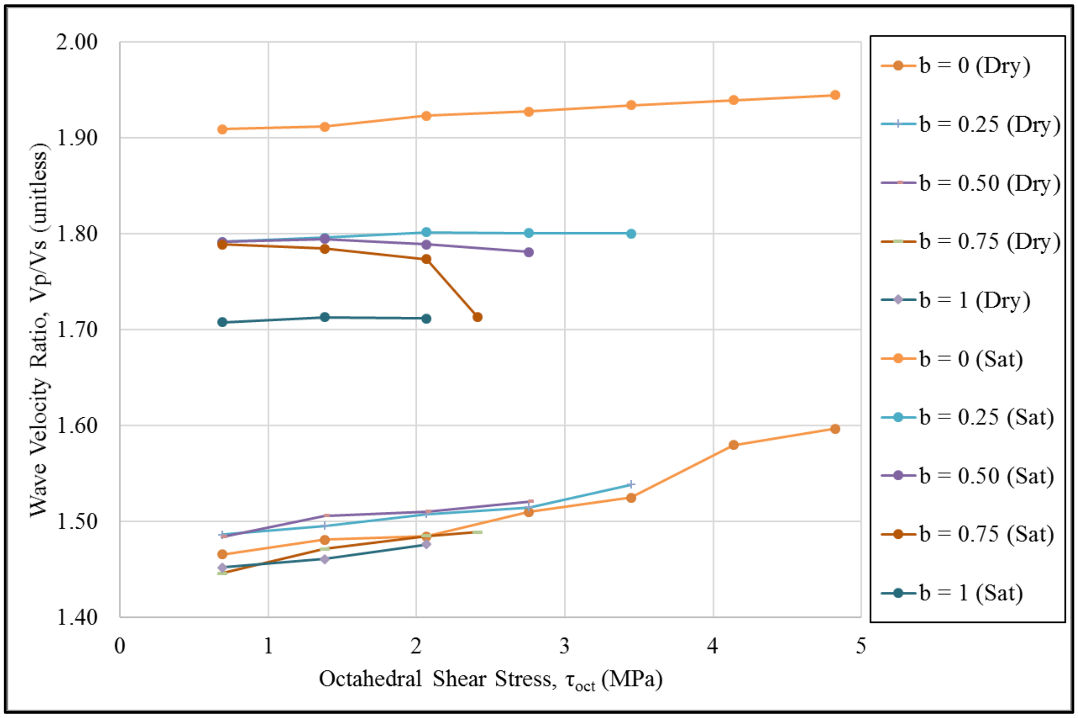

Figure 4.15: Ratios of compressional to shear velocities, Vp/Vs, at normal stress of σ_{oct} = 3.4 MPa.

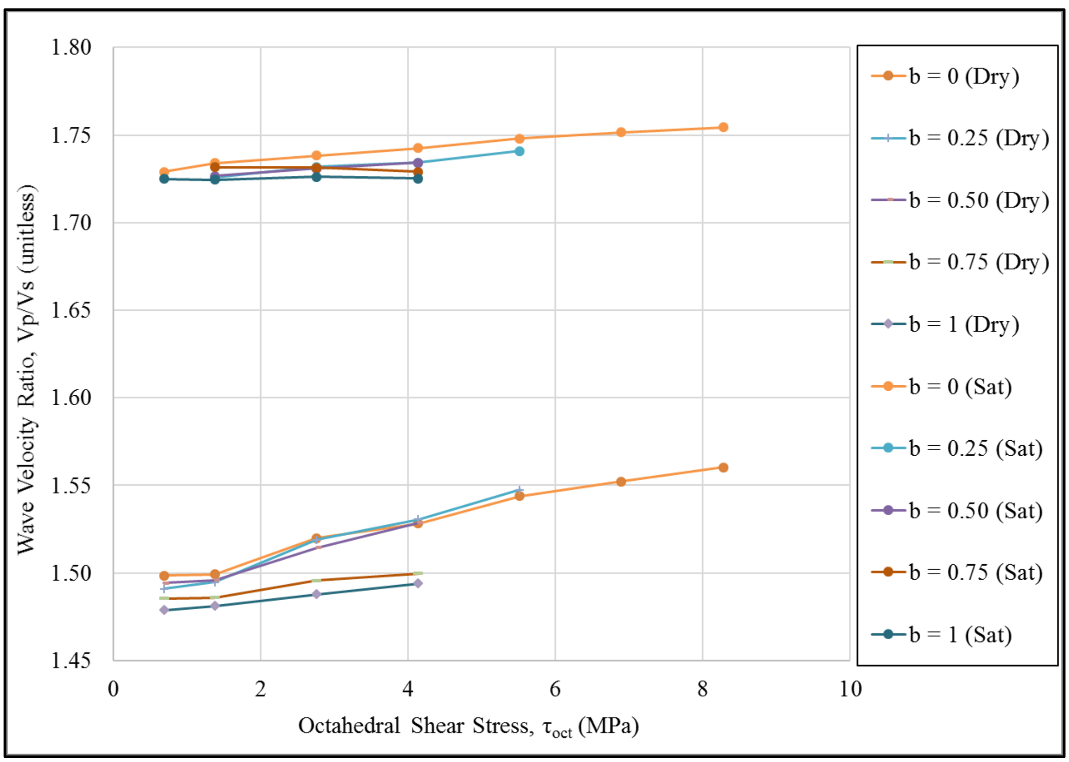

Figure 4.16: Ratios of compressional to shear velocities, Vp/Vs, at normal stress of σ_{oct} = 6.9 MPa.

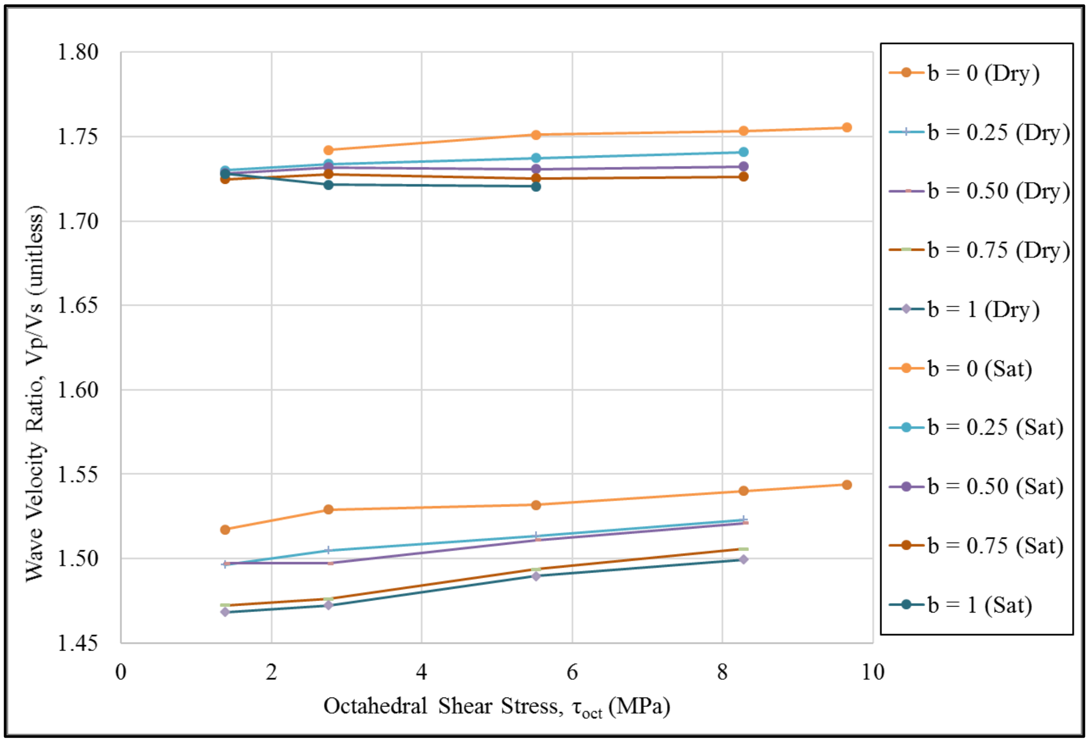

Figure 4.17: Ratios of compressional to shear velocities, Vp/Vs, at normal stress of σ_{oct} = 13.8 MPa.

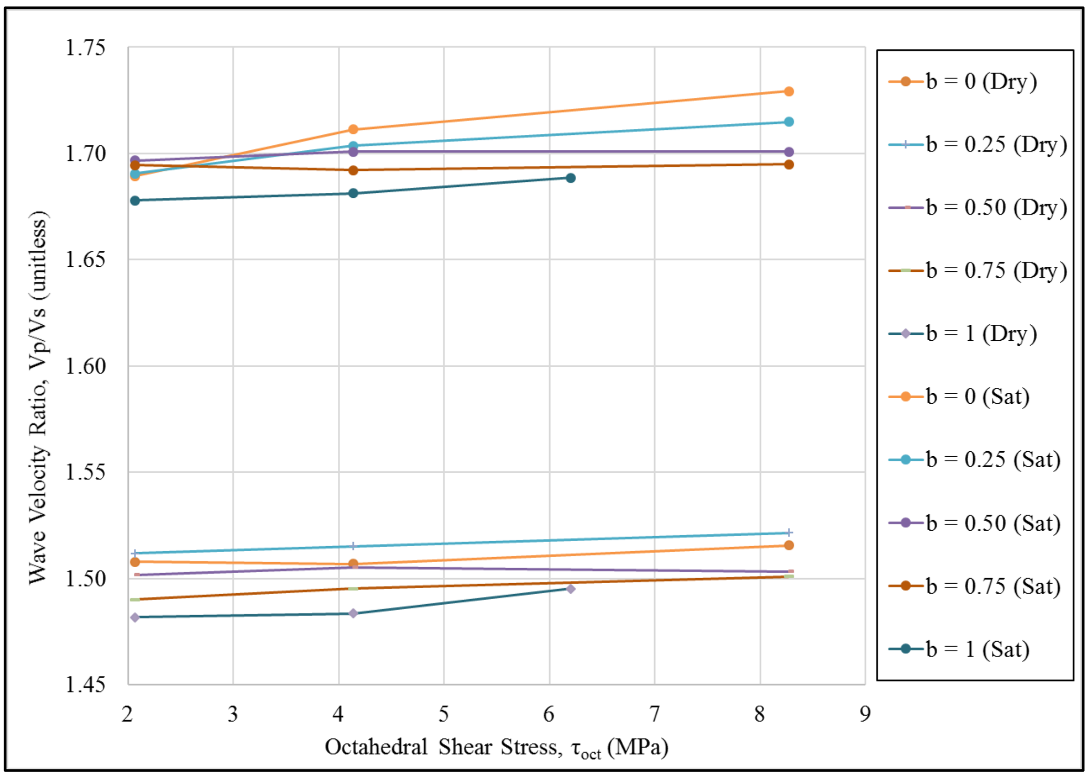

Figure 4.18: Ratios of compressional to shear velocities, Vp/Vs, normal stress of σ_{oct} = 20.7 MPa.

As shown in Figure 4.21, the data on Buff Berea for dry and water-saturated experiments exhibits very similar behavior. The dry velocity ratio is almost constant, with slight variations. The saturated velocity has a decreasing slope with increasing compressional velocity, as estimated by a linear trendline. The difference between the two figures exists in the magnitudes of compressional velocity, which are smaller in the case of Buff Berea. However, this discrepancy does not indicate a lack of correlation, because the effective stress magnitudes for Figure 4.20 data are not disclosed. It is possible that P-wave velocities were higher for that data as result of much higher magnitudes of stress. The difference in the shapes of the data is likely caused by the anisotropic state of stress generated in testing of Buff Berea.

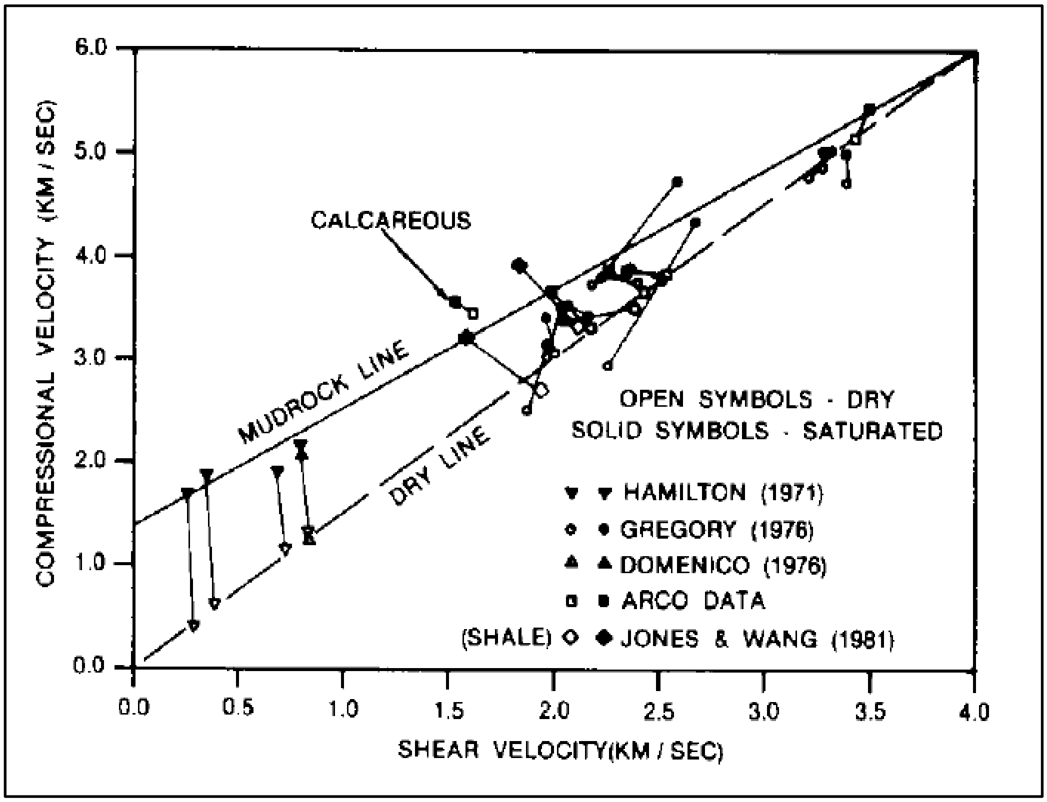

Figure 4.19: Wave velocity relationships for dry and saturated sandstones (Castagna et al. 1985).

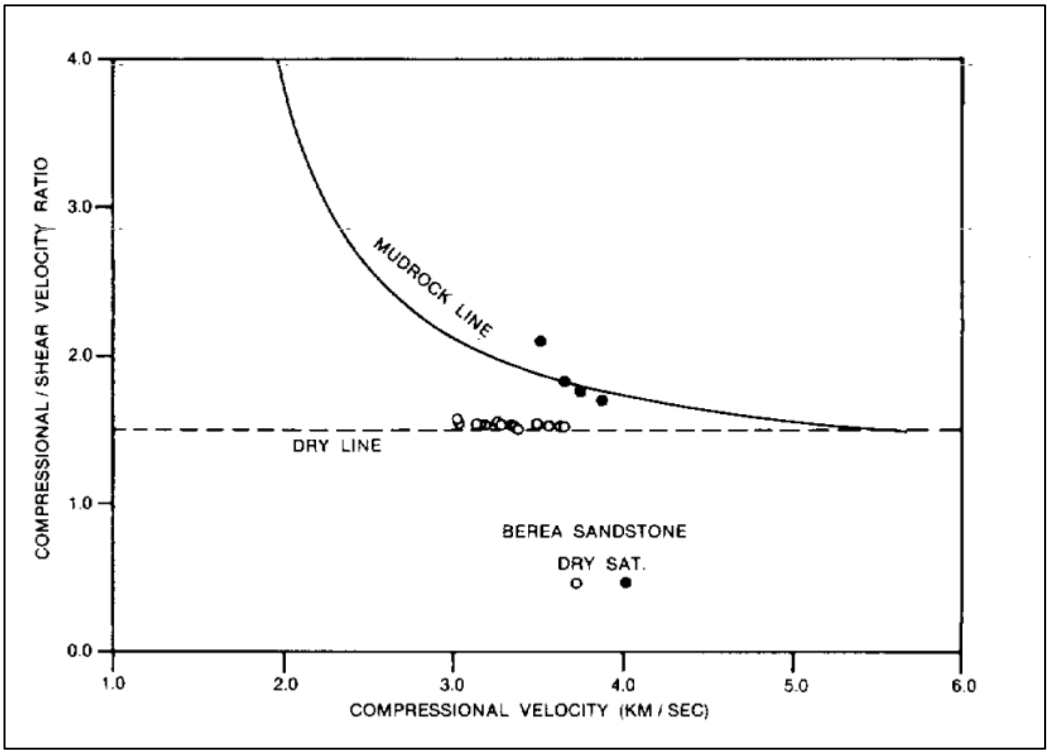

Figure 4.20: Wave velocity ratios for dry and water-saturated Berea sandstone under varying effective stresses (Castagna et al. 1985).

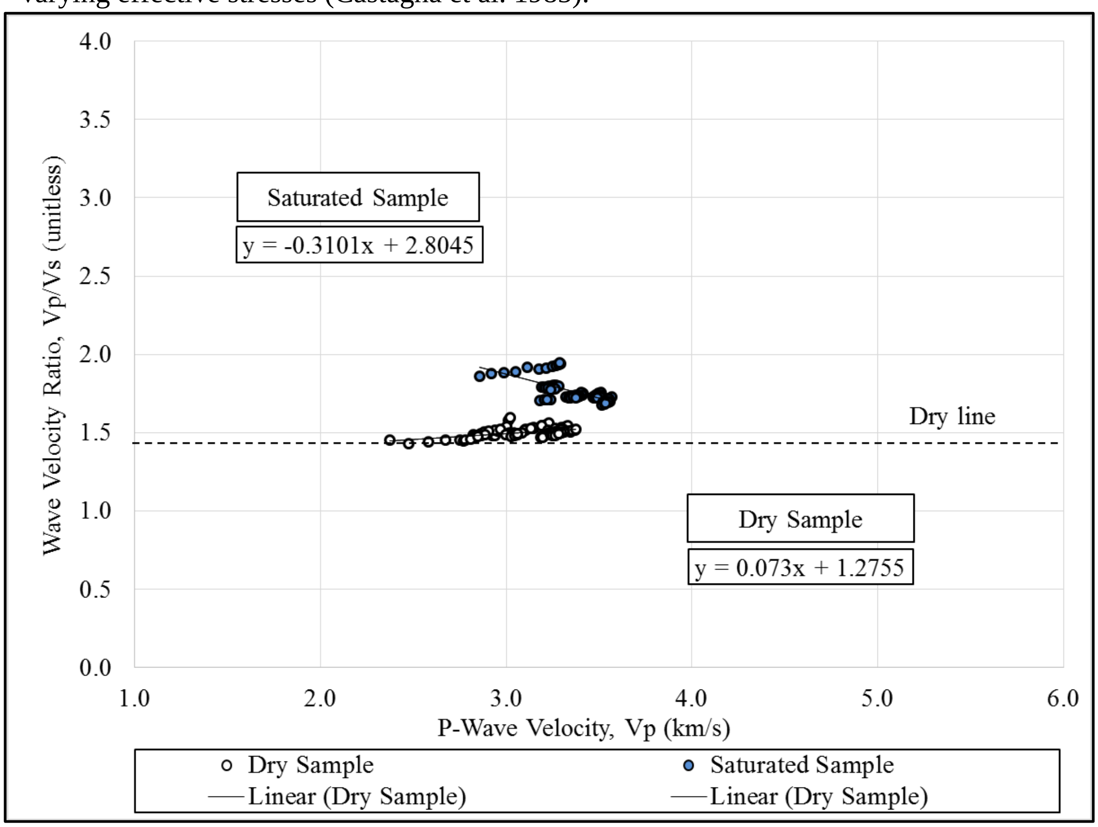

Figure 4.21: Wave velocity ratios for dry and water-saturated Buff Berea samples determined in this study.

Based on the similarity of wave velocities determined in this study to literature data shown above, the data of the study appears to be fitting for Berea sandstone. Moreover, the velocity ratios fall in the range of expected values for sandstones (1.5 – 1.7), as is expected in the conventional notion (Castagna et al. 1985). The full scale of relationship between compressional and shear waves is shown below (Figure 4.22), which is comparable to the literature data in Figure 4.19 above.

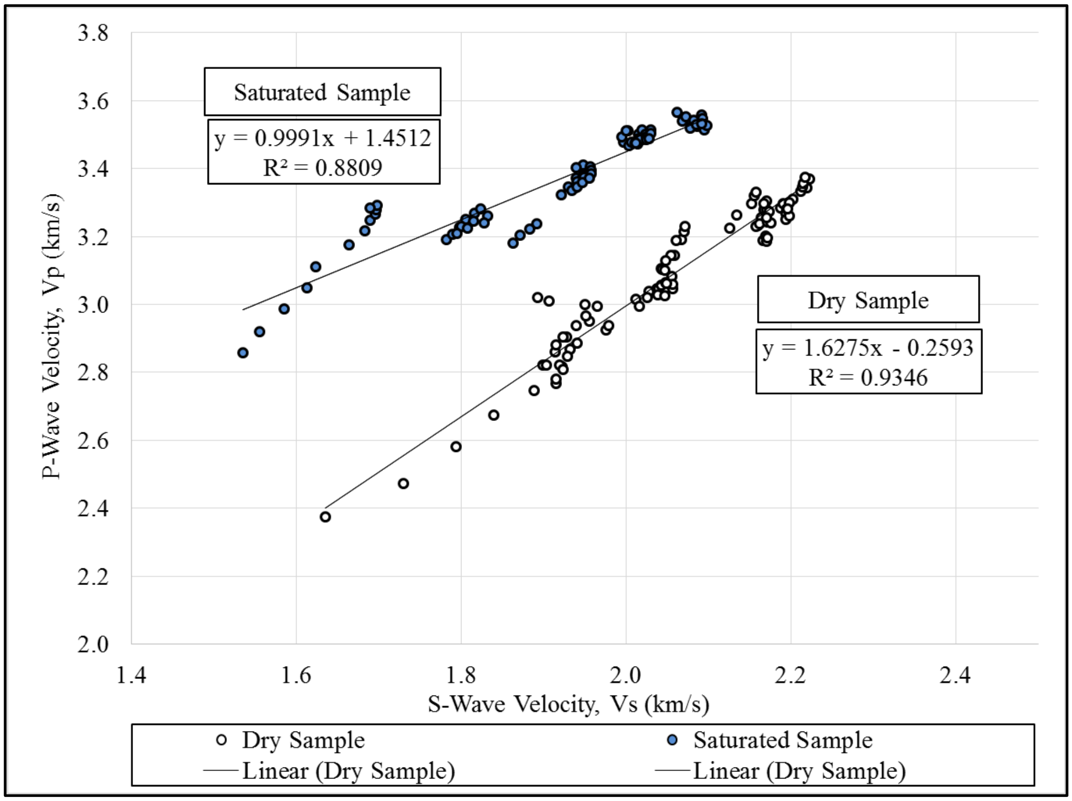

Figure 4.22: P- and S-wave velocity relationship in dry and saturated tests of Buff Berea.

As illustrated in the above figure, the average compressional to shear velocity ratio for the saturated scenario has a slope with a y-intercept different from that of the dry scenario, owing to a larger deviation from the trendline in the saturated sample data. As indicated by Figures 4.15-4.18, the saturated sample exhibited much higher velocity ratios than the dry sample. However, the saturated and dry velocity ratios react differently to stress changes. In spite of the deviation, the relationship between S- and P-waves is still nearly linear. The initial deviation for the saturated scenario is likely due to the high variation in S-wave velocities at normal stress of 3.4 MPa, as mentioned above.

Yin (1992) made wave velocity measurements in tensor form for Berea 200 sandstone (19.2% porosity and 2.14 g/cm^3 dry bulk density) under triaxial and polyaxial loading. The original tabulated data is presented in graphical form in terms of principal stresses (Figure 4.23).

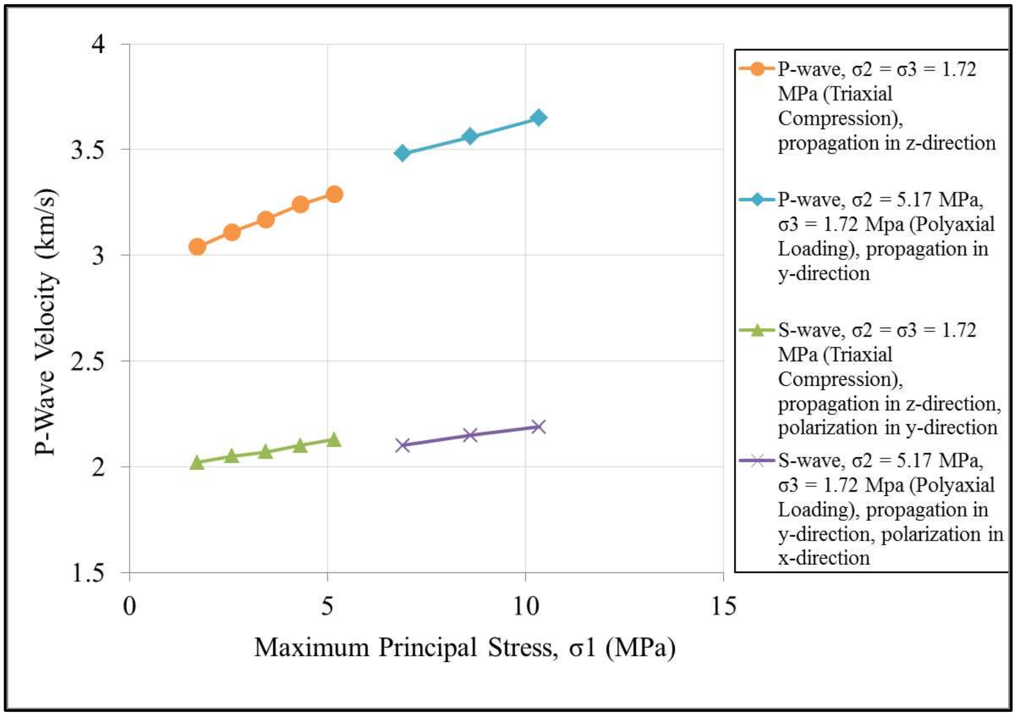

Figure 4.23: Wave velocity variation across triaxial and polyaxial loading for Berea 200 sandstone (dry). Wave propagation is along the direction of maximum principal stress. This is the graphical representation of Figure 4.24 with data points for maximum principal stress in directions of y- and z-axis (Yin 1992).

The data that was used to create the figure above is shown below (Figure 4.25). Because the direction of maximum principal stress changes from z-axis to y-axis, the corresponding velocities were also changed for P- and S-waves. The schematic of the polyaxial loading assembly used to measure wave propagation in the study is illustrated below (Figure 4.24). The loading was performed by manual turning of loading bolts of the polyaxial frame. As indicated by the schematic, the sample shape is different from cylindrical and the faces of the sample are incompletely covered by the rigid platens. This configuration, discussed in Chapter 2 as a Type I true triaxial loading device, incorporates partial loading due to the corner effect, as well as friction effects due to rigidity of the platens. Based on the observation of velocity response in the figure above, P-wave velocity increases under triaxial compression with higher maximum principal stress.

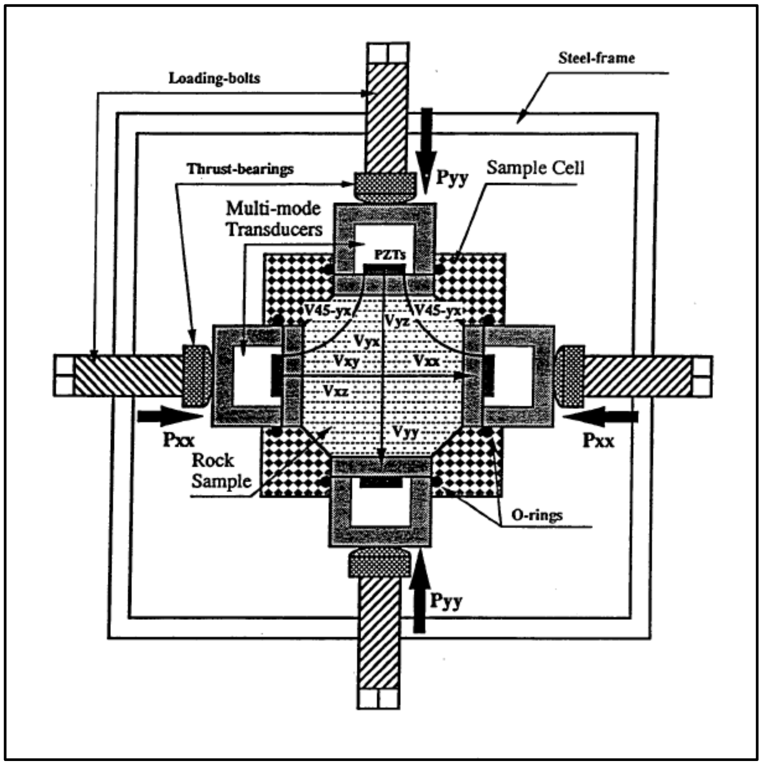

Figure 4.24: Schematic of loading and sample shape for polyaxial loading system (Yin 1992).

Berea 200 Sandstone (Triaxial Loading, Pxx=Pyy=17.2bar)

Pzz	Vzz	Vzx	Vzy	Vyy	Vyx	Vyz	Vxx	Vxy	Vxz	V_{45-zx}	V_{45-zy}	V_{45-xy}
(bar)	Velocity(KM/Second)											
17.2	3.04	1.97	2.02	3.21	2.03	2.08	3.20	2.02	2.08	3.17	3.16	3.20
25.8	3.11	2.01	2.05	3.22	2.03	2.09	3.20	2.03	2.10	3.25	3.18	3.21
34.5	3.17	2.03	2.07	3.22	2.03	2.11	3.21	2.03	2.12	3.26	3.25	3.22
43.1	3.24	2.06	2.10	3.23	2.04	2.13	3.22	2.03	2.14	3.29	3.28	3.22
51.7	3.29	2.08	2.13	3.22	2.05	2.14	3.23	2.03	2.15	3.34	3.32	3.25

Berea 200 Sandstone (Polyaxial Loading, Pxx=17.2bar, Pzz=51.7bar)

Pyy	Vzz	Vzx	Vzy	Vyy	Vyx	Vyz	Vxx	Vxy	Vxz	V_{45-zx}	V_{45-zy}	V_{45-xy}
(bar)	Velocity(KM/Second)											
17.2	3.29	2.08	2.13	3.22	2.05	2.14	3.23	2.03	2.15	3.34	3.32	3.25
34.5	3.29	2.09	2.14	3.33	2.07	2.18	3.21	2.06	2.15	3.32	3.38	3.31
51.7	3.29	2.09	2.16	3.39	2.09	2.20	3.21	2.08	2.16	3.26	3.43	3.35
69.0	3.29	2.10	2.18	3.48	2.13	2.23	3.20	2.09	2.16	3.28	3.45	3.37
86.2	3.31	2.10	2.20	3.56	2.15	2.26	3.20	2.12	2.17	3.25	3.47	3.40
103.5	3.31	2.11	2.23	3.65	2.19	2.29	3.20	2.15	2.17	3.27	3.51	3.42

Figure 4.25: Velocity variation with triaxial and polyaxial loading of Berea 200 sandstone (Yin 1992).

Essentially, the velocity increase under triaxial compression shows the same behavior as the wave velocities of dry Buff Berea when $b = 0$. However, the polyaxial velocity trend corresponds to decreasing b with increasing maximum principal stress (from $b = 0.67$ to $b = 0.40$). P-wave velocity increases with decreasing b, which parallels the compressional wave behavior in this study. S-wave velocity exhibits a correlating trend as well. It should be noted, however, that this data involves a larger error due to issues related to Type I devices and manual generation of loading. The trends in velocity response show the same behavior as with the Buff Berea tests. Yin stipulated that soft rocks, such as Berea sandstone, exhibit stress-induced anisotropy of wave velocity and attenuation due to microfracture closure along the direction of increasing stress, and that intrinsic velocity anisotropy is a result of preferential grain and microfracture orientations, as well as interbedded clay layers.

Since aspect ratios of closing microfractures are oriented normally to the direction of increasing stress, under varying anisotropic stress conditions microfracture closures depend on the relative magnitudes of all three principal stresses, indicating that the stress state of the sample influences anisotropy of deformation and wave velocity.

4.3 Stress-Induced Permeability Anisotropy

All of the permeability measurements were made in the axial direction (direction of maximum principal stress), with fluid flow upwards from the bottom of the sample. The Darcy's flow equation was used, based on the relatively high permeability of sandstone. Axial strain data was incorporated into the calculations. Permeability was measured at both hydrostatic and highly anisotropic conditions, for each of the four levels of normal stress and for each b value. In all anisotropic stress conditions, only the measurements under maximum shear stress were taken. The change in permeability under the tested stress conditions is illustrated in Figure 4.26. First two measurements were made under effective hydrostatic stresses of 1.4 and 3.4 MPa. The stress loops seen on the graph indicate all of permeability measurements for each cluster of constant normal stresses. At hydrostatic stresses of 6.9 and 13.8 MPa (between the stress cycles), permeability decreases with a large corresponding axial strain. Permeability change under hydrostatic stresses follows a certain curve, with a large initial drop in magnitude at low stresses and smaller subsequent reduction.

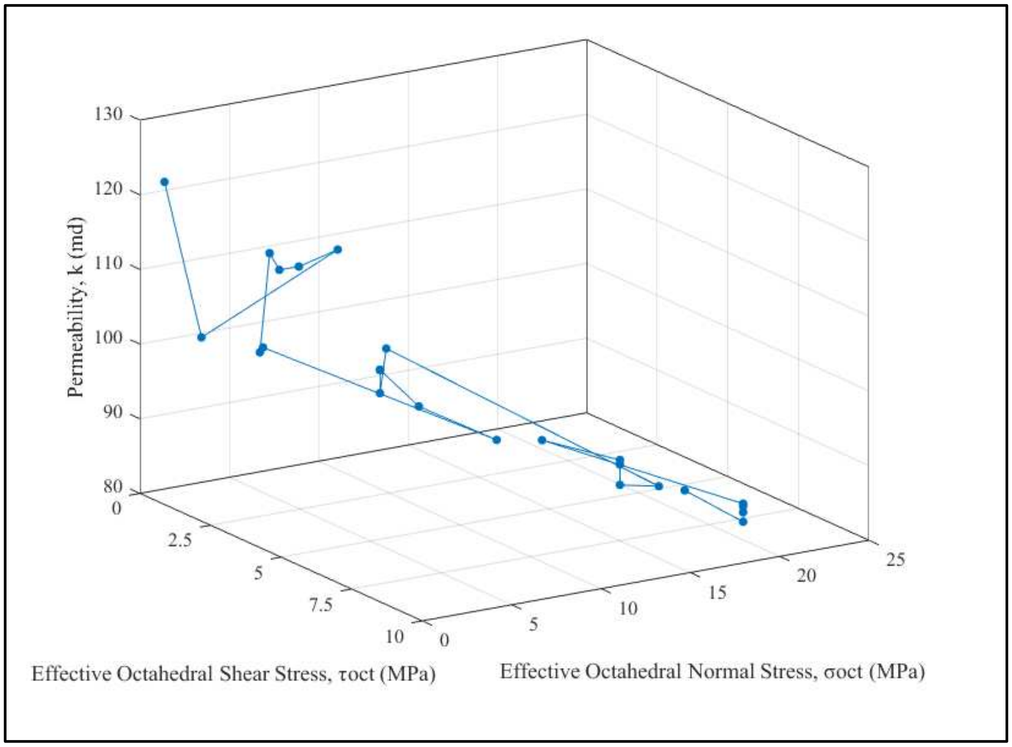

Figure 4.26: Effects of normal and shear stresses on permeability.

The response to both shear and normal stresses is clearly visible by the orientation of the curve. A more detailed permeability response to the applied stresses can be seen against axial strain (Figure 4.27). Each loop illustrated in the figure represents maximum shear stresses at increasing b. It is noticeable that permeability response to the stress parameter is not consistent across different normal stresses. In addition, shear stress in the sample is seen to increase permeability for all normal stresses. As b increases, however, this effect takes on different forms. For instance, at $b = 0$, maximum shear stress first results in an approximately 20 md increase in permeability at 3.4 MPa, but as b rises to 1, permeability drops 5 md. The effect of b is not consistent throughout the measurements, causing some increase of k at higher b values under larger normal stresses. The normal stress increase, as mentioned above, causes a smaller respective change in permeability, which can be aptly illustrated by plotting permeability versus hydrostatic stress (Figure 4.28).

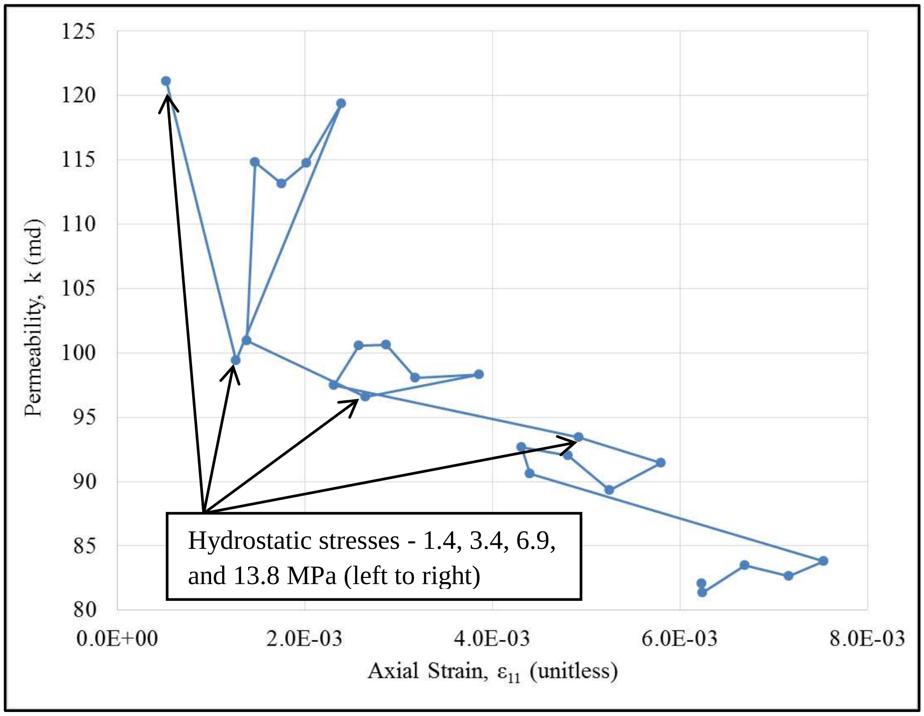

Figure 4.27: Permeability response to stress with corresponding axial strain.

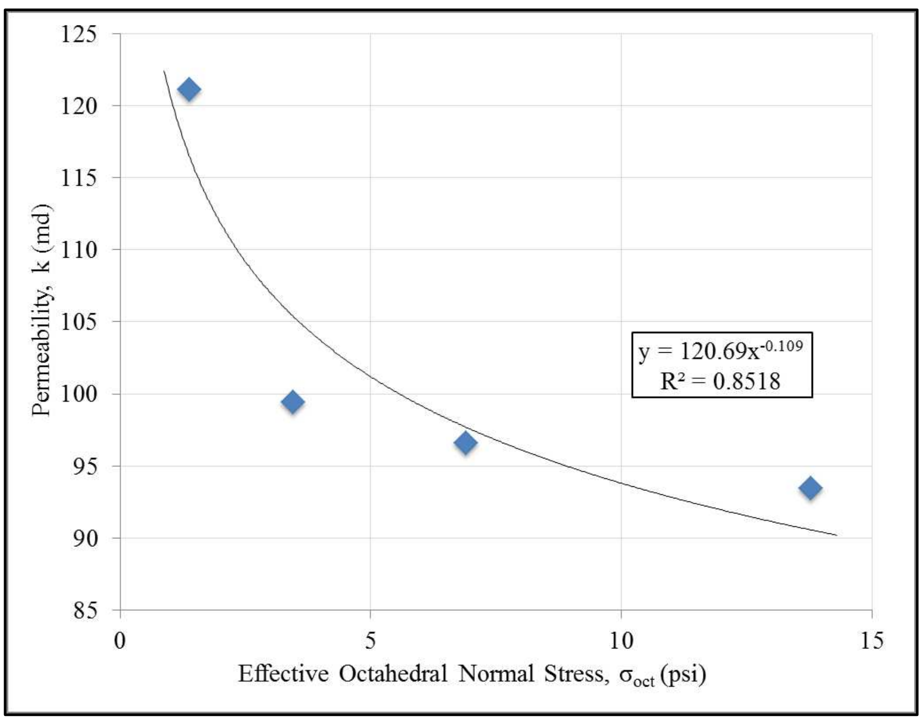

Figure 4.28: Permeability reduction with increasing hydrostatic stress.

The hydrostatic stress effect on permeability can be approximately captured by fitting the data points with a power-trendline. Figure 4.29 shows the b-sensitivity of permeability data at four different normal stresses. A trend of decreasing permeability with increasing b is discerned at $\sigma_{oct} = 3.4$ MPa.

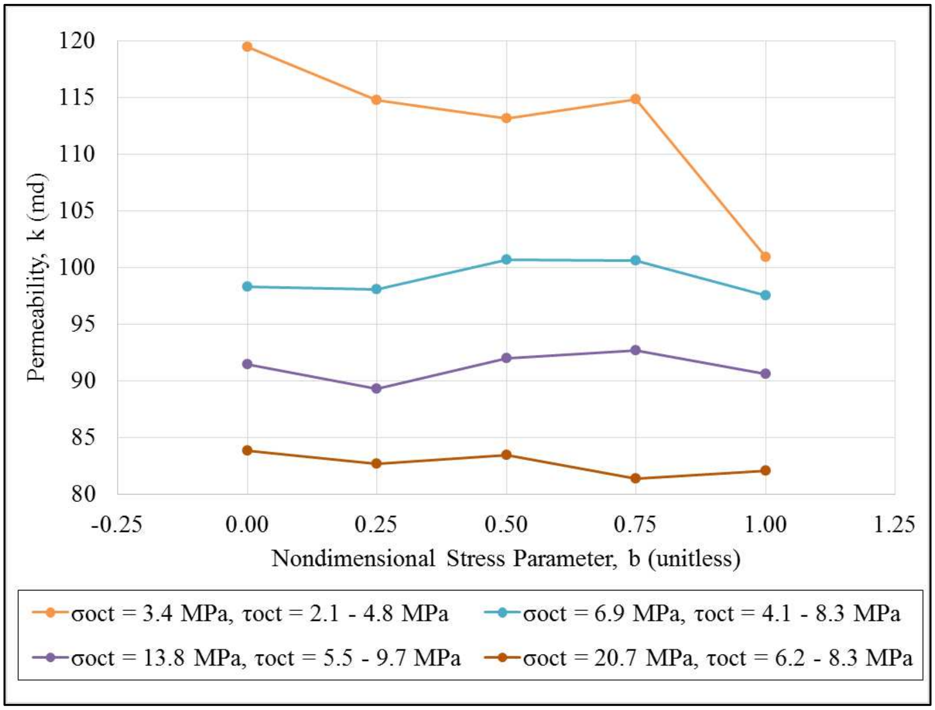

Figure 4.29: Permeability sensitivity to nondimensional stress parameter, b, at a variety of normal and shear stresses.

However, there seems to be a small effect of b on permeability at higher normal stresses, as demonstrated by the relatively constant permeability values with increasing b. It should be noted, though, that small fluctuations in permeability as shown in Figure 4.27 indicate that stress parameter effect is present and does influence permeability to a certain extent.

Since axial permeability shows dependence on b, aside from normal and shear stresses, it is necessary to observe the variation of permeability with shear wave velocity, a property that exhibits strong dependence on σ_2 effects. The two variables are shown in Figure 4.30. There appears to be a somewhat linear relationship between saturated S-wave velocity and axial permeability. Since permeability in this study is measured under both hydrostatic and anisotropic conditions, the large deviations from the observed trend can be attributed to hydrostatic stress effects. When all principal stresses are equal and continuously increased, closures tend to occur in all microfracture orientations, in addition to compaction of pore throats and channels. Naturally, shear wave velocity and permeability react differently to a decrease in pore volume and fluid pathways. Shear velocity will increase due to propagation through a denser medium, whereas permeability will decrease due to narrowing of fluid channels. Therefore, the outlier data in Figure 4.30 should not be assumed as an indication of poor correlation between the two properties.

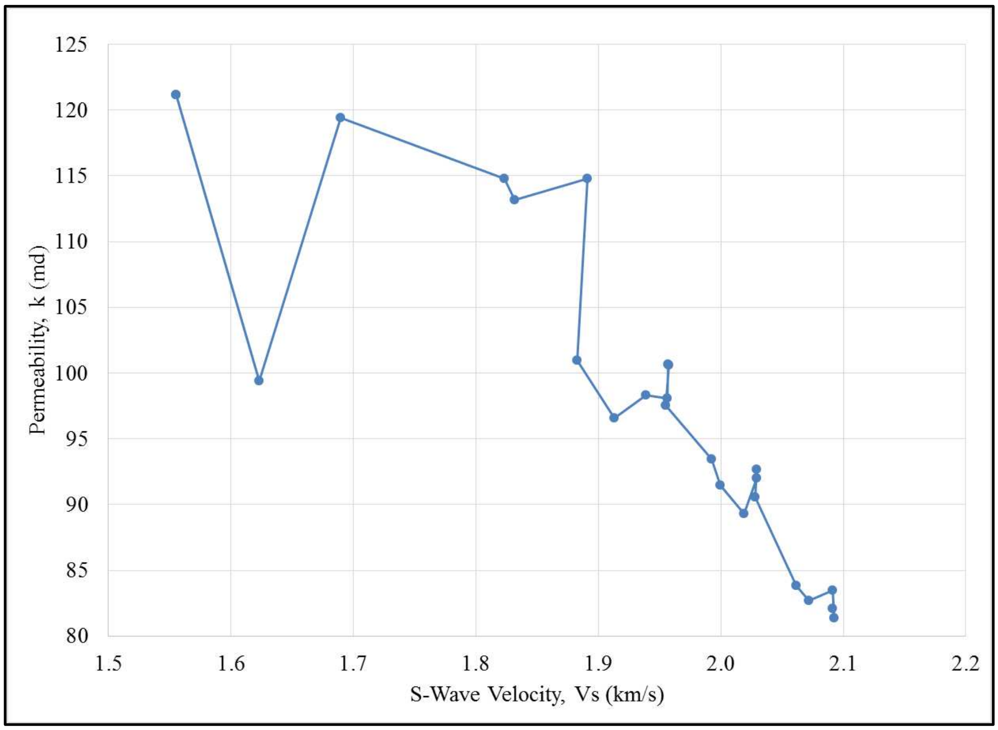

Figure 4.30: Permeability relationship with shear wave velocity.

As b increases with constant normal stress, the relative magnitude of σ_2 grows, resulting in closures of microfractures oriented normally to the direction of intermediate principal stress. On the one hand, as determined before, shear velocity will increase with b due to shear wave polarization in the plane parallel to σ_2. Permeability, on the other hand, depends on structure of open channels in the direction of flow, and is therefore influenced by all three principal stresses. While this figure illustrates a certain trend, velocities of S-waves polarized at 90 degrees to σ_2 could offer more information in terms of microfracture closures or openings in the direction of σ_3, possibly improving the understanding of their effects on permeability.

As discussed in Chapter 2, Bruno (1993) performed simulation studies as well as laboratory compressional testing of sandstones to determine stress-induced permeability anisotropy. The findings, correlated between simulation results and experimental data, concluded that permeability decreases under loading perpendicular to direction of flow, and increases under loading in direction parallel to flow. Microfracture formation and coalescence in the non-elastic deformation stage promoted permeability increase, even though initial elastic loading reduced permeability. Both the simulated models and real cores were tested under triaxial loading conditions, as well as uniaxial loading for simulation. The theoretical basis of the simulated cases constituted that pore space flow occurs through cementation bonds between grains and that deformation of those bonds affects flow.

The permeability results for water-saturated Buff Berea sample indicate strong correlations with these findings. First of all, there is a clear relationship between the direction of loading and permeability alteration. Permeability reduction with increasing b, signifying larger loading in direction perpendicular to flow, is quite substantial at low normal stress. The opposite behavior is observed with high shear stresses when $b = 0$, indicating flow-parallel loading that increases permeability. Secondly, the general trend throughout the extent of testing is the steady reduction in permeability, which is reported to take precedence before the onset of microfracture formation and coalescence that will ultimately reverse permeability changes. Even though the complete relationship between permeability and stress is not explored in this study to observe the abrupt increase in permeability under larger loading magnitudes nearing maximum stress, permeability trends under a variety of general states of stress are valuable indicators of stress effect.

The relationship between permeability and the state and magnitude of stress observed in this study is in clear accordance with literature data and moreover, illustrates the effect of stress parameter b. The parameter b exhibits a reversely proportional effect on permeability at low normal stresses, incorporating closures of microfractures and narrowing of flow channels in the direction of flow. At higher stresses, the effect of b becomes more negligible, which is likely associated with a lower degree of microfracture closures in the sample and sample stiffening.

4.4 Static and Dynamic Elastic Moduli

The use of elastic moduli is a significant feature of deformation analysis for uniaxial, hydrostatic, and conventional triaxial testing of rocks. However, due to an increased complexity of true triaxial stress-induced deformation with the addition of independent intermediate principal stress, it should be noted that the use of only two elastic moduli to study such deformation is insufficient due to the additional anisotropy introduced. The minimum number of elastic constants to describe the smallest degree of anisotropic behavior is five for transversely isotropic rocks, a group to which Berea sandstone belongs. However, some conclusions about deformation can be easily made even with two elastic moduli.

Dynamic moduli were calculated from the wave velocity data in the form of Poisson's ratios and Young's moduli. Static Young's moduli were calculated in the form of a secant modulus – the slope of the line from zero shear stress at any stress-strain curve to the designated shear stress. Due to the lack of static radial deformation data, radial strain was estimated from dynamic Poisson's ratios by assuming no variation between static and dynamic Poisson's ratios:

$$\varepsilon_{22} = \nu * \varepsilon_{11} \tag{4.1}$$

where ε_{22} = strain in σ_1 direction; ν = Poisson's ratio; ε_{11}= strain in σ_2 direction.

The dynamic Poisson's ratios are shown in Figures 4.31 - 4.34. The Poisson's ratios closely resemble previously discussed compressional to shear wave velocity ratios (Figures 4.15 – 4.18). Dynamic Poisson's ratios for the saturated scenario exhibit an inversely proportional relationship with b, indicating that under lower relative magnitudes of σ_2 radial expansion in the direction of σ_2 increases. Similarly to Vp/Vs, ν_D is most sensitive to changes in b under low normal stress (3.4 MPa). Shear stress dependency of saturated Poisson's ratios is negligible, indicated by a nearly zero slope of the ratios. Conversely, dry

Poisson's ratios exhibit ductile behavior, increasing under higher shear stress magnitudes. However, this behavior ceases at normal stress of 20.7 MPa. Dry ratios also indicate sensitivity to the stress parameter.

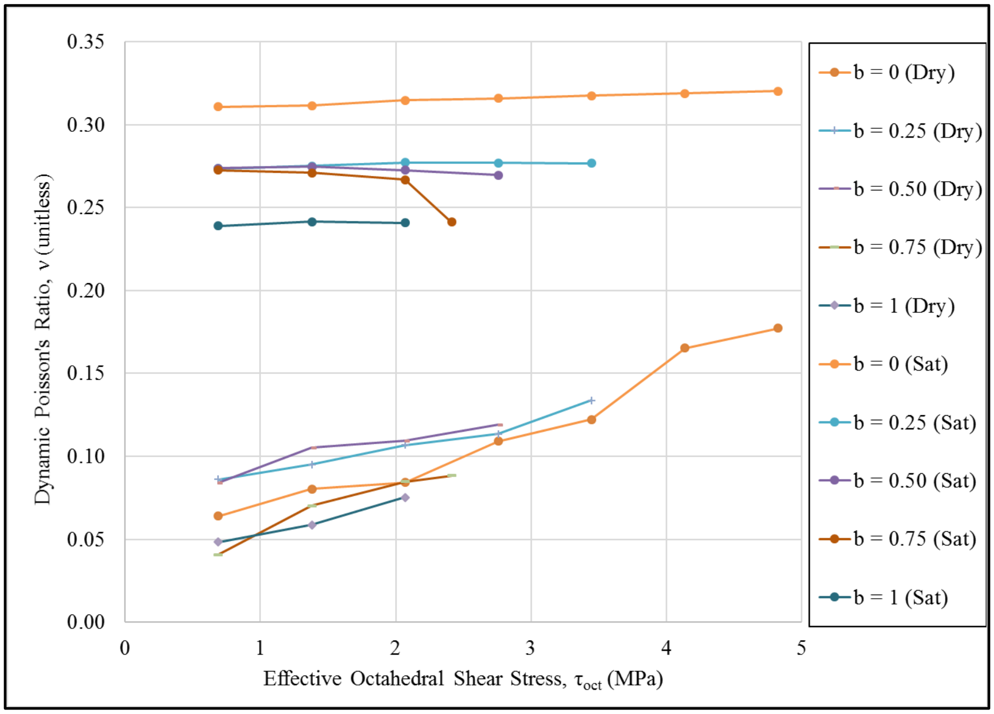

Figure 4.31: Dynamic Poisson's ratios at $\sigma_{oct} = 3.4$ MPa.

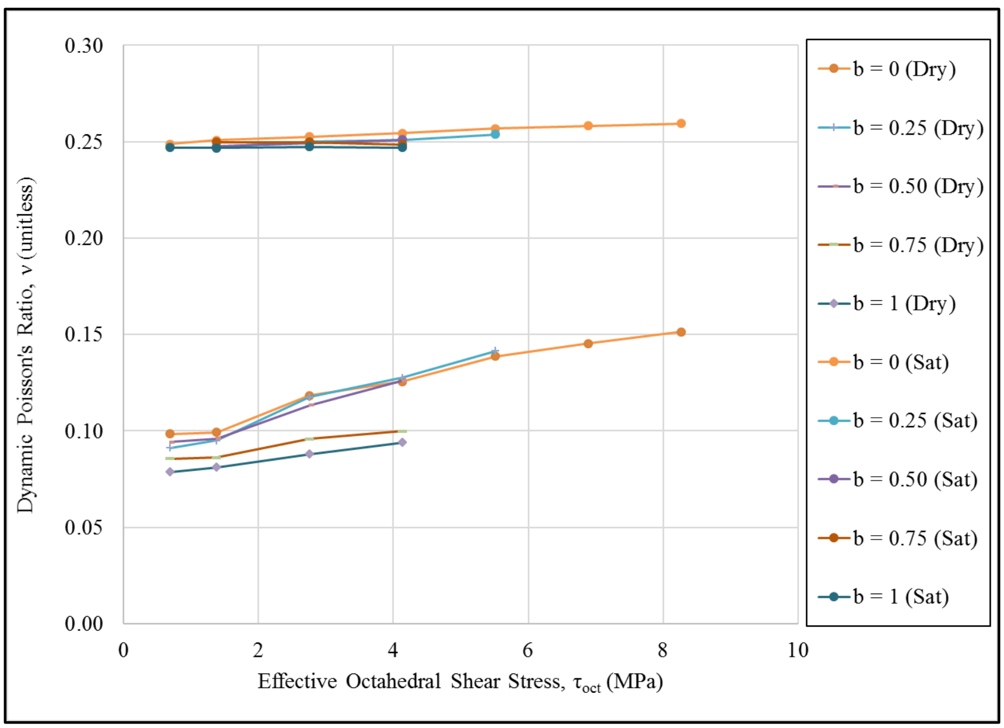

Figure 4.32: Dynamic Poisson's ratios at $\sigma_{oct} = 6.9$ MPa.

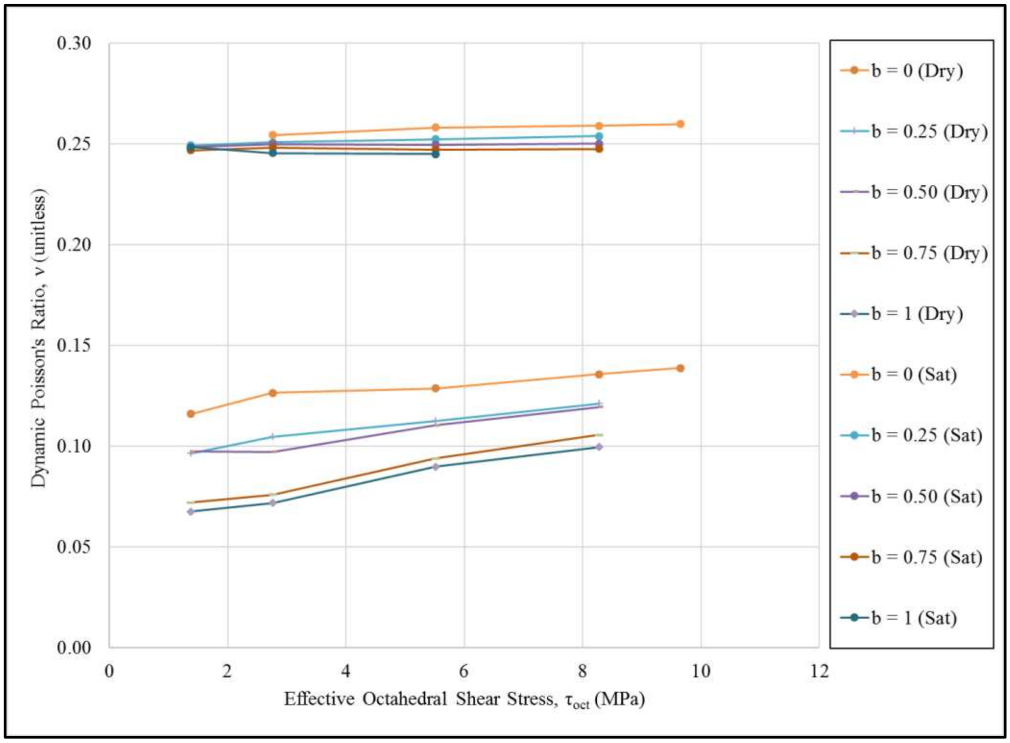

Figure 4.33: Dynamic Poisson's ratios at $\sigma_{oct} = 13.8$ MPa.

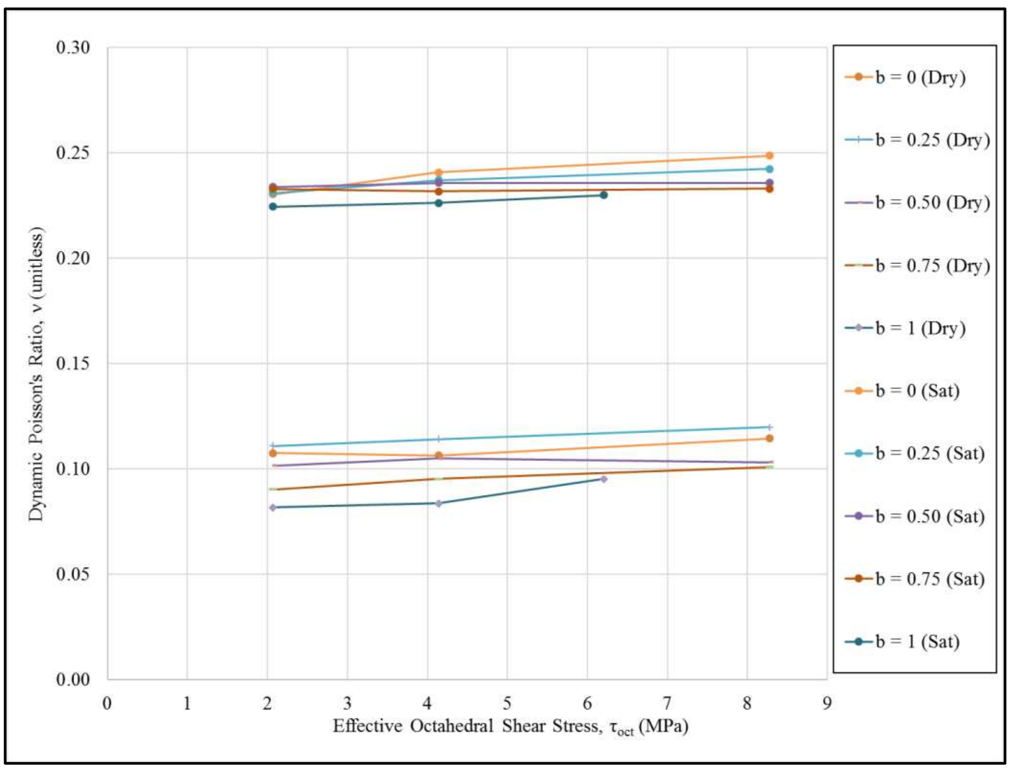

Figure 4.34: Dynamic Poisson's ratios at $\sigma_{oct} = 20.7$ MPa.

There is more deviation from the anticipated trend in the dry stress scenario. Young's moduli determined through wave velocity are contrasted with static Young's moduli (Figures 4.35 – 4.42).

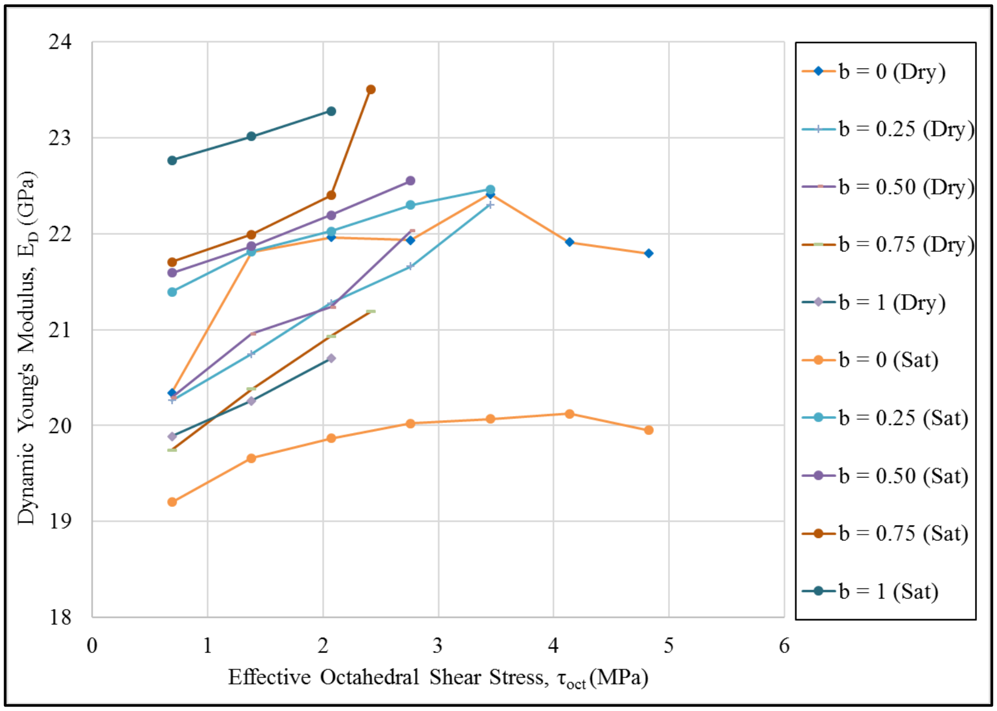

Figure 4.35: Dynamic Young's Moduli at σ_{oct} = 3.4 MPa.

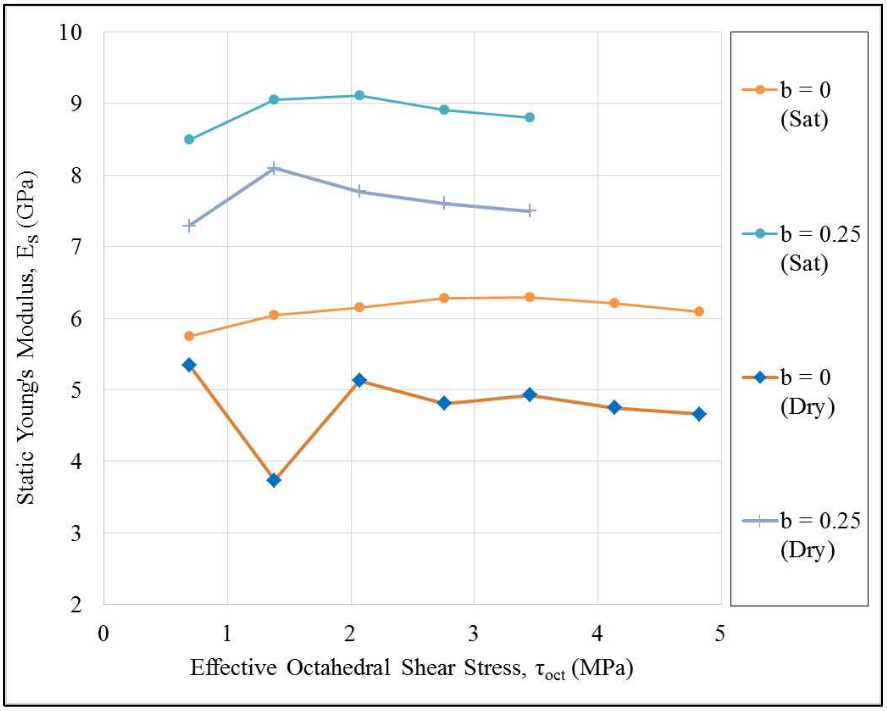

Figure 4.36: Static Young's Moduli at σ_{oct} = 3.4 MPa.

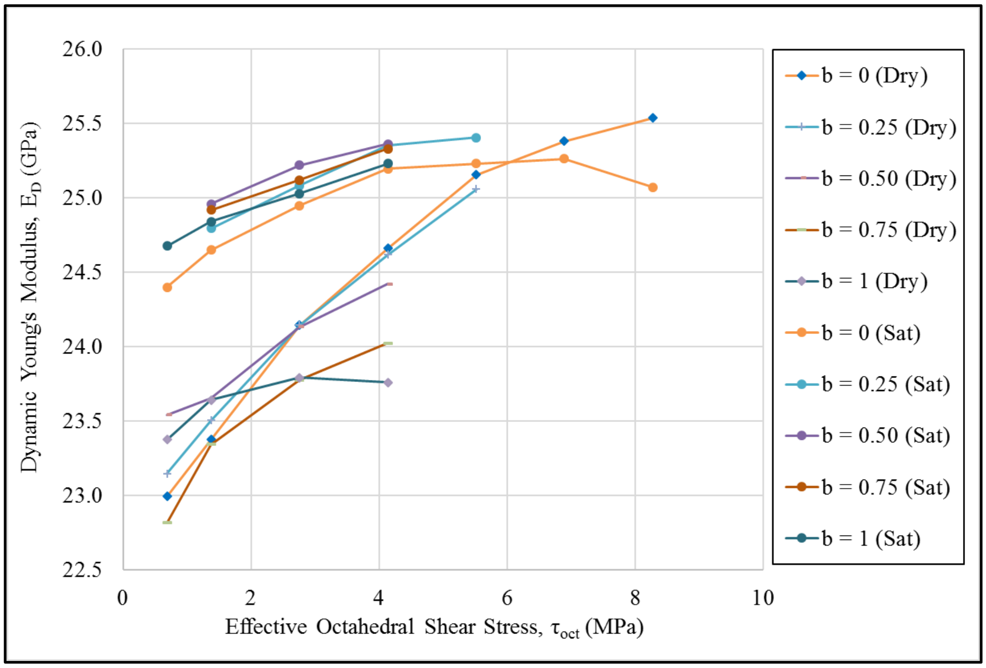

Figure 4.37: Dynamic Young's Moduli at $\sigma_{oct} = 6.9$ MPa.

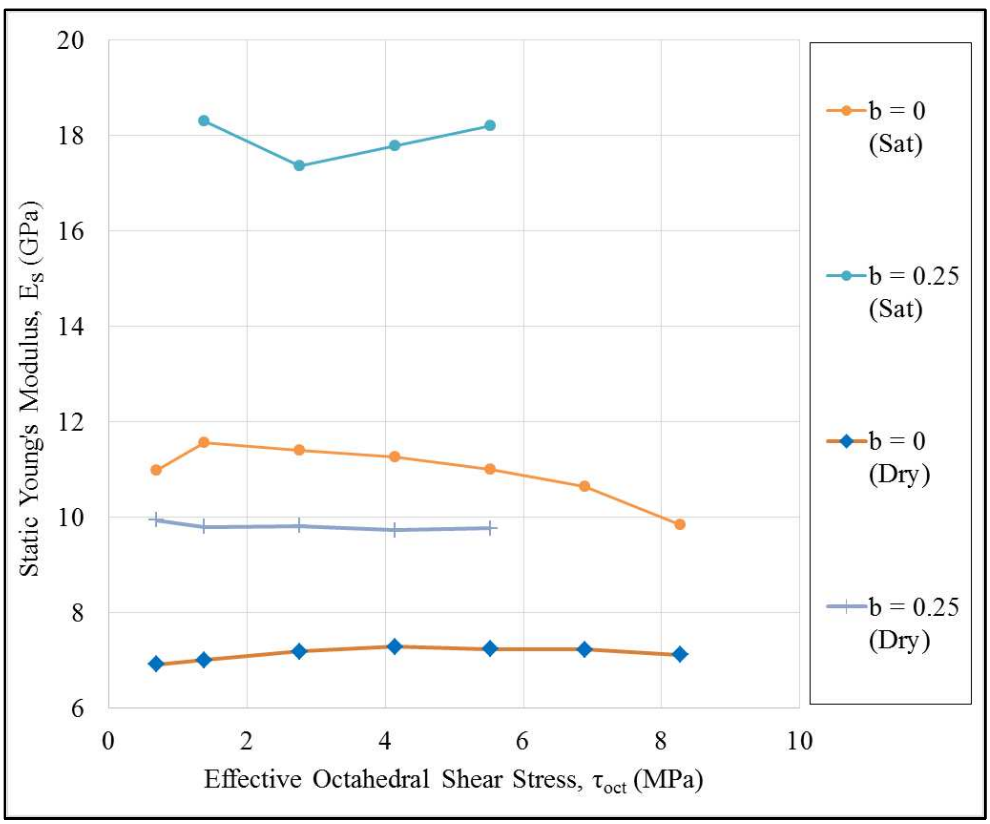

Figure 4.38: Static Young's Moduli at $\sigma_{oct} = 6.9$ MPa.

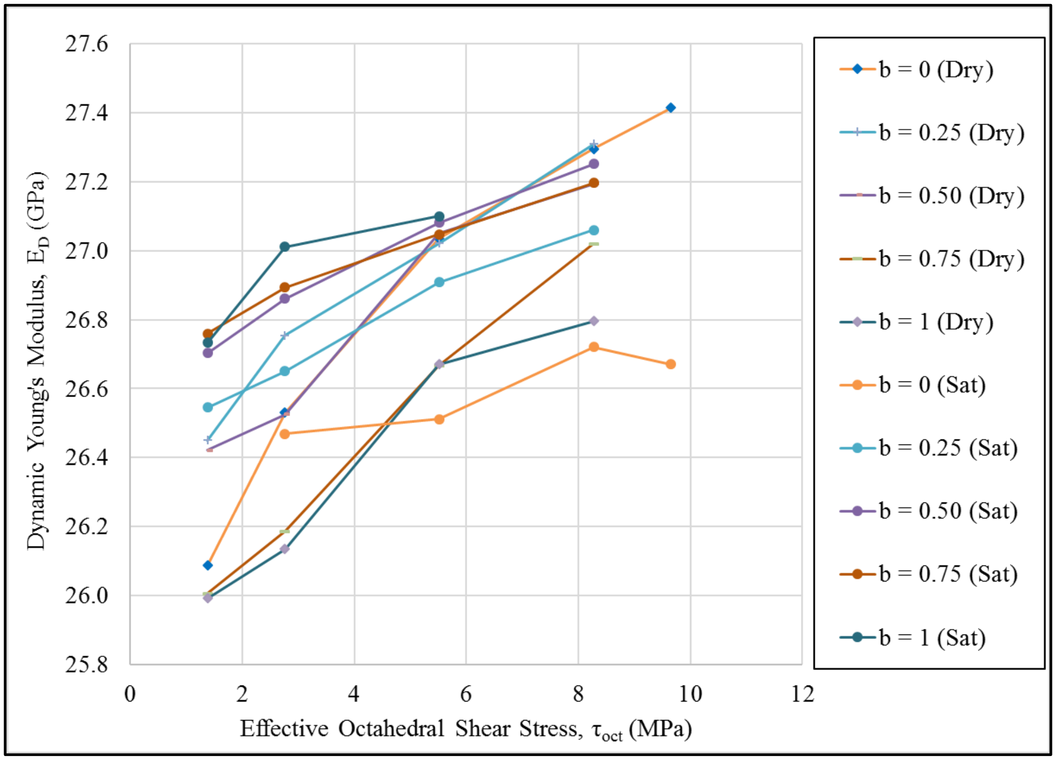

Figure 4.39: Dynamic Young's Moduli at $\sigma_{oct} = 13.8$ MPa.

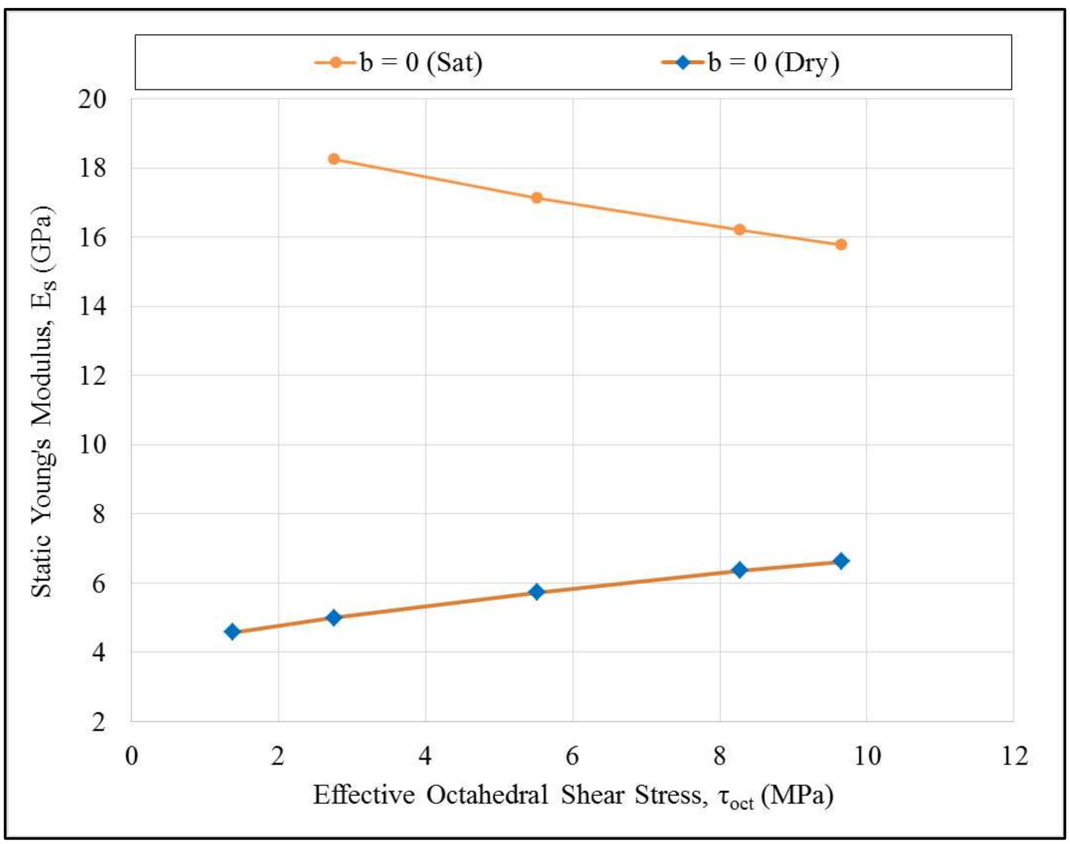

Figure 4.40: Static Young's Moduli at $\sigma_{oct} = 13.8$ MPa.

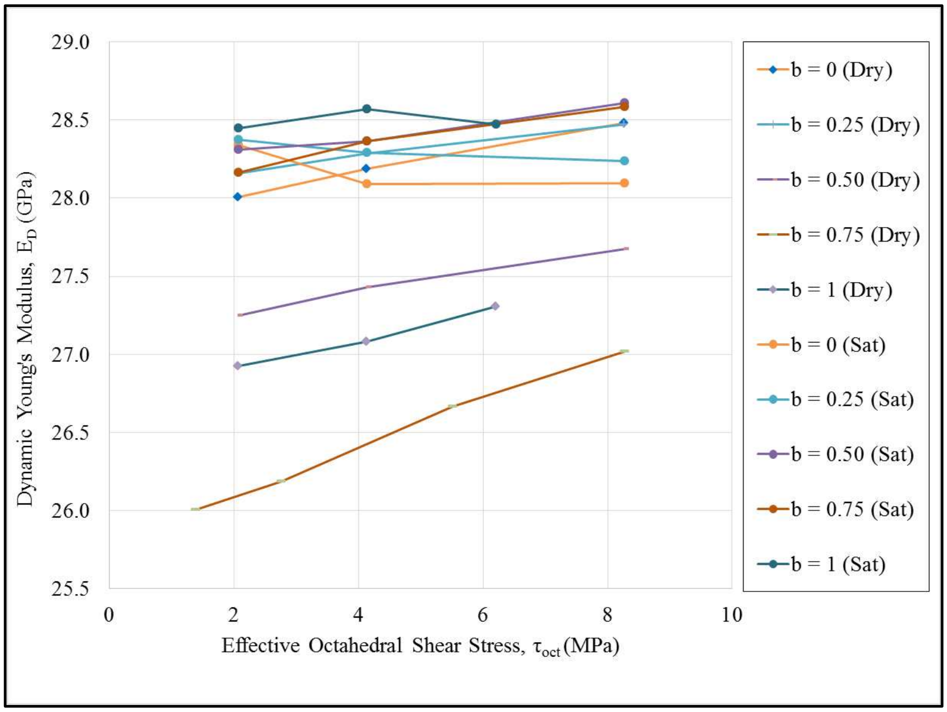

Figure 4.41: Dynamic Young's Moduli at $\sigma_{oct} = 20.7$ MPa.

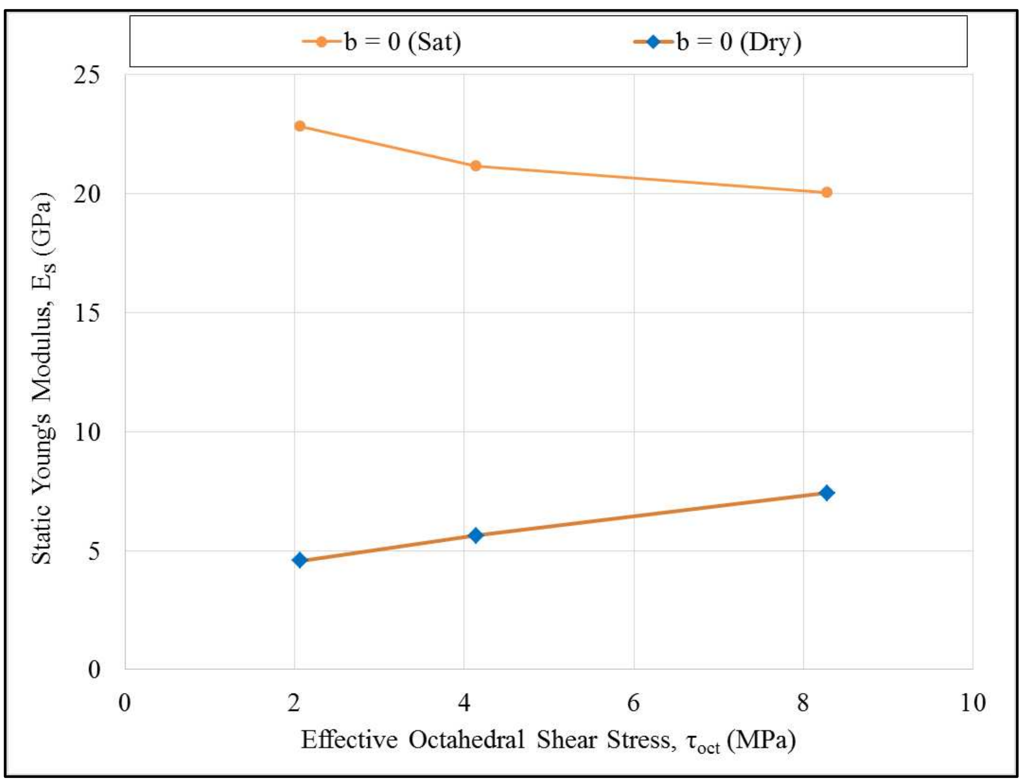

Figure 4.42: Static Young's Moduli at $\sigma_{oct} = 20.7$ MPa.

The dynamic Young's moduli display different relationships with b in the dry and saturated cases. The saturated E_D indicates a mostly directly proportional response to b for all normal stresses, meaning that the sample becomes stiffer at higher relative magnitudes of σ_2.There is more scatter in the dry E_D, and the relationship with the stress parameter, though not entirely consistent, is mostly reversely proportional. Both cases have a certain degree of inconsistency due to overlapping of data at different values of b, however, the general trends are more or less visible. The magnitudes of moduli in the two scenarios are quite similar. There is an increase in Young's moduli with higher normal stresses, as well as with increasing shear stress.

Static Young's moduli have much smaller magnitudes in the triaxial conditions, but rise with increasing normal stress. However, the dynamic data is consistently higher in magnitude. The saturated static moduli appear to be larger in magnitude for all stresses. Also, both cases display directly proportional response to b. However, only b values of 0 and 0.25 are incorporated into the calculation. Due to strain reversal occurring at $b \geq 0.5$, the calculated static Young's moduli become negative at those values of b. The reason for such behavior is based on assumptions in the calculation of Young's modulus. The assumption does not incorporate the effects of σ_2 on axial strain and therefore, the calculation does not account for negative strain in the axial direction. Due to these limitations of the elastic modulus, only the values at positive strains were used. In order to compare static and dynamic moduli, plots of E_D versus E_S are provided in Figures 4.42 – 4.45. From the relationships between Young's moduli, it is observed that saturated moduli approach the line $x = y$ at higher normal stresses, indicating a smaller difference between dynamic and static measurements, whereas the difference in the dry scenario remains almost constant. Larger b corresponds to a smaller difference between static and dynamic moduli. Because the static moduli approach dynamic ones at high stress magnitudes, it could signify a higher degree of accuracy for those dynamic moduli. However, even normal stress of 20.7 MPa, the dynamic moduli are larger, which is understandable, since the two methods incorporate very different strain amplitudes and frequencies.

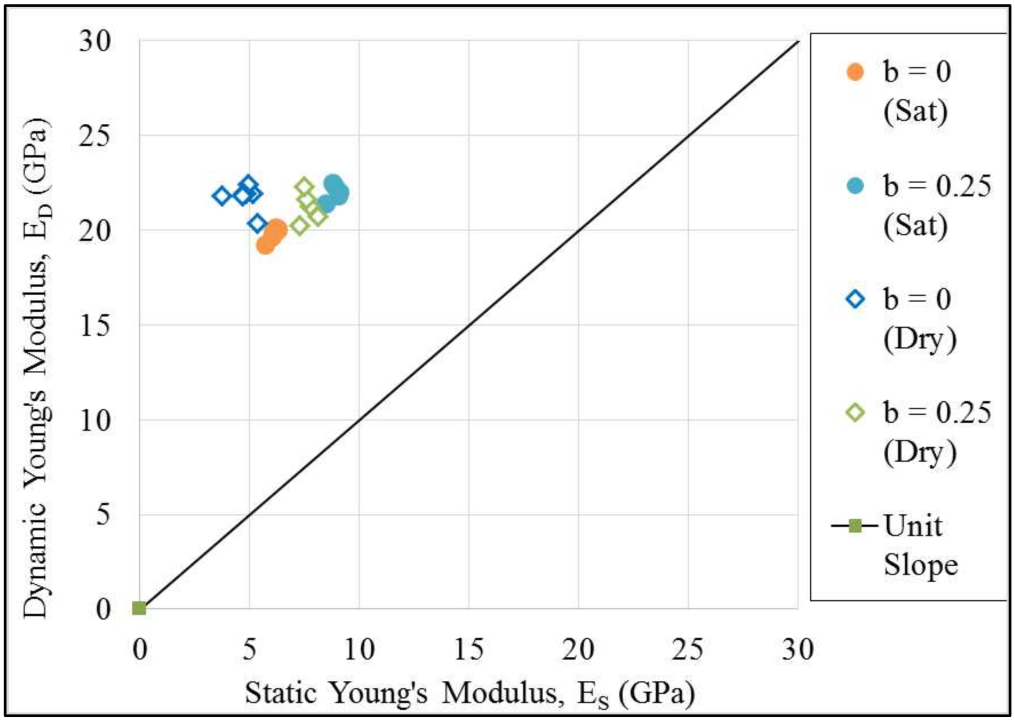

Figure 4.43: Relationship between dynamic and static Young's moduli for $\sigma_{oct} = 3.4$ MPa.

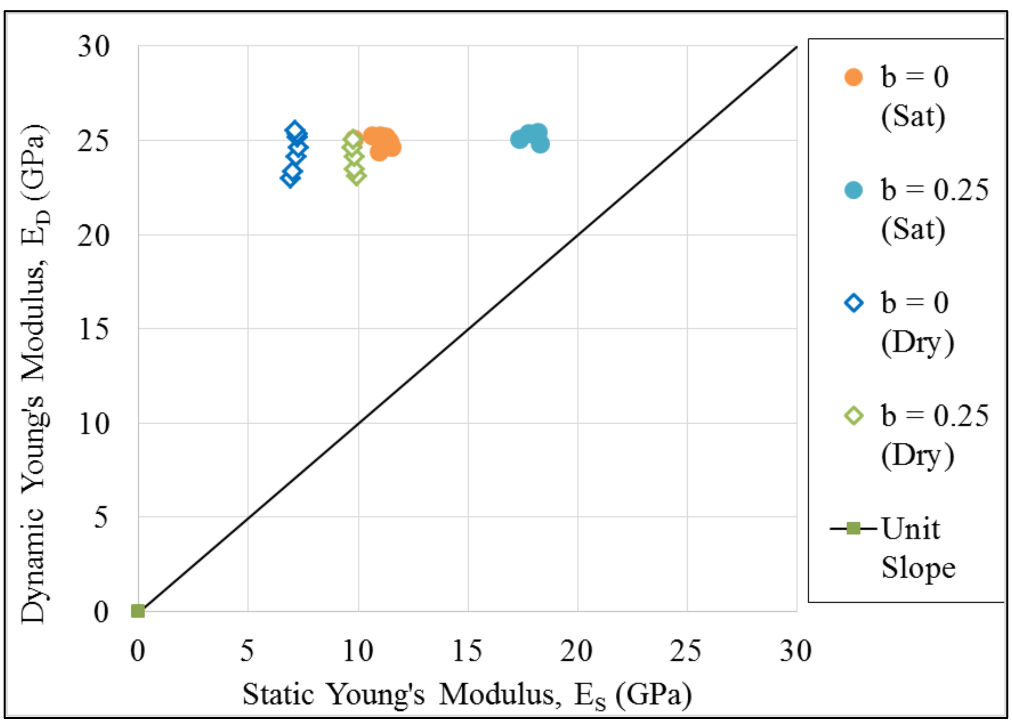

Figure 4.44: Relationship between dynamic and static Young's moduli for $\sigma_{oct} = 6.9$ MPa.

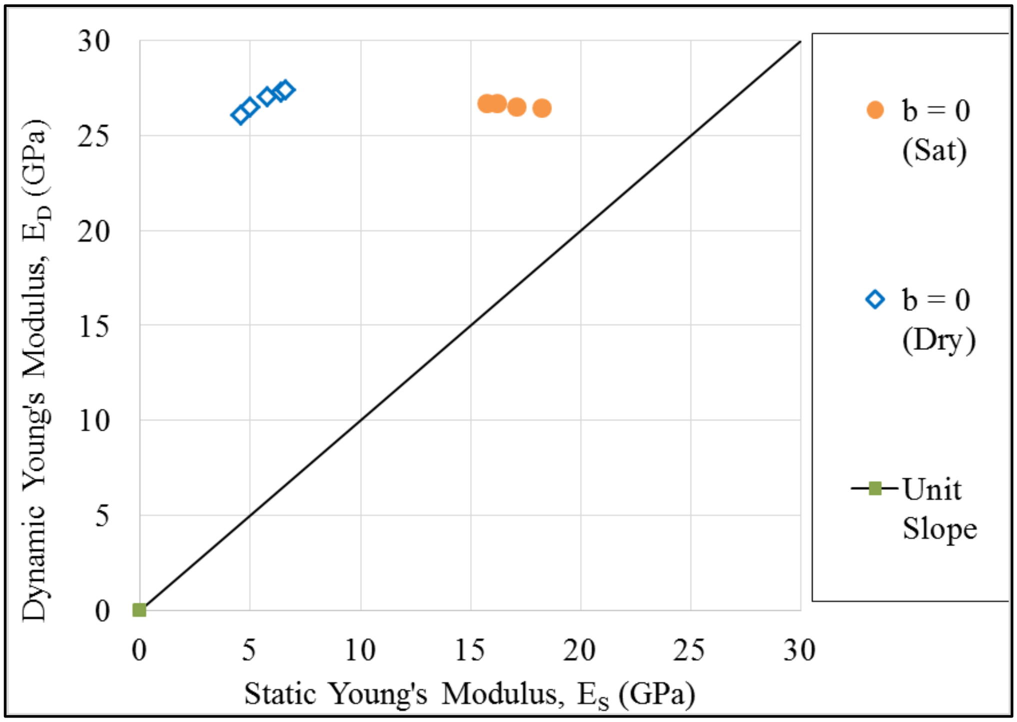

Figure 4.45: Relationship between dynamic and static Young's moduli for σ_{oct} = 13.8 MPa.

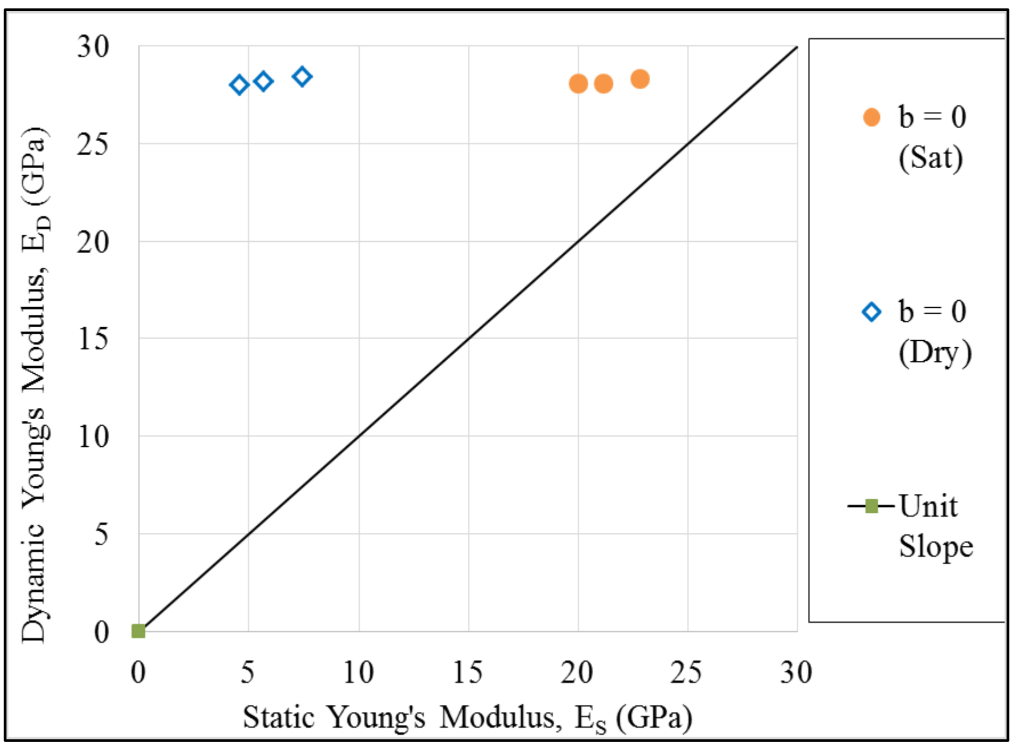

Figure 4.46: Relationship between dynamic and static Young's moduli for σ_{oct} = 20.7 MPa.

The ultrasonic wave propagation creates the smallest strain amplitudes, whereas static loading involves higher frictional sliding along grain boundaries (Fjaer 2009) and therefore has the highest strain amplitudes. However, the elastic moduli do not decrease at higher stresses in the tests, they increase. It is expected that at stresses that largely exceed 20.7 MPa both static and dynamic moduli will be reduced. For instance, Fjaer reported decreasing Young's moduli at axial stresses exceeding 60 MPa. The radial strain derived from dynamic Poisson's ratios and axial strain is illustrated in Figures 4.45-4.46 for saturated and dry cases. The radial strain is shown for σ_2 direction only, owing to the polarization of shear waves. The calculated radial strain reversal occurs at $b \geq 0.5$, at the same time with axial strain reversal, which is what would be anticipated in real measurement of radial strain. As the relative magnitude of σ_2 approaches that of σ_1, axial strain recovery begins, signifying that in σ_2 direction the samples are compacted. The magnitude of radial expansion is much smaller, compared to axial strain, for both dry and saturated conditions.

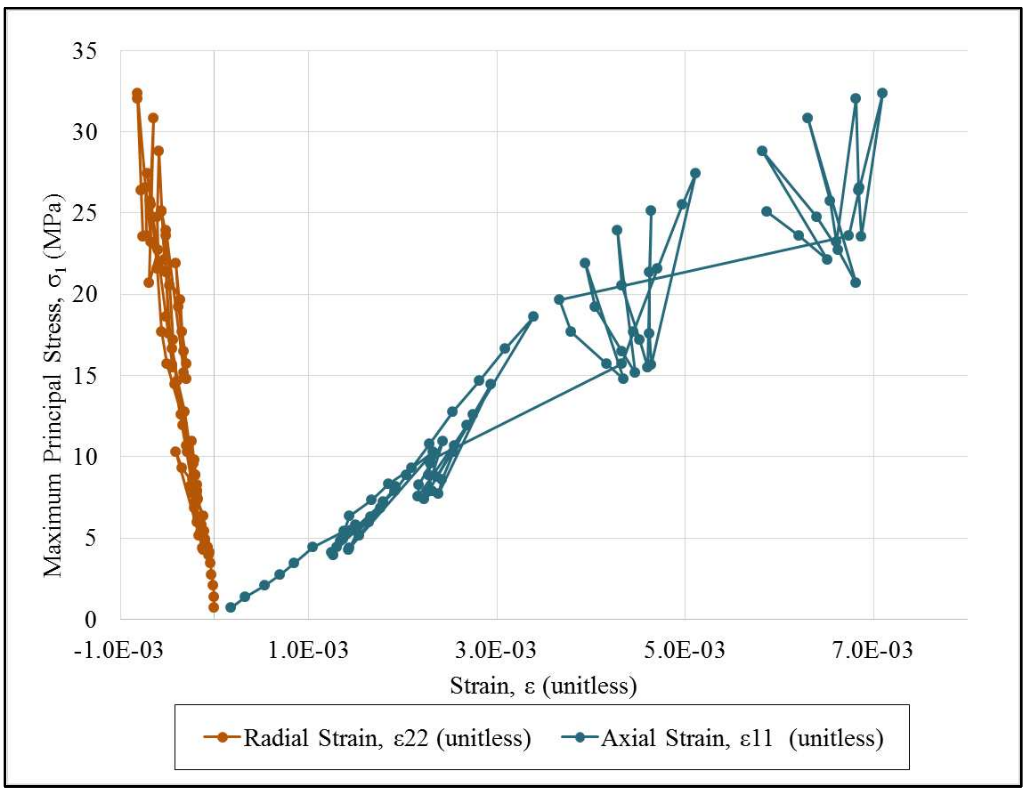

Figure 4.47: Dry sample axial strain and corresponding radial strain (σ_2 direction), calculated using dynamic Poisson's ratios.

The radial expansion in the saturated case is almost double that of the dry case, resulting from the differences in Poisson's ratios. This variance can be traced back to the differences in saturated and dry compressional wave velocities. As previously discussed, P-wave velocities of the saturated sample were larger in magnitude due to presence of another medium for propagation in the form of water filling the pore space. Even though saturated Poisson's ratios are higher than dry ones, dry Poisson's ratios display a more ductile behavior due to a dependence on shear stress. Therefore, the illustrated differences between two radial strain curves may not be fully representative of the real strains that took place during testing.

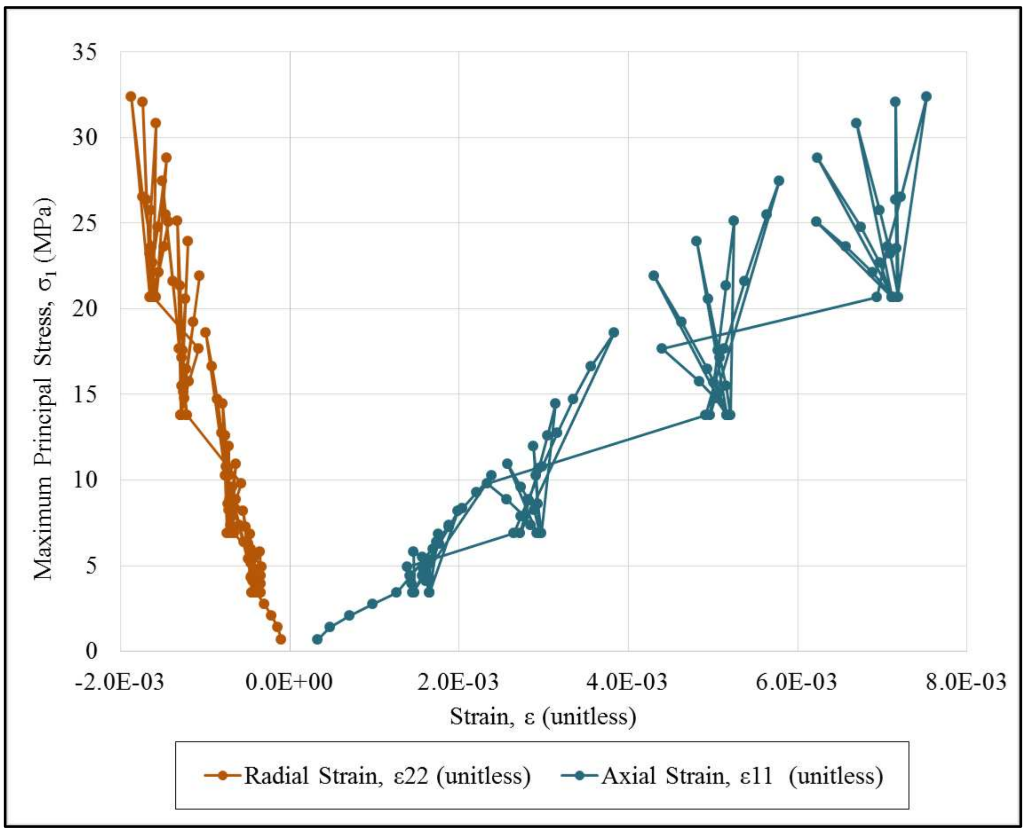

Figure 4.48: Saturated sample axial strain and corresponding radial strain (σ_2 direction), calculated using dynamic Poisson's ratios.

CHAPTER 5

CONCLUSION AND RECOMMENDATIONS

In this experimental study, the intended true triaxial testing of Buff Berea sandstone samples under dry and water-saturated conditions was successfully completed, along with measurements of axial strain, wave velocity propagation in the axial direction, and axial permeability variation for a variety of anisotropic and hydrostatic stress conditions were conducted. The objectives of this project have been achieved, with conclusions on stress-induced anisotropy of deformation, wave velocity, and permeability described below.

5.1 Conclusions

1. Upon careful analysis of response in P- and S-wave velocities, Vp/Vs velocity ratios, saturation effects, axial strains, and permeability to stress state and magnitude, it is concluded that the major source of stress-induced anisotropy is the interplay of opening and closing of microfractures oriented orthogonally to directions of increasing stresses. With the introduction of changing nondimensional stress parameter b, the additional control over microfractures in the radial plane has allowed a careful examination of microfracture effect on permeability in the axial direction, wave velocity propagation under dry and water-saturated conditions, and axial strain.
2. Permeability in the axial direction is influenced by both effective octahedral normal and shear stresses, as well as the relative magnitude of intermediate principal stress, portrayed by b. Permeability diminishes with increase in b at low stress (3.4 MPa), indicating that loading perpendicular to the flow direction decreases permeability, while flow-parallel loading increases it, as observed by a nearly uniaxial stress state. The effect of b is more negligible at higher normal stresses, however, with increased shear stress permeability can be further influenced by the stress parameter.

3. At stress conditions where b is equal to or larger than 0.5, axial strain reversal occurs, signified by increased lateral compaction in the σ_2 direction.
4. The UNGI true triaxial testing apparatus can be used to perform compressional testing under true triaxial stress state ($\sigma_1 \geq \sigma_2 \geq \sigma_3$), providing unrestricted radial sample deformation, and does not display any loading eccentricity, blank corner or end friction effects. Using the device, large magnitudes of stresses, exceeding 137 MPa, can be applied, granted it is allowed by the pump pressure capacities (the pressure rating of the apparatus was provided by the maker). Through comparison of test results from the apparatus to the results reported in the literature performed with similar rock specimens, correlation between the two sets of data was established. Compressional and shear wave velocity magnitudes and trends measured with the apparatus are in accordance with the velocities and trends determined under conventional triaxial and polyaxial loading in the literature. Axial strains and wave velocities under $b = 0$ exhibit deformational behavior that is consistent with that of triaxial compression state. Lastly, implementing the pore pressure system capabilities of the apparatus, permeability testing was conducted with results that parallel previous findings on stress-induced permeability anisotropy. The above results indicate that the UNGI true triaxial testing apparatus displays adequate testing capabilities and that the data it produces is comparable to that of conventional triaxial testing. It is possible to obtain results incorporating more realistic stress state conditions in order to improve input data for drilling, completion and hydraulic fracturing designs, reservoir simulations for reserve analysis, production optimization, and sand production prediction, among many other potential oil and gas applications.

5.2 Future Work Recommendations

Because of the extensive capabilities of the true triaxial testing apparatus, there exists a wide variety of improvements that can be made in both equipment and experimental research methodology. Firstly, with more calibration testing using original design, simultaneous measurements of wave propagation in three orthogonal directions can be established, which would allow wave velocity measurements in tensor form to study elasticity anisotropy of rock specimens. Deformation and failure measurements under true triaxial stress state at elevated temperature will provide further accuracy of creating true in-situ stress conditions.

Experiments with poorly consolidated and/or high-porosity formations to determine accurate drawdown conditions at the true in-situ stress state have a high potential for mitigation and/or prevention of sand production.

Experiments using preserved shale core samples should be introduced, given that geomechanical research on shales still incorporates many challenges but has a higher applicability in petroleum engineering projects. With true triaxial testing of shales, a variety of directions in research could be followed including fracture propagation studies in brine-saturated samples, proppant studies, and fluid-rock interactions under in-situ stress state. Another significant implementation of the apparatus can be failure testing under highly anisotropic stress conditions to model the envelope of maximum stress using true triaxial failure criteria. Last but not least is the inclusion of strain gages for radial measurements of static deformation. It should be noted that strain gage potential was previously explored at the beginning of this study and can be fruitful with more calibration work.

Regarding possible improvements to the research topic at hand, higher magnitudes of stress can be generated in future experiments to fully capture the effects of stress magnitudes and true in-situ stress state on stress-induced anisotropy of permeability, wave velocity, and static deformation well beyond the elastic limit of the rock.

REFERENCES CITED

Al-Tahini, A. M., and Abousleiman, Y. N. 2010. Pore-Pressure-Coefficient Anisotropy Measurements for Intrinsic and Induced Anisotropy in Sandstone. SPE Res Eval & Eng. V. 13 (02). SPE-116129-PA. http://dx.doi.org/10.2118/116129-PA.

Anderson, B., Bryant, I., Luling, M. et al. 1994. Oilfield Anisotropy: Its Origins and Electrical Characteristics. Oilfield Review, 6 (4).

Amadei, B. 1983. Introduction. In Rock Anisotropy and the Theory of Stress Measurements, V. 2, Chap. 1, 1-2. Springer Berlin Heidelberg.

Bruno, M. S. 1993. Micromechanics of stress-induced permeability anisotropy and damage in sedimentary rock. Mechanics of Materials. 18(1): 31-48. http://10.1016/0167-6636(94)90004-3

Castagna, J. P., Batzle, M. L., and Eastwood, R. L. 1985. Relationships between compressional-wave and shear wave velocities in clastic silicate rocks. Geophysics 50 (4): 571-581.

Dewhurst, D. N., and Siggins, A. F. 2006. Impact of fabric, microcracks and stress field on shale anisotropy. Geophysical Journal International 165: 135-148. http://10.1111/j.1365-246X.2006.02834.x

Eitzenberger, A. 2012. Wave Propagation in Rock and the Influence of Discontinuities. Doctoral Thesis. Lulea University of Technology, Lulea, Sweden.

Fjaer, E. 2009. Static and dynamic moduli of a weak sandstone. Geophysics 72 (2): 103-112.

Handin, J., Heard, H. C., and Magouirk, J. N. 1967. Effects of the intermediate principal stress on the failure of limestone, dolomite and glass at different temperatures and strain rates. Journal of Geophysical Research 72: 611-640.

Ita, S. L., Cook, N. G. W., Myer, L. R. et al. 1993. Effects of Stress Anisotropy on the Static and Dynamic Properties of Berea Sandstone. Int. J. Rock. Mech. Min. Sci. & Geomech 30(7): 785-788.

Jaeger, J. C., Cook, N. G. W., and Zimmerman, R., W. 2007. Fundamentals of Rock Mechanics, fourth edition, Oxford: Blackwell Publishing Ltd.

Karman, T.V. 1911. Festigkeitsversuche unter allseitigem druck. Z. Verein. Dtsch. Ing. 55: 1749–1757.

King, M. S., Chaudhry, N. A., and Shakeel, A. 1995. Experimental ultrasonic velocities and permeability for sandstone with aligned cracks. Int. J. Rock Mech. Min. Sci. & Geomech. 32: 155-163.

Kwasniewski, M. A., and Mogi, K. 2000. Faulting in an anisotropic, schistose rock under general triaxial compression. 4th North American Rock Mechanics Symposium, Seattle, WA, 31 July-3 August. ARMA-2000-0737.

Lene, G.W., and Owen, D.E. 1969. Grain Orientation in a Berea Sandstone Channel at South Amherst, Ohio. Journal of Sedimentary Petrology V. 39 (2):737-743. http://dx.doi.org/10.1306/74D71D02-2B21-11D7-8648000102C1865D.

Li, X., Shi, L., and Bai, B. 2011. True-triaxial testing techniques for rocks - State of the art and future perspectives. True Triaxial Testing of Rocks. Kwasniewski. M., Li. X. and Takahashi. M., Chap. 1, 3-18, Wuhan, China: Chinese Academy of Sciences. http://10.1201/b12705-3

Lo, T.W., Coyner, K.B., and Toksoz, M. N. 1986. Experimental determination of elastic anisotropy of Berea Sandstone, Chicopee Shale, and Chelmsford Granite. Geophysics 51 (1):164-171. http://dx.doi.org/10.1190/1.1442029.

Lockner, D. A. and Beeler, N. M. 2003. Stress-induced anisotropic poroelasticity response in sandstone. 16th ASCE Engineering Mechanics Conference, Seattle, WA.

Mavko, G. M. and Nur, A. 1979. Wave attenuation in partially saturated rocks. Geophysics 44 (2): 161-178.

Mogi, K. 1970. Effect of the triaxial stress system on rock failure. Rock Mechanics in Japan 1: 53-55.

Piane, C. D., Dewhurst, D. N., Siggins, A. F. et al. 2010. Stress-induced anisotropy in brine saturated shale. Geophysical Journal International 184: 897-906. http://dx.doi.org/10.1111/j.1365-246X.2010.04885.x

Pickett, G. R. 1963. Acoustic Character Logs and Their Applications in Formation Evaluation. Journal of Petroleum Technology 15 (6): 659-667. http://dx.doi.org/10.2118/452-PA

Popp, T., and Salzer, K. 2006. Anisotropy of seismic and mechanical properties of Opalinus clay during triaxial deformation in a multi-anvil apparatus. Physics and Chemistry of the Earth, Parts A/B/C 32 (8-14): 879-888. http://dx.doi.org/10.1016/j.pce.2006.04.022

Ramana, Y. V., and Venkatanarayana, B. Laboratory Studies on Kolar Rocks. Int. J. Rock Mech. Min. Sci. & Geomech 10: 465-489.

Rudnicki, J. B. 1977. Effect of Stress-Induced anisotropy on a Model of Brittle Rock Failure as Localization of Deformation. 18th U.S. Symposium on Rocj Mechanics (USRMS), Golden, CO, June 22-24. ARMA-77-0193.

Sayers, C. M. and Kachanov, M. 1995. Microcrack–induced elastic wave anisotropy of brittle rocks. Journal of Geophysical Research 100: 4149-4156.

Smart, B. G. D. 1995. A true triaxial cell for testing cylindrical rock speciments. Int. J. Rock Mech. Min. Sci. & Geomech. 32 (3): 269-275.

Smart, B. G. D., Somerville, J. M., and Crawford, B. R. 1999. A rock test cell with true triaxial capability. Geotechnical and Geological Engineering 17: 157-176.

Takahashi, M. and Koide, H. 1989. Effect of the intermediate principal stress on strength and deformation behavior of sedimentary rocks at the depth shallower than 2000 m. ISRM International Symposium, Pau, France, 30 August-2 September 1989. ISRM-IS-1989-003.

Thosuwan, R., Walsri, C., Poonprakon, P. et al. 2009. Effects of Intermediate Principal Stress on Compressive and Tensile Strengths of Sandstones. ISRM International Symposium on Rock Mechanics - SINOROCK 2009, Hong Kong, China, 19-22 May 2009. ISRM-SINOROCK-2009-055.

Tutuncu, A. N., Podio, A. L., Gregory, A. R. et al. 1998. Nonlinear viscoelastic behavior of sedimentary rocks, Part 1: Effect of frequency and strain amplitude. Geophysics 63 (1): 184-194.

Tutuncu, A. N., Podio, A. L., and Sharma, M. M. 1998. Nonlinear viscoelastic behavior of sedimentary rocks, Part 2: Hysteresis effects and influence of type of fluid on elastic moduli. Geophysics 63 (1): 195-203.

Wu, B. and Hudson, J. A. 1991. Stress-induced anisotropy in rock and its influence on wellbore stability. The 32nd U.S. Symposium on Rock Mechanics (USRMS), Norman, OK, 10-12 July. ARMA-91-941.

Yin, H. 1992. Acoustic Velocity and Attenuation of Rocks: Isotropy, Intrinsic Anisotropy, and Stress-Induced Anisotropy. PhD Dissertation, Stanford University, Stanford, California (December 1992).

Yin, H. and Nur, A. 1992. Stress-Induced Ultrasonic Velocity and Attenuation Anisotropy of Rocks. 1992 SEG Annual Meeting, New Orleans, LA, October 22-29. SEG-1992-1073.

Zoback, M. 2007. Basic Constitutive Laws. In Reservoir Geomechanics, Chap. 3, 60. Cambridge, United Kingdom: Cambridge University Press.

APPENDIX

CT SCANS OF DRY, SATURATED, AND INTACT BUFF BEREA SAMPLES

Three Buff Berea samples were used in collecting the CT scans: one intact sample that was not used in any testing, as well as the samples used in testing under both dry and saturated conditions. As can be seen by the scans of all three samples, there is no visible pore volume change after testing under both conditions, which signifies that loading was performed under the elastic limit of the rock. The strains of tested samples were fully recovered. While higher resolution scans could illustrate a higher degree of accuracy, overall trends are expected to be the same. The scans are shown in Figures Appendix.1-6.

Figure Appendix.1: Longitudinal scan of intact Buff Berea sample.

The scale of measurement is shown in Figure Appendix.7.

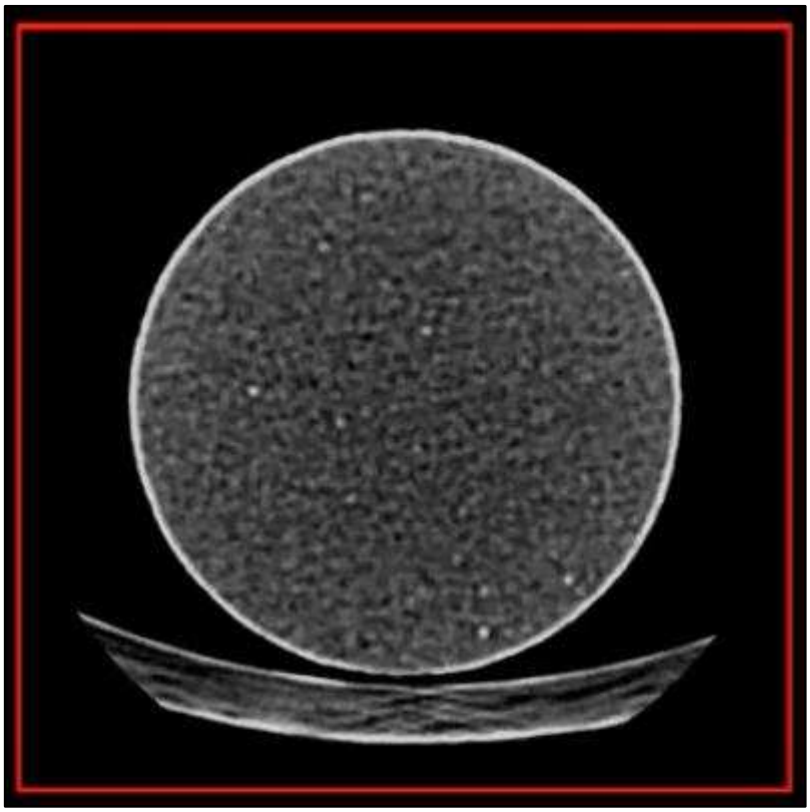

Figure Appendix.2: Transverse scan of intact Buff Berea sample.

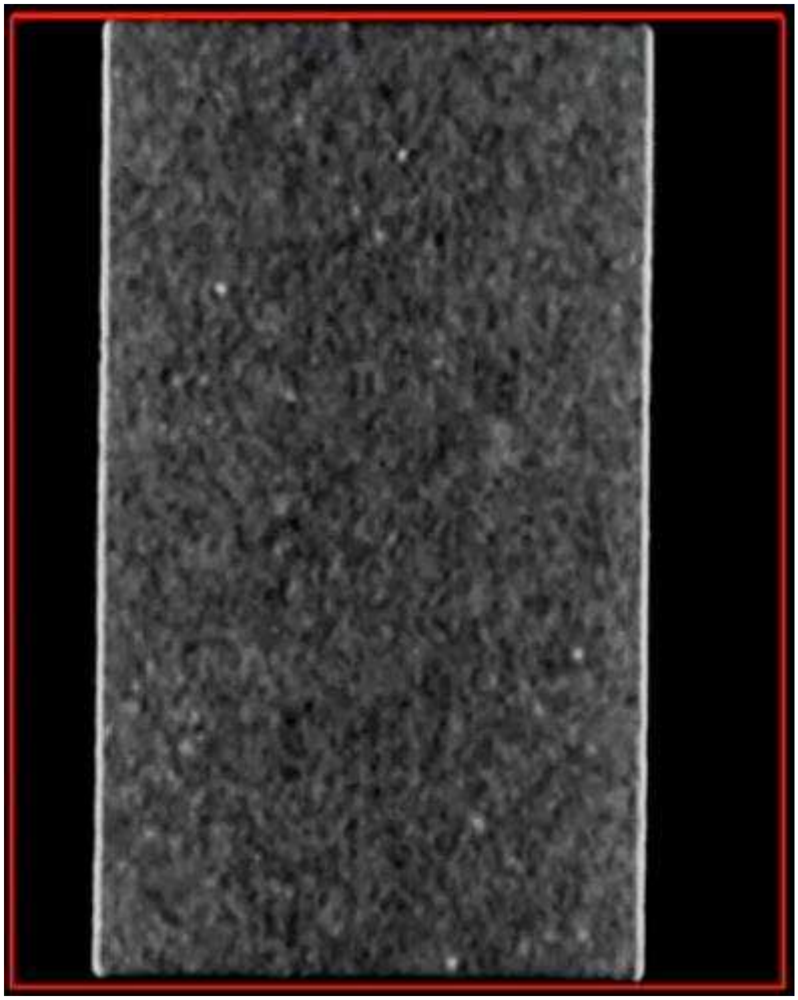

Figure Appendix.3: Longitudinal scan of Buff Berea sample used in dry condition testing.

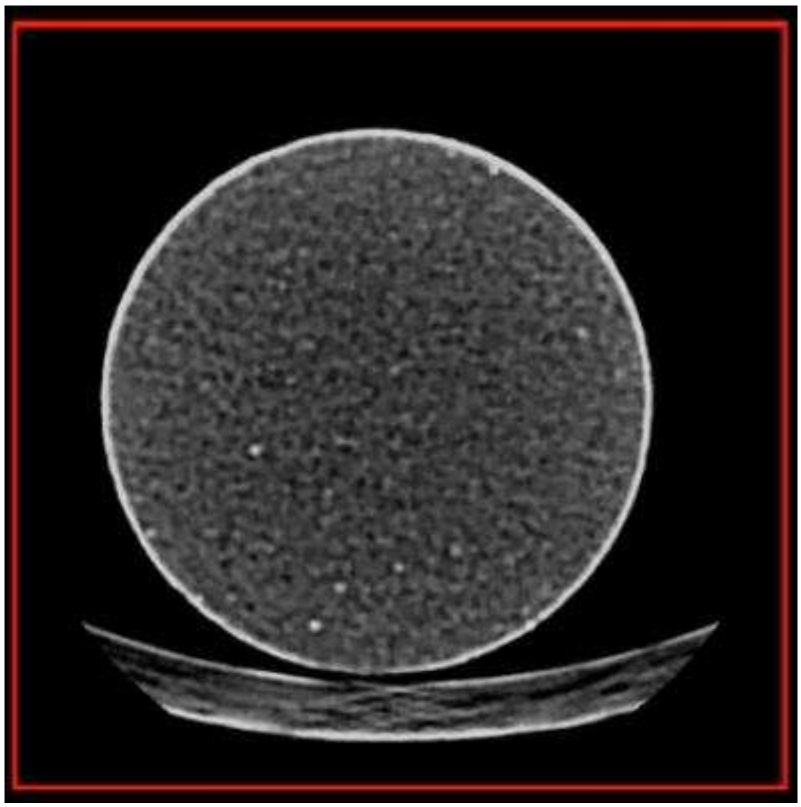

Figure Appendix.4: Transverse scan of Buff Berea sample used in dry condition testing.

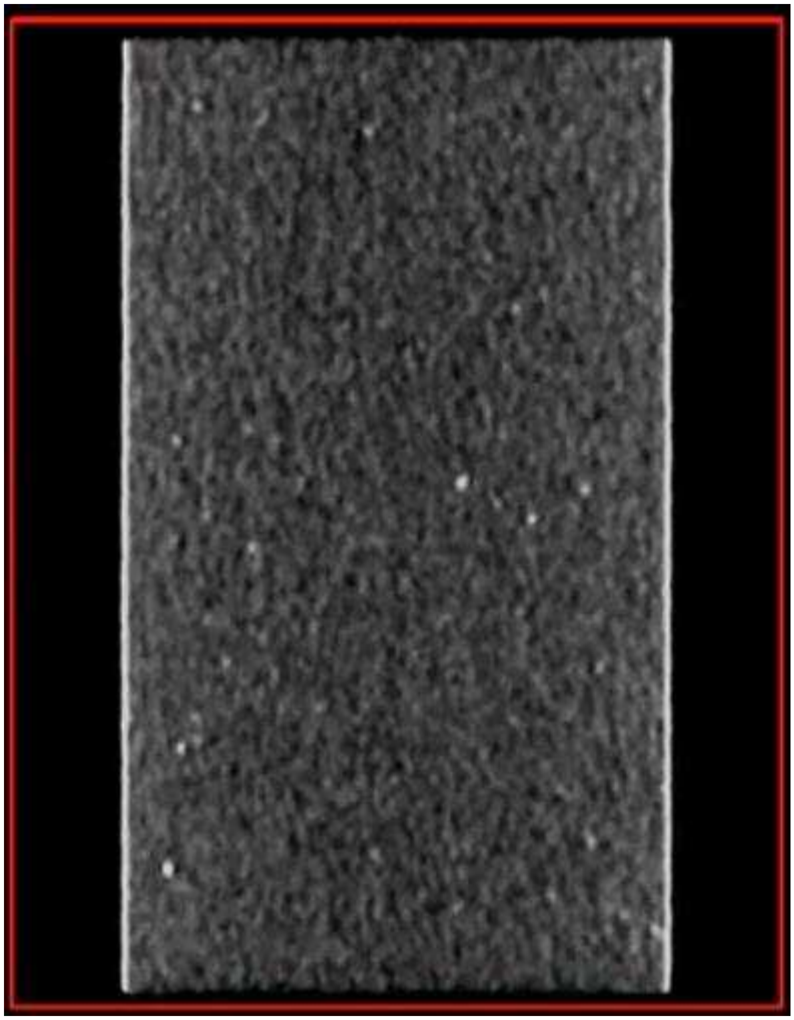

Figure Appendix.5: Longitudinal scan of Buff Berea sample used in water-saturated condition testing.

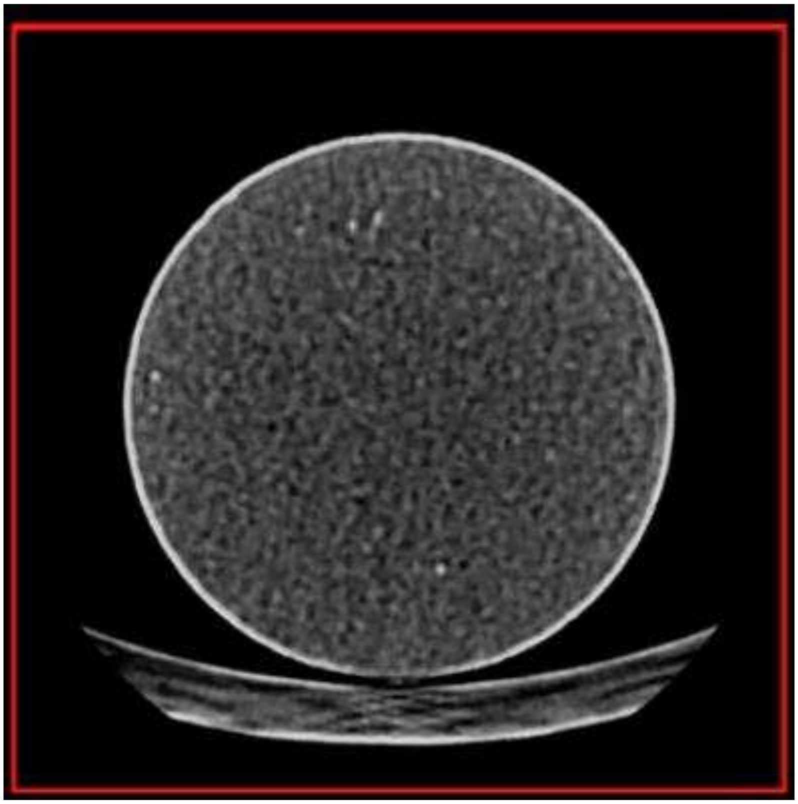

Figure Appendix.6: Transverse scan of Buff Berea sample used in water-saturated condition testing.

Figure Appendix.7: Hounsfield scale for all CT scans.